ELECTRON MICROSCOPE STUDIES OF ORGANIC PIGMENTS

by

GORDON RICHARD DUCKETT

being a thesis submitted for the degree of
Doctor of Philosophy in the Chemistry Department
of the University of Glasgow

MAY 1987

ACKNOWLEDGEMENT

I would like to take this opportunity to thank all those people who assisted in the production of this thesis.

To my supervisor Dr John Fryer, I owe an enormous debt of gratitude for his guidance, advice, helpful criticism and on occasions, stern encouragement during the course of the last three years. Dr T. Baird has also been a considerable source of helpful discussion and advice, as well as more than a few amusing anecdotes.

The project was an SERC sponsored CASE award in conjuction with CIBA-GEIGY Pigments Ltd, (UK). My thanks must be given to Dr Colin Campbell of Ciba-Geigy for his support and assistance.

Mr David Thom must be thanked for the maintenance of the equipment in the electron microscopy group along with my fellow workers Martin, Laura, Catherine, Ahmed, Raymond, Lorraine and Jeffrey, all of whom have contributed much in both discussion and friendship.

Mr Jim Beck of the Glasgow Computing Service and Dr W. O. Saxton of Cambridge University provided much needed assistance in the establishment of the image processing system at Glasgow, and Miss Diane McCormack should be praised for her efforts in typing part of this thesis.

Lastly, but by no means least, I would like to thank my family for their support. My grandmother, Mrs Anne Harvey, for her patience in proof reading the thesis, and my mother and her husband, Marion and Ken Wardrop and my brothers, Derek and Robert, for their encouragement.

Summary

Organic Pigments form a large and commercially important group of materials. Crystal structure analysis of these compounds has, in general, been hampered by the small crystallite size exhibited by these materials, which precludes the use of standard single crystal x-ray diffraction techniques. The results of using an electron microscope for the crystallographic analysis of an organic pigment provides one aspect of the work recorded in this thesis. Electron microscope studies of organic crystals suffer a major, resolution limiting factor in the susceptibility of the crystals to damage on exposure to the electron beam. Computer processing of electron microscope images of organic pigments has been applied to overcome the radiation damage problem. The installation of an image processing system and the results obtained from this are described. An organic pigment, Pigment Red 57, exhibits a colour shade change, brought about by a crystallographic change, on altering the crystal water content. One of the main aims of the project was to provide an interpretation for this shade variation.

INDEX

CHAPTER 1: ORGANIC PIGMENTS

1.1 INTRODUCTION

Colour has many applications in todays' society, from protection and identification to communication or simply decoration. Most of the colour used today is derived from organic pigments of one sort or another. Industrially, a pigment is defined as any finely divided solid material, a major function of which is to improve the appearance of the medium in which it is to be used. Incorporation is always by simple physical mixing of the pigment and medium. The colouristic properties of pigments depend, unlike dyes which colour as single molecules or small groups, not only upon the absorption properties of the molecules but also on their crystallographic arrangement.

The more conventional pigments, that is the azo's (red, orange and yellow colours) and the phthalocyanines (blues and greens), are used in applications where good resistance to light, heat and solvents is essential; for example in the colouring of printing inks, rubbers and household paints. The properties controlling the use of any particular pigment are light and solvent fastness, dispersibility,temperature stability and of course, as they are important commercial materials, cost and appeal.

The mechanical dispersion of the small pigment crystals, in the media in which they are applied, is hampered by their high interfacial energy which leads to crystal aggregation and in some cases, crystal growth. This directly opposes the strength and depth of colour produced in the medium and must be controlled by the pigment manufacturer. The properties exhibited by the pigments are affected, or more often purposely enhanced by their mode of preparation. Such factors as temperature, concentration and pH along with the addition of various resins and dispersing agents are critical and this is why much of the development of new products in the pigment industry today is centered on the improvement in physical properties when in use; for example ease of handling, dispersibility and flow.

The purpose of this chapter is to provide an introduction to some aspects of pigment chemistry and to review the limited amount of work which has been carried out on the solid state structures of the pigments which this project is concerned with.

1.2 PHTHALOCYANINE PIGMENTS

Phthalocyanines provide, almost exclusively, all the blue and green organic pigments in use today. The reason for this is that, in terms of cost, tinctorial strength, brightness of shade and all round fastness properties, they approximate most closely to ideal pigments.

A comprehensive reference work, dealing with most aspects of phthalocyanine chemistry and properties, has been written by Moser and Thomas (1983) and is mentioned here to save continual reference to it throughout this chapter.

Based on the structure shown in figure 1.1(a), the phthalocyanine molecule is rigidly coplanar and tetradentate. Usually the metal (M) used is copper but many other elements, such as Pt, Mn, Al and Si for example, can be coordinated in this position. The pigment as shown is blue in colour although substitution of the aromatic hydrogens by chlorine leads to a green material. Preparation of the pigment is achieved by the vigorous reaction of phthalic anhydride with urea and a copper salt in a high boiling point solvent such as nitro- or trichloro benzene, using ammonium molybdate as a catalyst. (see figure 1.1(b)).

The molecule occurs in several polymorphic forms, the most stable being the β-phase where the planar molecules stack in zig-zag columns such that the copper atom in one molecule is above a nitrogen atom in another, permitting a distorted octahedral coordination of the copper. The β-form, the thermodynamically more stable polymorph, is a green-shade blue compound whereas the other main variant, - the α-form -, is a red-shade blue. Other polymorphs (γ, δ and ε forms) show distorted α-structures, but as they have little commercial significance need not be mentioned further here. Figure 1.2 shows the essential differences between the β- and α- phases.

(a)

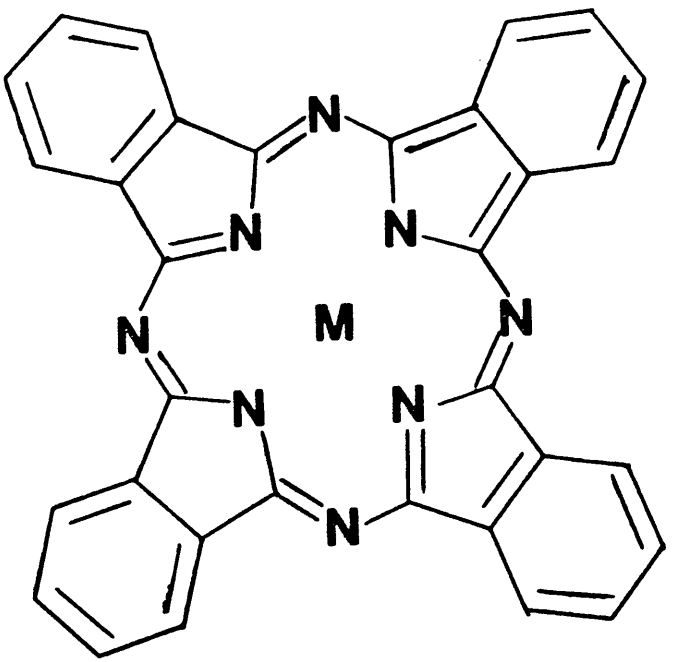

(b)

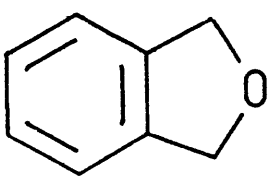

+ $(NH_2)_2CO$ + Cu^{2+} (salt)

ammonium molybdate → CuPc

Figure 1.1

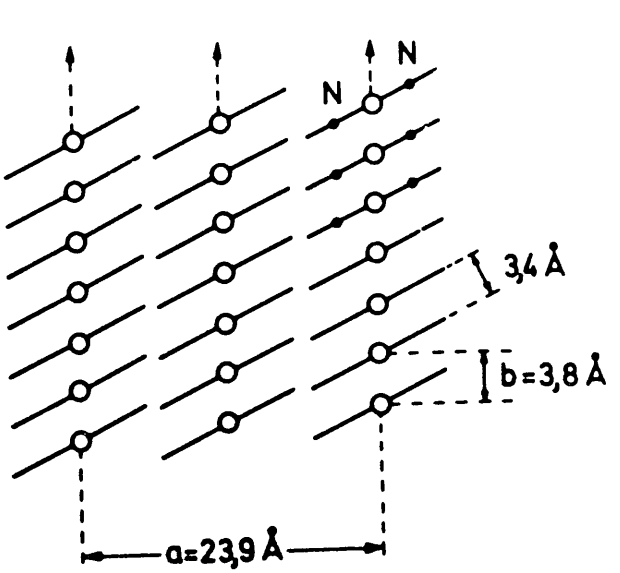

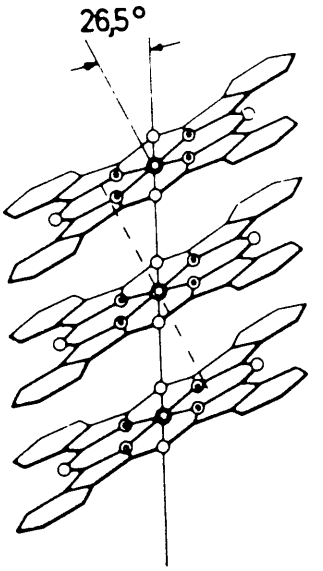

α-CuPc

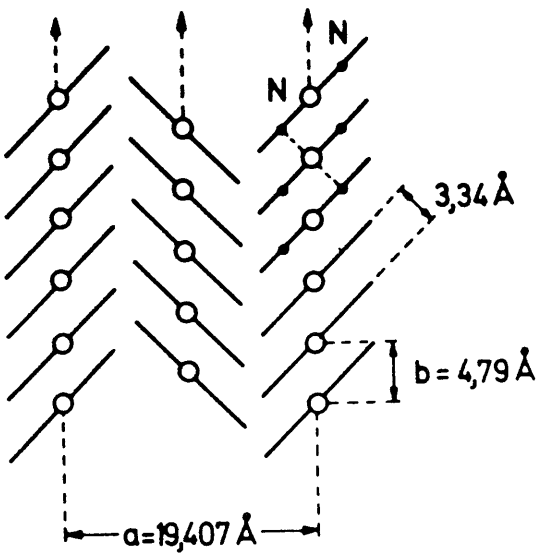

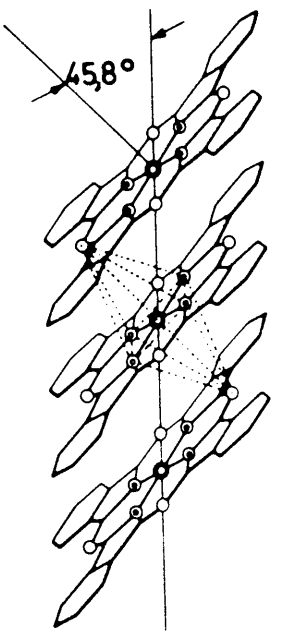

β-CuPc

Figure 1.2

As prepared, the β-form usually separates during formation and can also be obtained by grinding the crude pigment aggregates in the presence of a small amount of organic solvent such as an aromatic amine. The α-phase is precipitated in a process known as 'acid-pasting', where the pigment is ground in the presence of a mineral acid (usually concentrated sulphuric acid). The pigment dissolves in the acid to form a charge transfer complex which is destroyed on the addition of water (often referred to as 'drowning out').

Morphologically, the α-form crystals tend to be brick shaped whereas those of the β-form are rod shaped. This anisotropy of crystal growth of the β-form has been explained by the high density of contacts and the octahedral metal coordination between adjacent molecules, giving rise to the preferential growth along the b-axis of the crystal.

The solid state structures of the packing variations of the copper phthalocyanines have been extensively studied; notably, for example, by such workers as Robertson (1935) β-phase, Brown (1968) α-phase, Kirner et al (1976) and Mason et al (1979).

The development of epitaxial specimen preparation techniques (Ashida (1966 a,b) and minimal dose techniques (Williams and Fisher (1970)), along with improvements in instrument capability have allowed the examination of the fine structure of the crystals by

high resolution electron microscopy. The direct observation of molecular images of chlorinated copper phthalocyanines by , among others, Uyeda et al (1972), Murata et al (1976) and Fryer (1977),(1978), has been shown to be a powerful aid in the elucidation of the local molecular arrangement in the crystals and for defect analysis. (Fryer and Smith (1984)).

1.3 AZO- PIGMENTS

1.3.1 CLASSIFICATION AND USES

Azo pigments form, by far, the largest proportion of organic pigments produced. The discovery of aromatic diazo compounds in the mid 19th Century provided the impetus for the rapid growth of the dyestuffs industry in Europe, which reached its' height around the end of that century. In recent years, mainly due to the increased use of plastics and of colour in printing, the organic pigment industry has grown steadily.

Azo pigments are produced by the reaction of diazotised amines (diazo component) with a variety of coupling components. There are many different classes of azo colours, the more common being toluidine reds, arylamide reds, precipitated azo reds and diarylide yellows. The suitability of a class of pigment for a particular application is a primary consideration and the properties of all commercial pigments are stringently tested for as

wide a range of media and conditions as possible. Toluidine reds, for example, are cheaper to produce and often have a more acceptable shade than the precipitated azo reds, but have inferior solvent fastness properties which benefit the latter for use in rubbers.

Given the hundreds of possible combinations of diazo and coupling components, classification of the pigments presents considerable difficulties. Grouping pigments according to chemical composition, for example toluidine reds, or by the preparatory route used - precipitated azo reds- are frequently used methods of nomenclature. The issue is further confused however, by the fact that each manufacturer often has his own name for a particular pigment. The Colour Index, published jointly by the Society of Dyers and Colourists in Britain and the American Association of Textile Chemists and Colourists in the U.S.A., is a compilation of pigment names and shades, each pigment being denoted by a different number and shade number.

Colouring applications of azo pigments are widespread. Traditional uses such as inks and paints still account for a large percentage of the pigments produced. These generally require quite large quantities of pigment to achieve the desired shade - some printing inks can contain as much as 30 - 40% pigment by weight. The colouring of plastics (notably polyvinylchloride,PVC),on the other hand, requires proportionately much less pigmentary material. The increase in the use of plastics today

however, has provided a new and very large market for pigment manufacturers.

1.3.2 SYNTHESIS OF AZO PIGMENTS

As already mentioned, azo pigments are produced by the coupling of a diazotized amine with a variety of coupling components. This section deals with the preparation firstly by considering the general structures and synthesis of the two components and secondly by examining the coupling process.

(a) The diazo component

The product of the reaction of a primary aromatic amine with sodium nitrite, in a well cooled, acidic solution is an unstable compound known as a diazonium salt. (equation 1.3.2(i)).

$$ArNH_2 + NaNO_2 + 2HCL \longrightarrow ArN_2^+Cl^- + NaCl + 2H_2O \qquad ---1.3.2(i)$$

The mechanism of the reaction is not yet clear, however it would appear that the rate determining step involves the N-nitrosation of the amine (equation 1.3.2(ii)), (Bamberger (1894)).

$$ArNH_2 \xrightarrow[slow]{NO-X} ArNH-NO \xrightarrow[fast]{} Ar-N=N-OH \xrightarrow[fast]{acid} ArN=N \qquad ---1.3.2(ii)$$

Care must be exercised in avoiding an excess of the nitrite ion as the amine is in equilibrium with the corresponding ammonium ion ($ArNH_3^+$) and consequently an excess would exert an unfavourable influence on the reaction. A low temperature, usually of around 0-10°C, is required because of the moderate stability of the diazo product and to prevent the escape of nitrous gases. The resulting lower reaction rate is outwieghed by these considerations. In the case of amines with sparingly soluble salts, diazotization can be improved by the addition of surfactants.

The Lewis acid nature of the aryldiazonium ion suggests that the ion has weak electrophilic properties. Under the proper conditions, diazonium salts react with certain aromatic compounds to yield products of the general formula Ar-N=N-Ar', called azo compounds, in a process known as coupling. The presence of electron accepting substituents will increase reactivity. (Zollinger (1961)).

(b) The coupling component

The aromatic coupling component must, in general, contain a powerfully electron releasing group. Some of the more common coupling components are shown in figure 1.3

Preparation of the coupling component before coupling depends upon the nature of the substituents on the aromatic nucleus, for example the coupling rates of diazonium salts with phenols increase with increasing pH due to the greater

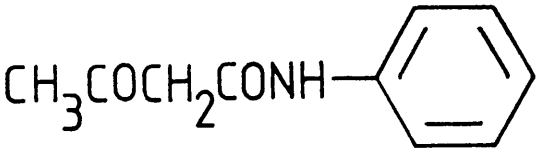

Acetoacetanilide

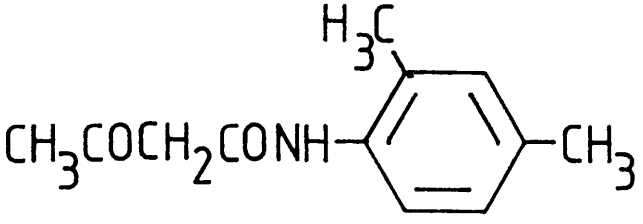

Acetoacet-m-xylidide

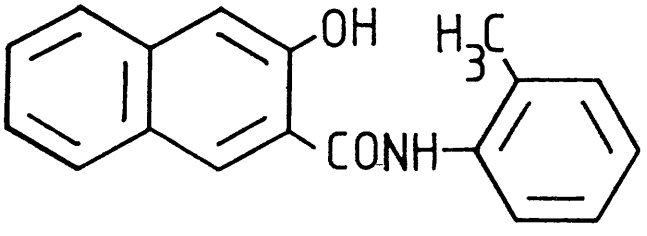

Naphthol AS-D
(o-toluidide of BONA)

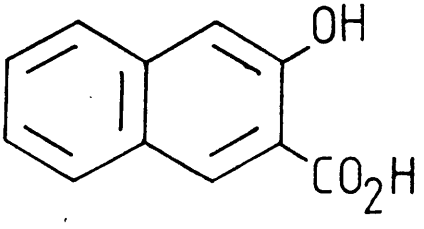

β-oxynaphthoic acid (BONA

Figure 1.3

concentration of phenoxide ions.

The coupling reaction mechanism is described as "Electrophilic Aromatic Substitution" and may be represented as shown in figure 1.4.

The azo pigment used in this work was CI pigment Red 57, CI Number 15850, known as a calcium 4B toner and is an example of a class of monoazo pigments called the precipitated azo reds. In the formation of this compound, as detailed in chapter 4, the organic pigment is precipitated or "laked" from solution by the addition of a metal salt, usually a calcium salt although other metals such as Mn, Mg, Ba, Sr, and Ni have been used. The diazo component is the diazonium salt of 6-amino-3-toluene-sulphonic acid, which is coupled with 3-hydroxy-2-naphthoic acid (β-oxynaphthoic acid or βONA). The molecular structure of this material is shown in figure 1.5.

1.3.3 SOLID STATE CHARACTERISTICS

The importance of particle size, shape and absorption properties and the crystallographic arrangement of the pigment molecules, to the suitability of a pigment for a given application, makes the study of the solid state extremely important. Crystal structure analysis has been hampered by the difficulty in growing pigment crystals to a size suitable for single crystal x-ray diffraction experiments. With the exception of the work carried out on the phthalocyanines mentioned in section 1.2 and a limited

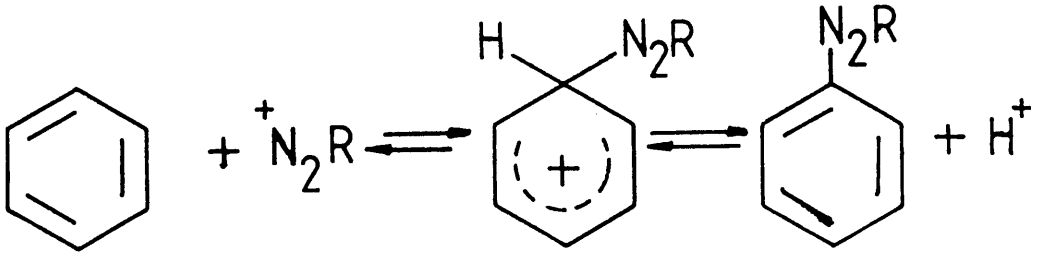

Figure 1.4

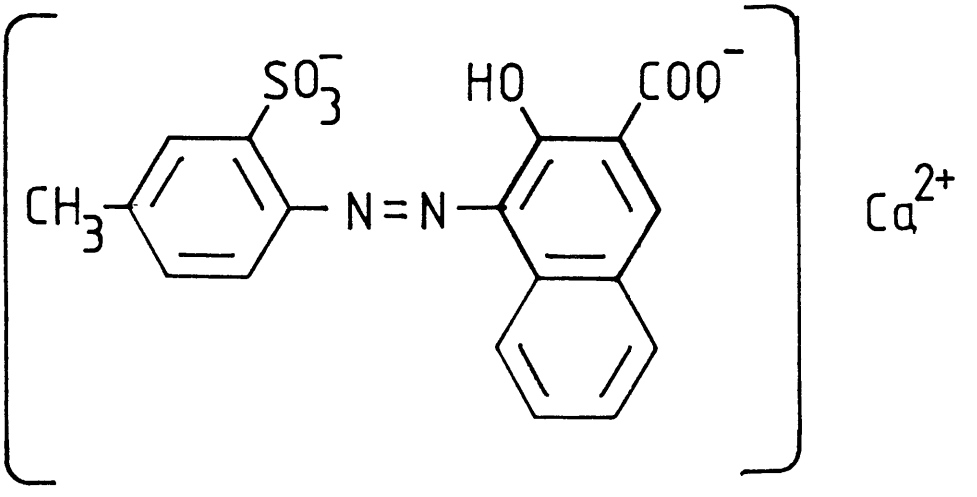

Figure 1.5

number of azo- compounds, the use of x-ray diffraction has largely been confined to powder techniques in an analytical capacity. Some azo- pigments involving β-naphthol have, however, proved to be amenable to study by single crystal x-ray diffraction techniques and several common features are described below. The molecular structures of the pigments concerned are shown in figure 1.6.

Firstly, it should be pointed out that the molecules of an azo- pigment involving β-naphthol may be represented by either of two tautomeric structures as shown in figure 1.7. The two structures differ with respect to certain bonds. In (I), the azo-bond (N=N) is a double bond with the adjacent (N-C) bond and the (C-O) bond being single. The opposite situation exists in the hydrazone tautomer (II) and this difference may be seen in the bond lengths in the structures. In all of the cases studied, it would appear that the molecules exist as the hydrazone tautomer. The bond lengths correllate well with the accepted values for (N-N),(C=N) and (C=O) bonds, quoted in the International Tables, and the bond angles subtended at the nitrogen atoms are approximately 120°. These bond angles imply that the molecules may exhibit cis-/trans-isomerism, but in each structure investigated, the trans- configuration was found (figure 1.8).

This molecular configuration also suggests a number of other features. The oxygen atom of the β-naphthol and the hydrogen atom of N(i) are situated too close to each other to be a non-bonded pair of atoms. The H --- O distance in

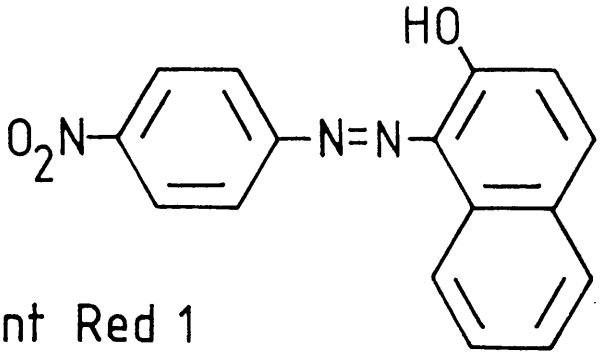

Pigment Red 1

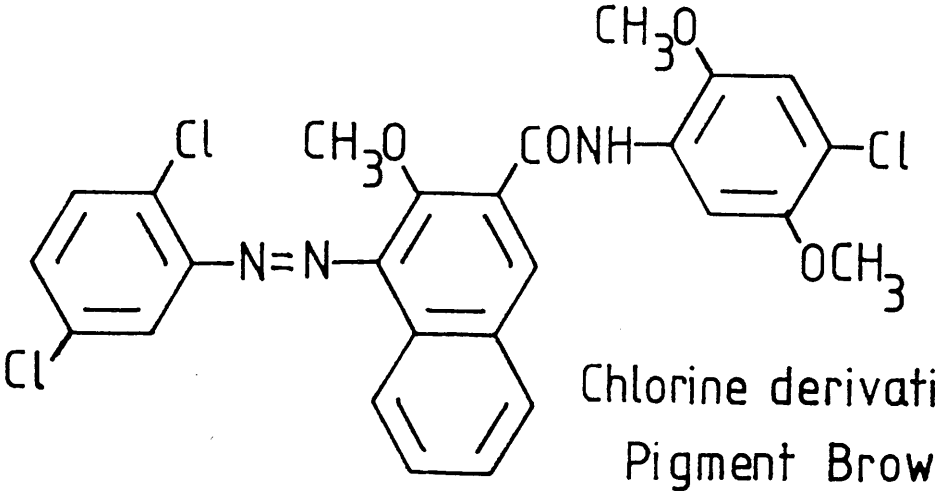

Chlorine derivative of
Pigment Brown 1

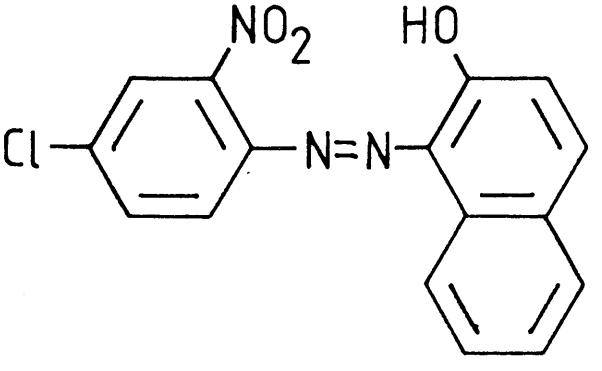

Pigment Red 6

Figure 1.6

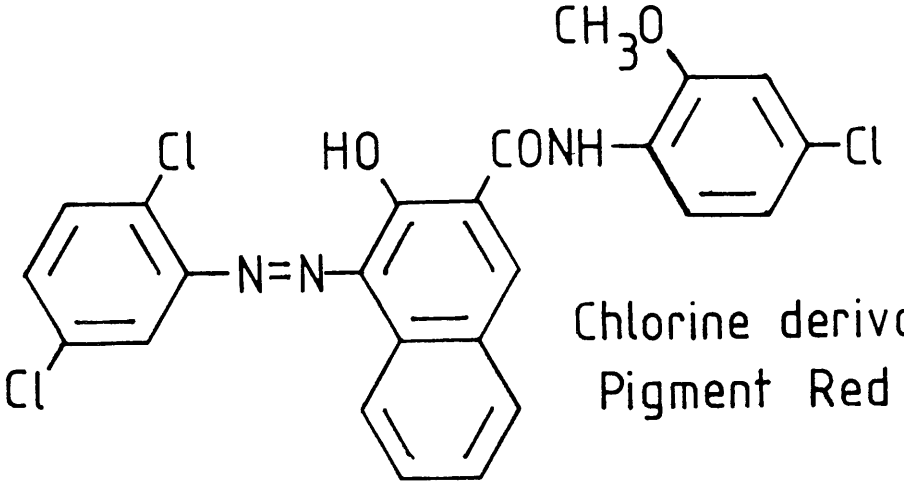

Chlorine derivative of Pigment Red 9

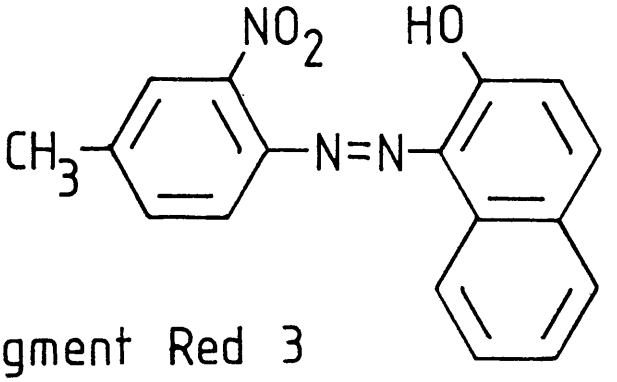

Pigment Red 3

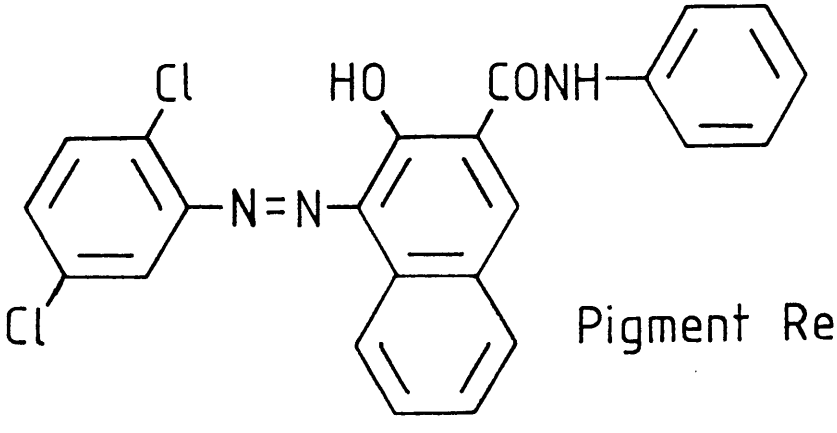

Pigment Red 2

Figure 1.6 (continued)

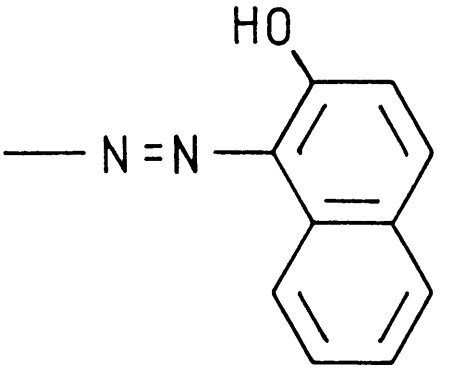

(I)

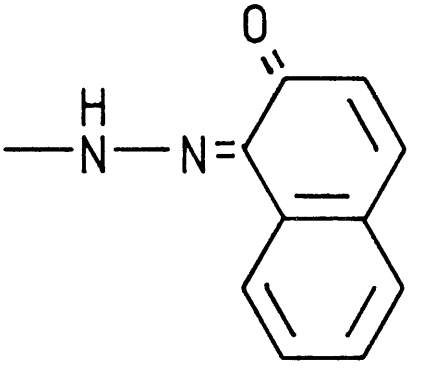

(II)

Figure 1.7

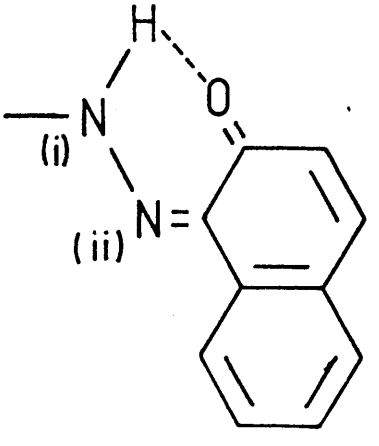

Figure 1.8

all cases, corresponds to that of a hydrogen bond, a fact previously suggested by the lack of hydroxylic properties exhibited by the molecules. The effects of this hydrogen bond are that, firstly, the azo- group will tend to be held in the same plane as the naphthalene moiety and secondly that the molecule will be "locked" in the trans- configuration. Light-induced cis-/trans- isomeric changes have been suggested as the reason for changes of hue on exposure to strong light (Allen (1971)).

Further hydrogen bonding is possible if the phenyl ring has an appropriate substituent in the ortho position. CI pigment Red 3, for example, has a nitro- group ortho to the hydrazo linkage and the measured (NO----H) distance of 2.62Å suggests that a bifurcated hydrogen bond, involving the hydrogen on N(I), the naphthalene oxygen and the nearer of the nitro- group oxygens, is present (see figure 1.9). Similar effects are shown by CI pigments Red 6 (o-nitro), Brown 1 (o-Cl), Red 9 (o-Cl) and Red 2 (o-Cl).

An immediate consequence of this bifurcated hydrogen bond is the constraint of both ring systems to the same plane. CI pigment Red 1 has a nitro substituent para to the hydrazo linkage and so the bifurcated hydrogen bond cannot occur. The deviation from planarity of this molecule is greater than for any of the others studied, the angle between the normals to the naphthalene and phenyl(azo) groups being 8.5°.

Whilst none of the molecules examined can be described as

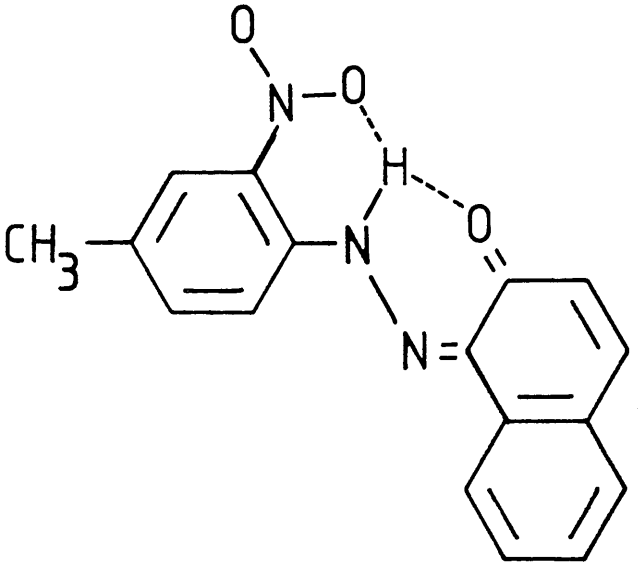

Figure 1.9

strictly planar, they can be considered essentially so. The bulk of the ring substituents is seen to have a ring distorting or "warping" effect; as in CI pigments Red 6 and Red 3 where the ortho-nitro group on the phenyl(azo) twists about the C-N bond and the naphthol oxygen twists out of the molecular plane, both movements being transmitted to the aromatic rings. This steric crowding effect is also seen in the chloro- substituted pigments Brown 1 and Red 9. Steric hindrance between adjacent molecules would also appear to have a distorting effect as shown by the fact that in CI pigment Red 3, where a methyl group replaces the para- substituted chlorine atom of CI pigment Red 6, the methyl group is coplanar with the phenyl(azo) ring.

In all cases, the molecules are stacked in columns in the crystal, with the column axis not perpendicular to the ring plane. The stacking may be parallel (CI pigments Red 1, Brown 1 and Red 9) or anti-parallel (CI pigments Red 6, Red 2 and Red 3) and adjacent columns may be packed in the same or different directions ("herring-bone" fashion). These stacking possibilities are shown diagramatically in figure 1.10. The molecules in the columns would appear to be linked only by Van der Waals forces, thus perhaps explaining why large single crystals can only be prepared with difficulty, if at all.

As with the phthalocyanines, it would appear that the azo pigments may also exhibit polymorphism. Whitaker (1980,1979) and Grainger and McConnell (1969) have described the structures of three polymorphs of CI pigment

(a) View down molecular columns

(i) parallel

(ii) anti-parallel

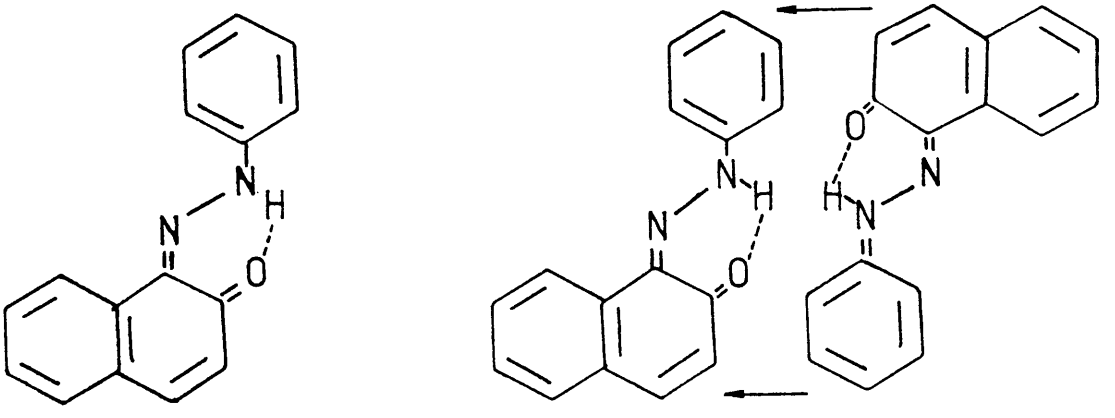

(b) Adjacent column packing

(i)

(ii) 'Herring-bone'

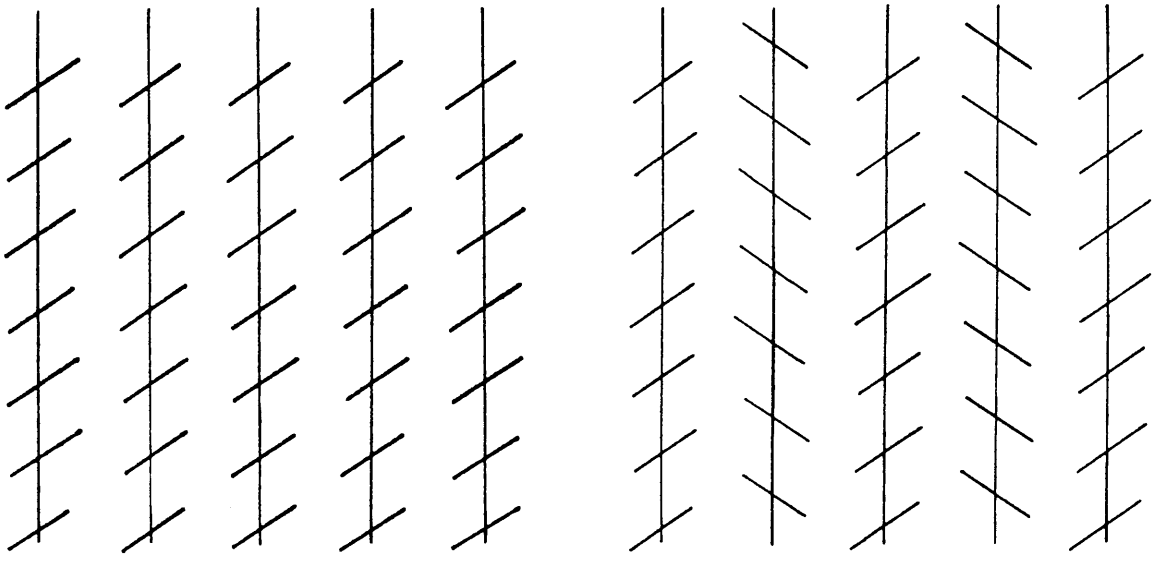

Figure 1.10

Red 1; the α,β, and γ forms. A fourth polymorph, the δ form has also been reported (Whitaker (1982)). The existance of polymorphic forms of a pigment can be important as the various forms may exhibit markedly different colour and other physical properties on application. It is not yet clear, in the case of azo-pigments, how slight changes in the production process, from manufacturer to manufacturer, affects the crystal form of the finished pigment. Indeed, different manufacturers may well produce pigments which, whilst chemically identical, show markedly different physical properties; an important consideration should a consumer choose to change his or her supplier.

The azo pigment used in this project was CI pigment Red 57, calcium 4B toner, and the next section deals with the reasons for studying this material and with the limited amount of information available on its' solid state structure.

1.3.4 PIGMENT RED 57, CALCIUM 4B TONER

This pigment provides a good example of how production parameters, such as pH and temperature, can affect the physical properties of the finished product, as the pigment exhibits a marked dependance of the red shading on the crystal water content. The molecular structure was already shown in figure 1.5.

At a high water content, the pigment has a distinctly

yellow shading, whereas at a lower level, the shade becomes bluer; the blue shade being the required commercial product. In production, the blue shading is developed by drying the filtered pigment (or "presscake") at relatively high temperatures (90-100°C), but care must be taken to ensure that this does not lead to thermal degradation, or other physical changes, in the pigment or pigment additives. Thermal gravimetric analysis (TGA) and differential scanning calorimetry (DSC) have shown that the yellow shading is associated with a crystal water content of 2 moles, whilst the bluer shading has only one mole of associated water and that this water is not merely water of crystallisation, but is in some way discretely bound to the pigment molecules (Young (1971)).

Early studies of the crystals by electron microscopy revealed little about the structural arrangement of the pigment molecules. The crystals were shown to be very small ($<$ 50nm) and to be extremely sensitive to electron beam damage, only their plate-like morphology being seen. The purpose of the present study then was to apply high resolution electron microscopy combined with computer image processing techniques to overcome the radiation damage problem, in order to determine the molecular arrangement in the crystals and hence account for the shade variation of the different hydration states.

CHAPTER 2: THE ELECTRON MICROSCOPE

2.1.1 GENERAL INTRODUCTION

The possibility of using an electron beam to obtain a higher optical resolving power than that obtained using visible light was suggested with the development of wave/particle theories (De Broglie (1924)) and wave mechanics (Schrödinger (1926)). Davisson and Germer's electron diffraction patterns (Davisson and Germer (1927)) served to validate De Broglies' hypothesis and along with parallel research into electron trajectories in magnetic and electric fields (Busch (1926),(1927)), led to rapid advances in the developing field of electron optics.

The result of this intense activity was the publication, by Knoll and Ruska (1932), of the development of an electron microscope, followed by a description of the construction of an instrument designed for high resolution imaging (0.5 um) in 1934 (Ruska (1934)).

Development and improvements on Ruska's basic design throughout the 1930's and 40's gave rise to microscopes capable of achieving a resolution of 10Å (Hillier and Ramberg (1947)) , while specimen preparation and manipulation techniques evolved in order to make fuller use of the power of the new instruments.

Modern electron microscopes, such as the JEOL 1200EX at Glasgow, are now achieving resolution of better than 3Å routinely and higher accelerating voltage instruments, such as the Cambridge 600kV microscope (Nixon et al (1977)), have achieved lattice resolution of less than 1Å

The Jeol 1200EX electron microscope has an accelerating voltage of 120kV and as such an electron beam wavelength of 0.003nm, given by the formula;

$$\lambda = \frac{1{\cdot}2261}{\sqrt{V}\cdot\sqrt{1+9{\cdot}7880\times10^{-7}}}\ \text{nm} \quad (2.1.1(i))$$

(corrected for relativistic effects).

This is considerably smaller than x-ray wavelengths of between 0.1 and 0.2nm and so electron microscopy, at first sight at any rate, should allow the direct imaging of atomic detail. As will be shown later however, the prospect of atomic imaging is hampered by the imaging process.

Nevertheless, electron microscopy has contributed greatly to our understanding of material structure in many diverse fields. Defect analysis by Hirsch, Howie et al (1965), molecular imaging studies of organic materials by Fryer and Smith (1984), Murata et al (1976) and the extensive literature on biological applications, in particular the 3 dimensional reconstructions of protein structures by Unwin and Henderson (1975) for example, give an insight into the extensive use of electron microscopes in modern science.

The purpose of this chapter is to outline the main features and operational modes of an electron microscope and to summarize the current theories of the process by which structural information about a specimen is transferred to electron microscope images.

2.1.2 THE TRANSMISSION ELECTRON MICROSCOPE (TEM): GENERAL CONSTRUCTION

This section deals with the main components of an electron microscope.

Figure 2.1 shows a schematic diagram of an electron microscope column, consisting of an illumination source (electron gun), two condenser lenses, a specimen stage, a number of image forming lenses and a recording device. In the case of the Jeol 1200EX electron microscope used in this work, the image forming lenses number five; namely, an objective lens, three intermediate lenses and a projector lens. The whole optical column is maintained at a vacuum of 10^{-6} torr or better.

The electron gun is the source of electrons in the instrument and most commonly is of the thermionic type. Field emission sources are also available but, as they were not used in this work, will not be described in any detail here. In the thermionic gun, the source of electrons is a heated cathode emitter and is normally a tungsten hairpin filament, although in this work a lanthanum hexaboride filament was used for increased brightness and coherence.

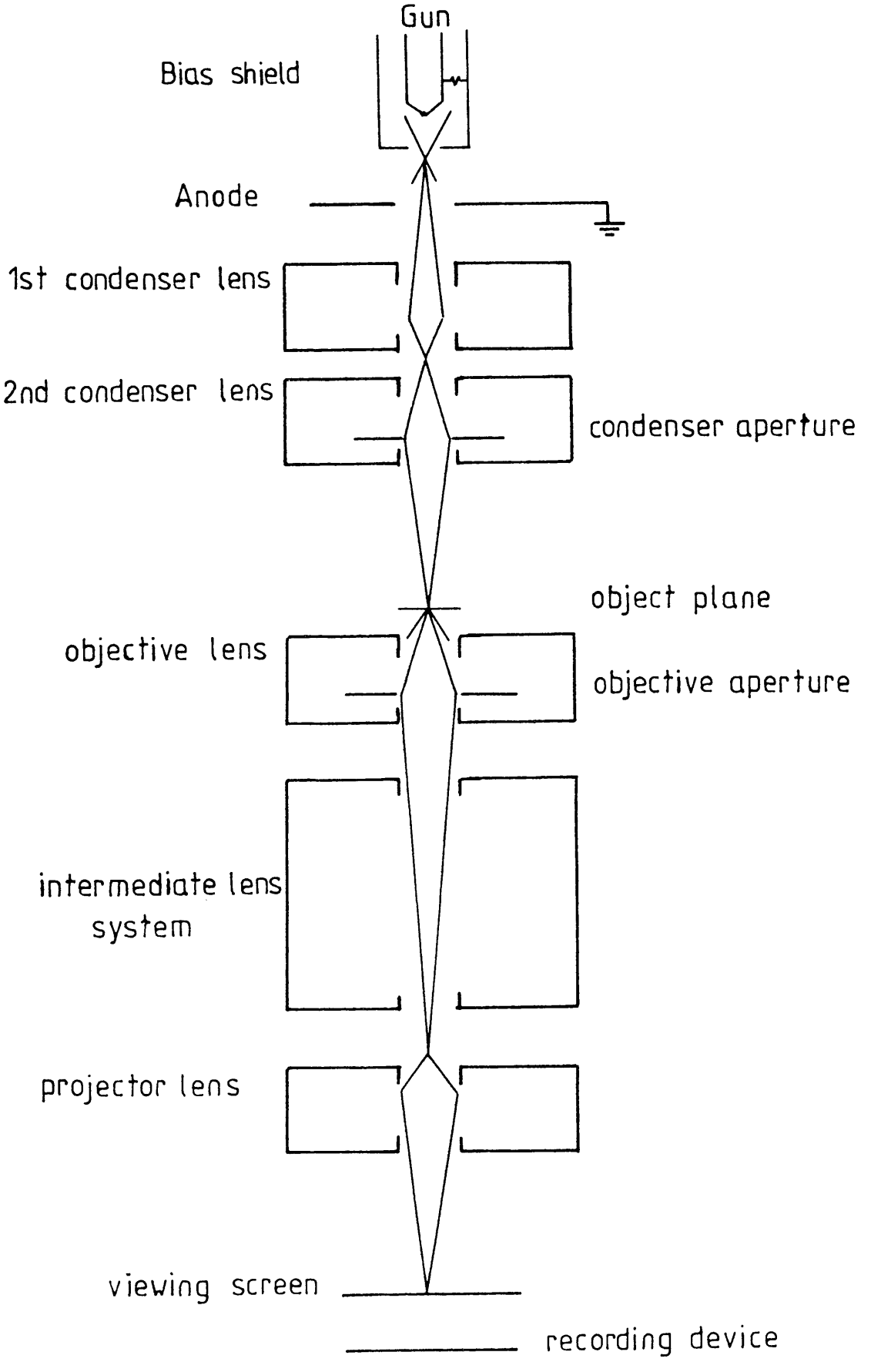
Gun
Bias shield
Anode
1st condenser lens
2nd condenser lens
condenser aperture
object plane
objective lens
objective aperture
intermediate lens system
projector lens
viewing screen
recording device

Figure 2.1

The electrical heating of this filament in an accelerating potential of, in this case, 120kV between the cathode and the anode leads to thermionic emission of electrons from the filament tip. The biassing shield acts as an electrostatic lens, decreasing the source size and hence increasing its' intensity, so that the result is a thin beam of electrons with a spread of wavelengths related to the filament temperature.

The condenser lens system consists of two electro-magnetic lenses and a fixed and a variable aperture and is used to control the intensity and angular convergence of the electron beam at the specimen. High resolution electron microscopy demands highly parallel, coherent incident illumination and the design of the electron gun and condenser lens system is tailored to suit this requirement A series of magnetic deflector coils is included in the illumination system to allow accurate alignment of the beam.

The objective lens is a short focal length lens which images the electrons scattered by the specimen. As the aberrations in this lens are not compensated for by the remaining image forming lenses, unlike the situation in light microscopes, its' performance is crucial to the overall performance of the microscope. Of these aberrations, the most important is the third order spherical aberration because the scattered electrons are close to the optical axis of the instrument, therefore diminishing the effects of the higher order aberrations

such as coma and distortion. Astigmatism in the lens, caused by deviations from cylindrical symmetry, is corrected by electromagnetic stigmators. The affects of the objective lens on the scattered electrons will be considered in the next section.

The objective aperture, situated in the back focal plane of the objective lens, serves to limit the amount of scattered electrons reaching the recording device, by stopping any beams scattered through an angle larger than that subtended by the aperture from contributing to the image.

The remaining lenses, the three intermediate lenses and the projector lens, magnify the image produced by the objective lens to a range of final magnifications (up to 10^6 X). By appropriate alterations to the intermediate lens current the microscope can be used in the 'Selected Area Diffraction' mode (see section 2.3).

Finally the recording device at the bottom of the column is usually a photographic plate. The image is recorded by means of a controlled exposure of a photographic emulsion to the electron beams comprising the image. In other cases, a television camera has been used to display the image on a television screen or to store it, in digital form, in a computer framestore. This latter approach has led to some interesting examples of real time dynamic processes being recorded on video tape and of course, with the image in a digital form, it is then accessible to the application of computer image processing techniques.

2.2 IMAGE FORMATION

2.2.1 INTRODUCTION

Correct interpretation of electron microscope images requires an understanding of how the structural information about the specimen is transferred through the optical system. The theory, as outlined below, is presented more fully by other authors. (Glaser (1952),(1956), Hawkes (1973), Glaeser (1982)).

Electron micrographs can essentially be considered to be complicated interference patterns. The nature of these patterns arises from the atom positions in the specimen and the way in which the electron optics of the microscope allows recombination of the scattered electrons to form the image. Firstly, the wave propagation from the exit face of the specimen to the final image will be described, followed by the effect of specimen structure on the incident electron beam.

2.2.2 TRANSFER THEORY

An electron microscope may be considered as a system which can be described in terms of Abbe's theory of imaging. (Goodman (1968), Hawkes (1972)). This "Fourier Optics" approach considers that the image is formed in two stages; a Fourier transform of the object plane wavefunction gives the diffraction plane (back-focal plane) wavefunction and

a second transform yields the image plane wavefunction. This wave optical approach takes into account the effects of lens aberrations, image defocus, the presence of an objective aperture and the coherence of the illumination.

The result of this approach is to consider the electron microscope as a linear imaging system as the input and output are related by the linear Fourier transform operator.

The Schrödinger equation for the motion of electrons through the microscope is the most suitable method for describing the situation (Glaser (1952), Saxton (1978)).

The wavefunction in any chosen plane z, can be expressed in terms of the wavefunction leaving the object plane z_o, within the limits of the paraxial approximation (all electron trajectories near and at small angles to the electron optical axis), by the following;

$$\psi(\underline{x},z) = \frac{1}{i\lambda h}\exp\left(\frac{i k h'}{2h}|\underline{x}|^2\right)\int \psi_o(\underline{x}_o)\exp\left(\frac{i k g}{2h}|\underline{x}|^2\right)\exp\left(\frac{-ik}{h}\underline{x}\cdot\underline{x}_o\right)d^2\underline{x}_o$$

where $k = \frac{p}{\hbar} = \frac{2\pi}{\lambda}$ and $g=g(z)$, $h=h(z)$ etc. 2.2.2(i)

This equation represents the propagation law for the electron wavefunction between different planes of the microscope. The cartesian coordinates (x,y) are denoted by a vector $\underline{x}$, g(z) and h(z) are solutions of the paraxial equations of motion such that;

$$g(z_o) = h'(z_o) = 1$$
$$g'(z_o) = h(z_o) = 0 \qquad 2.2.2(ii)$$

and $\psi(\underline{x}_o, z_o)$, ($=\psi(x_o, y_o, z_o)$) represents the wavefuction leaving the object plane.

The form of the wavefunction in the diffraction plane is then;

$$\psi(\underline{x}_d, z_d) = \frac{E_d}{i\lambda h} \exp\left(\frac{ikh'}{2h}|\underline{x}|^2\right) \int \psi_o(\underline{x}_o) \exp\left(\frac{-ik}{h}\underline{x}_d \cdot \underline{x}_o\right) d^2\underline{x}_o \qquad 2.2.2(iii)$$

as $g(z_d)=0$. and $E_d = \exp\left(\frac{i\pi h \underline{x}_d . \underline{x}_d}{\lambda h}\right)$

$\psi(\underline{x}_d, z_d)$ is then proportional to the Fourier transform of the wavefunction at the object plane and as such is the Fraunhofer diffraction pattern of the object wavefunction.

Considering equation 2.2.2(i), images of $\psi(\underline{x}_o, z_o)$ are formed in any plane z_i for which h vanishes. The image wavefunction is therefore obtained by a further application of equation 2.2.2(i). This analysis is suitable for a perfect optical system however, for real optical systems, the resulting wavefunction must be multiplied by a masking function A(x) to take account of the objective aperture, the spherical aberration and defocus of the lens and the coherence of the illumination. The exact form of this function will be dealt with in section 2.2.4, therefore it is sufficient to state here that it exists.

The neglect of aberrations other than spherical aberration

is known as the isoplanatic approximation, which states that the image of a point object has the same form wherever that point is in object space. For an isoplanatic system, the image plane wavefunction is then;

$$\psi(\underline{x},z_i) = \frac{-1}{\lambda^2 h^2 g_i}\exp\left(\frac{i k g_i'}{2 g_i}|\underline{x}|^2\right)\int A(\underline{x}_d)F\left(\psi_o\left(\frac{\underline{x}_d}{\lambda h_d}\right)\right)\exp\left(\frac{i k}{h_d g_i}\underline{x}\cdot\underline{x}_d\right)d^2\underline{x}_d \qquad 2.2.2(iv)$$

Thus $\psi_i(\underline{x}_i, z_i)$, the image plane wavefunction, is proportional to the inverse Fourier transform of $(F(\psi_o(\underline{x}))A(\lambda f\underline{x}))$.

By considering transforms;

$$F(\psi_i(\underline{p})) = 1/M\ F(K(\underline{p}))F(\psi_o(\underline{p})) \qquad 2.2.2(v)$$

and therefore the microscope, characterised by K- a function of the nature of the optical system, acts as a linear filter. The spatial frequency spectrum at any frequency $\underline{p}$ is the product of K and the object wavefunction component at the same frequency.

The function K is the impulse response of the microscope and its' transform is known as the coherent transfer function of the system. As shown, this can be evoked to relate the image and object transforms and its' use reflects this ease of application.

2.2.3 SPECIMEN - BEAM INTERACTION

The previous section described the propagation of the wavefunction leaving the object, through the microscope. The scattering of the electrons by the specimen has now to be considered. Only the salient features of the types of interactions which take place will be discussed here. More complete accounts are given by Cowley (1975), by Reimer and Gilde (1973) for isolated atoms and thin films, by Misell (1973) with reference to inelastic scattering and by Hirsch et al (1965) for crystals.

The scattering of incident electrons arises from their interaction with the electrostatic potential distribution in the specimen. The specimen may be described by a complex transparency which depends only on object position and as such is described as "multiplicative". Almost all the electrons pass through the specimen undeflected (as long as it is not too thick), with only those passing close to atoms being scattered. Thus we can split the emerging wavefunction into two terms; the primary or unscattered beam, represented by unity and the scattered wave represented by the rest. This concept of splitting the wavefunction in this manner will be seen shortly.

The nature of electron - specimen interaction is extremely varied and one of the important divisions of the types of interaction which can be made is that between elastic and inelastic scattering events. Inelastic processes will be considered in more detail in the section dealing with

radiation damage (section 2.2.6), but may be described here as scattering events resulting in a loss of energy of the scattered electrons. The net effect of inelastic scattering is to reduce the contrast in the image by imposing an out-of-focus background of intensity.

Elastically scattered electrons are the primary information carriers in an electron microscope. Image contrast is generally defined in terms of the variation of image intensity relative to the mean intensity. The main contribution is from the unscattered beam whilst the variation in contrast arises mainly from the electron scattering properties of the specimen. The scattering of electrons at angles larger than that subtended by the objective aperture results in "aperture" contrast or, in the case of periodic specimens, "diffraction" contrast. Thus areas where the scattered electrons are prevented from reaching the image appear dark in contrast. In general, this type of contrast is only important at low to medium resolution.

The elastically scattered electron waves have a phase lag caused by the specimen, resulting in a path length difference when compared with the undiffracted beam. The view of images as complicated interference patterns can then be explained by the recombination of the phase altered elastically scattered electrons and the central beam. The resulting variation in image contrast is known as "elastic phase contrast" and is of primary importance in high resolution imaging (see section 2.2.4). If the scattering

arises from a periodic structure in the specimen, for example a crystalline specimen with at least one lattice plane orientated parallel to the beam direction, then, with selected levels of defocus, a related periodicity in the image contrast may be obtained. This is the basis of "lattice imaging" in high resolution electron microscopy. The effects of lens aberrations on the retrieval and interpretation of information obtained by 'phase contrast' microscopy can then be understood, as small periodicities in the object will give rise to widely scattered electrons being focused by off-axis parts of the objective lens.

As stated at the beginning of this section, specimen - beam interaction is extremely complicated. The scattering cross sections of matter for electrons are five to six orders of magnitiude greater than for x-rays. Consequently, the probability of an electron scattering event is very high. It is reasonable to believe then that an electron, having already undergone a scattering interaction with one atom in the specimen, will undergo further scattering. Theories dealing with such multiple scattering events are termed 'dynamic' and were first advanced in the 'multi-slice' formulation of Cowley and Moodie (Cowley and Moodie (1957)) Such a rigorous approach will clearly represent the scattered amplitudes and phases more accurately, but at the expense of a simple interpretation of image contrast, as it is no longer possible to describe the transmitted wave as a product of the incident wave and the specimen transparency (see section 2.3).

Phase contrast effects can only be simply interpreted for thin specimens ($<$10nm), where a single scattering event or 'kinematical' approximation can be said to hold. In such an approach inelastic and dynamical processes are neglected and the object is regarded as a pure phase object; that is an object which retards the electron wave as it traverses the specimen. The scattered wave amplitudes are assumed to be much smaller than the undiffracted wave amplitudes and that the electron wavelength is vanishingly small. Under these conditions, assuming a normally incident plane wave of amplitude A, the transmission function for a pure phase object would be;

$$\psi_t(x,y) = \psi_o \exp(-i\sigma\phi(x,y)) \qquad 2.2.3(i)$$

where $\phi(x,y)$ is the projection of the Coulomb potential distribution in the beam direction and is the interaction constant (π V/ λ), V is the accelerating voltage.

The weak phase approximation is then invoked by assuming $\sigma\phi(x,y) \ll 1$ and so the transmission function ψ_t becomes;

$$\psi_t(x,y) = \psi_o (1 - i\sigma\phi(x,y)) \qquad 2.2.3(ii)$$

The Fourier transform (F) of this object wave then gives the diffraction plane amplitudes in the back focal plane of the objective lens;

$$\psi_d(u,v) = F(\psi_t(x,y)) \exp(i\chi(u,v)) A(u,v) \qquad 2.2.3(iii)$$

The terms $\chi(u,v)$ and $A(u,v)$ account for the effects of wave aberrations and the objective aperture.

In the kinematic approximation then, the resultant amplitude distribution is given by the difference between the primary wave amplitude $\delta(u,v)$ and the elastically scattered amplitude distribution. The form of equation 2.2.3(iii) is therefore;

$$\psi_d(u,v) = \delta(u,v) - (\sigma\phi(x,y)\sin\chi(u,v) - i\sigma\phi(x,y)\cos\chi(u,v) \qquad 2.2.3(iv)$$

In accordance with Abbe's theory of imaging then, the image plane wavefunction is arrived at by a second application of the Fourier transform operation;

$$\psi_i(x,y) = 1 - F(\sigma\phi(x,y)\sin\chi(u,v) - i\sigma\phi(x,y)\cos\chi(u,v)) \qquad 2.2.3(v)$$

The intensity distribution in the image plane $I(x,y)$ is then;

$$I(x,y) = \psi_i \psi_i^*$$

$$= 1 - 2\sigma\phi(x,y) * F(\sin\chi(u,v)) \qquad 2.2.3(vi)$$

where * denotes convolution

Phase contrast effects in high resolution electron

microscopy are generated as a result of the phase distortion function $\sin \chi$ due to any sort of wave aberration associated with the objective lens. Such phase contrast transfer functions are of primary importance in understanding the intensity distribution in the image plane and form the subject of the next section.

A further complication can be added by admitting a weak amplitude variation in the transmitted wave in addition to the weak phase variation. The result of applying a similar weak scattering approach to a weak, mixed phase and amplitude object, is that the image intensity I(s) is given by;

$$I(s) = \delta(s) - 2F(\eta(x)\sin\gamma(s)) - 2F(\mu(x)\cos\gamma(s)) \qquad 2.2.3(vii)$$

which is a linear combination of the phase and amplitude contrast effects. While it is no longer possible in this case (the weak phase and amplitude object approximation - WPAO), to represent the Fourier transform of the image intensity as the product of the Fourier transform of the object function and a phase and amplitude modulating function, the result is still simple as the phase contrast is characterised by one transfer function, whilst the amplitude contrast is characterised by another.

As yet, there is little evidence to indicate to what extent objects can be described as mixed, weak phase and amplitude objects, however some experimental evidence does suggest

that the inclusion of a weak amplitude variation is a valid representation for specimens for which the weak phase approximation fails (Erickson and Klug (1971)).

Before progressing however, importance of the contrast transfer functions should be described.

2.2.4 CONTRAST TRANSFER FUNCTIONS

Scherzer considered the theoretical resolution limit of the TEM and derived a wave-mechanical formulation of image formation, according to the Fourier optical theory of "linear systems", (Scherzer (1949)). The performance of a linear system is characterized by the "transfer function" of the system and relates, in the case of an electron microscope, periodic variations in image contrast to variations of the same periodicity in the transmittance function of the object.

Phase contrast in electron microscopy is governed by the function $\sin\chi$ in equation 2.2.3(vi). For a perfect lens, $\sin\chi = 1$ and the image intensity is given by;

$$I(r) = 1 - 2\sigma\phi(r) \qquad 2.2.4(i)$$

The presence of wave aberrations however can be accounted for by an instrumental modulation factor $\chi(s)$ where;

$$\chi(s) = 2\pi/\lambda \left(\Delta f \frac{\alpha(s)^2}{2} - Cs \frac{\alpha(s)^4}{4} \right) \qquad 2.2.4(ii)$$

$\alpha(s)$ is the scattering angle for the diffracted beam

Cs is the spherical aberration constant

Δf is the lens defocus.

As can be seen, the function $\sin\chi(s)$ is oscillatory and its' value will depend upon the scattering angle, the defocus and the objective lens spherical aberration. $\sin\chi(s)$ or the phase contrast transfer functions (PCTFs') for the Jeol 1200EX electron microscope have been plotted and some examples are shown in figure 2.2 assuming coherent illumination.

In use, the defocus value chosen, say for a periodic object, should be such that there are no sharp oscillations of contrast over the maximum range of spatial frequencies. This "optimum defocus" value or "Scherzer" focus Δf, is given by;

$$\Delta f = 1.2\sqrt{Cs\lambda} \qquad 2.2.4(iii)$$

In the case of the Jeol 1200EX, $\Delta f \doteqdot 100nm$.

Eisenhandler and Siegal (1966) calculated the Scherzer cut-off, d_{min}, as;

$$d_{min} = 0.65\ Cs^{1/4}\lambda^{3/4} \qquad 2.2.4(iv)$$

Different spatial periodicities can be imaged with reverse contrast or removed entirely from the image, depending upon the chosen level of defocus. It is common practice to

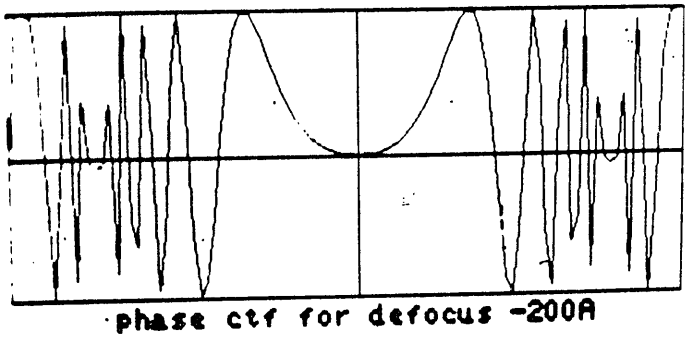
phase ctf for defocus -200A

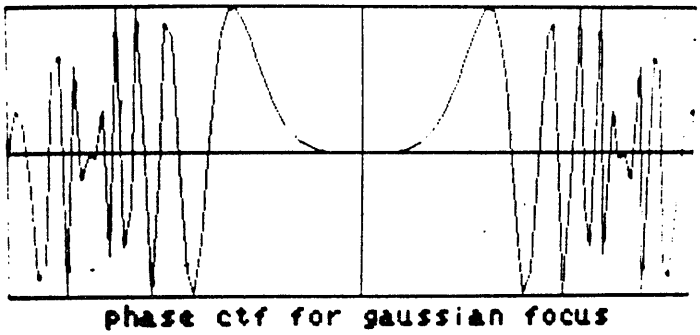
phase ctf for gaussian focus

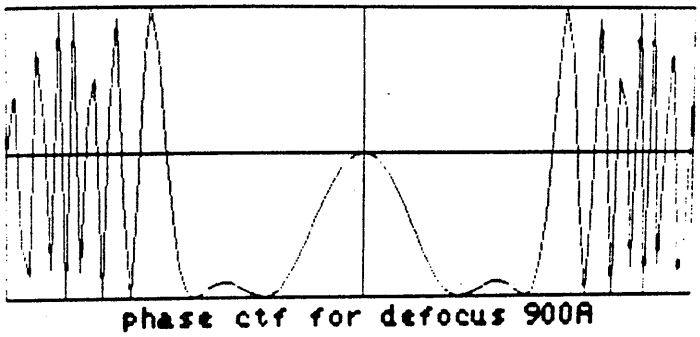
phase ctf for defocus 900A

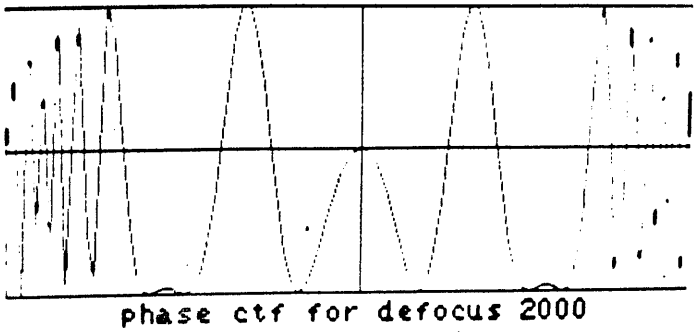
phase ctf for defocus 2000

Figure 2.2

record a 'focal series' of micrographs by successive alterations to the objective lens defocus. In this way, spatial periodicities not seen in one member of the series may well be seen in another, in addition to allowing the calculation of a variety of optical parameters, for example the effective coherence width of the illumination source (Frank (1973)).

The contrast of thin specimens is often found to be markedly dependant upon the coherence of the illumination. The coherence of a wavefield refers to its' ability to produce interference effects, the high resolution detail in an electron micrograph arising from coherent interference. The transfer functions described so far are those exhibited under perfect spatial and temporal coherence.

In reality however, the electron microscope has a finite source size and a gaussian distribution of incident electron energies. This lack of spatial and temporal coherence has been accounted for by the introduction of "envelope functions" in the expressions for the transfer functions. (Hanzen (1971), Hanzen and Trepte (1971), Misell (1973), Frank (1973) and Boerchia and Bonhomme (1974)).

An effective source size for an electron microscope can be defined as an imaginary electron emitter filling the illuminating aperture in the exit pupil of the second condenser lens (Hopkins (1957)). The coherence width is the distance, at the object, over which the illumination

may be assumed to be perfectly coherent. The coherence width X_c can be expressed as;

$$X_c = \lambda / 2 \pi \theta_c \qquad 2.2.4(v)$$

where θ_c is the semi-angle subtended by the illuminating aperture at the specimen, although this fails to take account of the condenser action of the objective lens pre-field. Temporal incoherence results from sinusoidal modulation of the high voltage system and objective lens currents and serves to limit the coherence length of the illumination.

The PCTF has therefore, to be modified to allow for the effects of partial coherence as shown below;

$$\text{Sin } \chi(s)_{\alpha,\varepsilon} = \text{Sin } \chi(s) \cdot E_\alpha(s) \cdot E_\varepsilon(s) \qquad 2.2.4(vi)$$

where $E_\alpha(s)$ is the damping envelope function representing limited coherence width and $E_\varepsilon(s)$ is the envelope function due to chromatic fluctuations; although this is an approximation as the partial coherence function is defocus dependent.

Frank (1973) and Fejes (1977) have shown the form of the envelope functions to be;

$$E_\alpha(s) = \frac{2J_1\left(\frac{2\pi}{\lambda}\alpha(C_s\alpha^3 - \Delta f\alpha)\right)}{\frac{2\pi}{\lambda}\alpha(C_s\alpha^3 - \Delta f\alpha)} \qquad 2.2.4(vii)$$

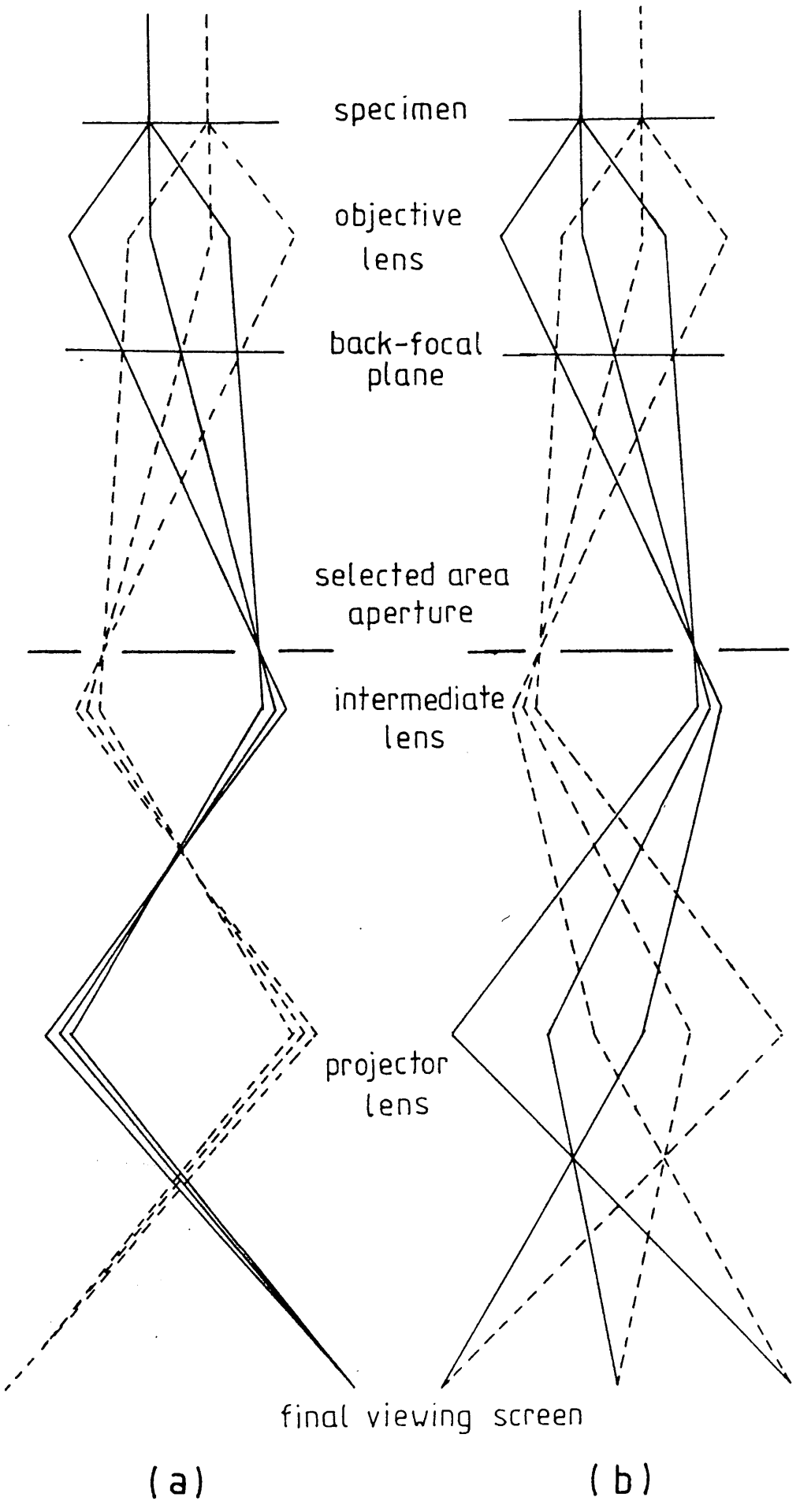
specimen
objective lens
back-focal plane
selected area aperture
intermediate lens
projector lens
final viewing screen
(a)
(b)

Figure 2.4

and

$$E_{\varepsilon}(s) = J_0\left(\frac{\pi\lambda}{d^2}\cdot\varepsilon\right)$$

where J_0 and J_1 are zero and first order Bessel functions respectively.

α - is the specimen illumination angle

ε - is the focal variation due to high voltage (V) and lens current (I) fluctuations, given by

$$\varepsilon = \left(\frac{\Delta V}{V} + \frac{2\Delta I}{I}\right) C_C \qquad 2.2.4(viii)$$

C_C is the chromatic aberration constant.

Figure 2.3, shows the same PCTFs as figure 2.2, this time incorporating the effects of the coherence envelopes.

In the preceeding description of the path of electrons from object to image a number of crucial approximations concerning the types of interactions between the electrons and the object, the properties of the imaging system (linear and isoplanatic) and the form of the contrast transfer functions were made. consequently, the results of image analysis and interpretation are only valid within the limits of these assumptions. Thankfully however, a large body of evidence has shown that, in the majority of experimental investigations, providing sufficient care is taken, these assumptions do hold.

A range of other factors can limit the acquisition of information from an electron microscope examination however and these are the subject of the next section.

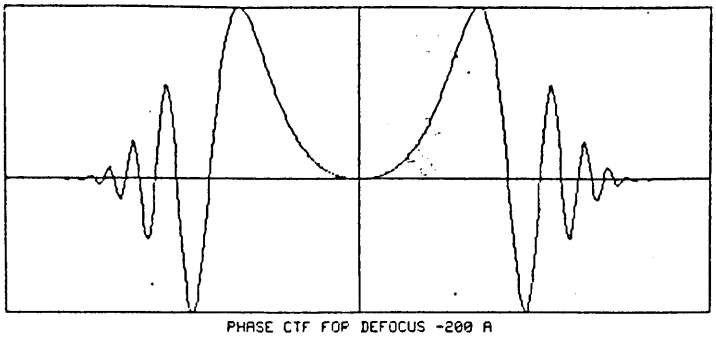

PHASE CTF FOR DEFOCUS -200 A

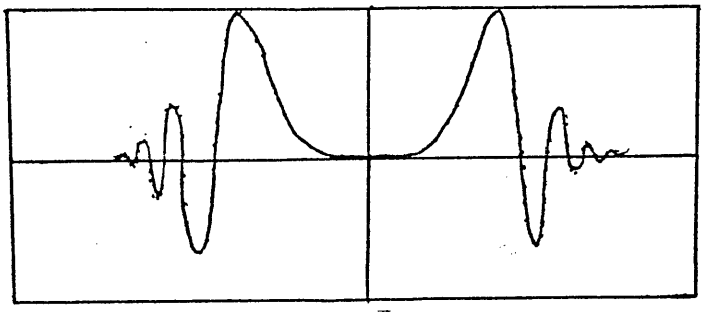

phase ctf for gaussian focus

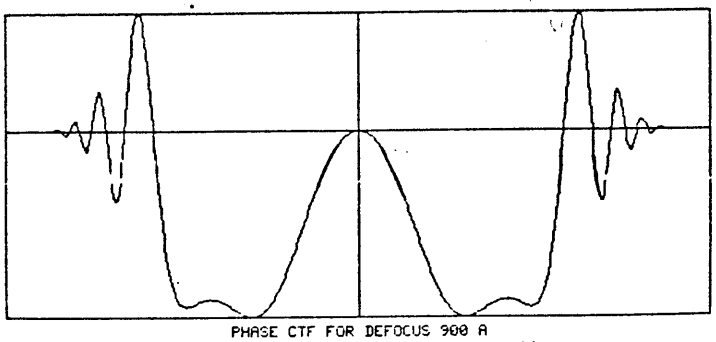

PHASE CTF FOR DEFOCUS 900 A

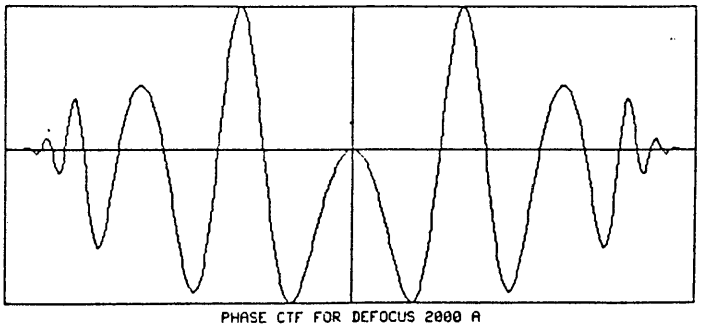

PHASE CTF FOR DEFOCUS 2000 A

Figure 2.3

2.2.5 FACTORS AFFECTING RETRIEVAL OF HIGH RESOLUTION INFORMATION

Astigmatism

Astigmatism is caused by an asymmetric magnetic field. A point is imaged by an astigmatic lens as two line foci at different points on the optical axis. It can be inherent in the lens from the machining of the lens pole-piece, or can be induced by the charging of contamination within the microscope column. All electron microscopes contain octopole stigmating lenses which can compensate for this defect to a limit that is governed, unless the defect is too severe, by the skill of the operator.

Specimen Contamination

The build up of amorphous, usually carbonaceous, material on the specimen and column sections can give rise to charging effects which obscure the specimen structure. Most modern electron microscopes are equipped with liquid nitrogen-cooled, anti-contamination jackets around the specimen area in order to condense contaminant vapours.

Specimen Stability

Electron beam irradiation will damage most specimens to some extent. In the case of organic and biological material, the sustainable radiation exposure is often the major, resolution limiting effect. As the materials

studied in this project were radiation sensitive, the problem of radiation damage will be considered more fully in the next section.

Mechanical Stability

Drifting of the specimen stage and mechanical and thermal vibrations can lead to a degradation in image quality. Modern microscopes are usually installed on secure mounts, with a hydraulic damping system supporting the column to minimize the effects of mechanical vibrations. Time for re-equilibration of the specimen is allowed when a new area is being examined or recorded, although this can often present problems when dealing with radiation sensitive materials.

2.2.6 RADIATION DAMAGE

The fundamental limitation to the collection of high resolution images of organic materials, or materials containing substantial organic moieties, is the degradation of the samples on exposure to the electron beam. Most, if not all, organic substances show changes in structure and properties resulting from exposure to ionising radiation. As this work is concerned with organic pigments, it would be useful to consider here, the various ways in which electron microscopical examination of the materials can be hampered by their radiation sensitivity and to mention some of the methods employed to alleviate the problem.

The subject of radiation damage has been extensively studied by a large number of workers using a variety of ionising radiations and techniques. This project, whilst being directly affected by the problem of radiation sensitivity was, nevertheless, not concerned with a study of the processes involved and therefore the purpose of this section is to provide a sufficient introduction to the problem of radiation damage, without attempting an extensive review of the current literature.

The phenomenon of radiation damage is primarily due to the inelastic scattering of the electron beam. Damage produced by elastic scattering events, such as "knock-on" collisions, have a far smaller probability and can therefore usually be ignored.

The energy imparted to the specimen by an inelastic collision may be dissipated by a number of processes which can be broadly categorised as ionisation (both valence and inner-shell), the formation of excited molecular states, the transfer of electronic excitation from one molecule to another, the dissociation of excited vibrational states, electron capture, neutralisation and radical reactions. In most cases a molecular ionisation event will result in some form of bond disruption in organic molecules as the excited vibrational states will dissociate in a very short time (on the order of 10^{-14} sec), precluding the possibility of recombination of the positive molecular ion with an electron from its' environment to form an electronically excited, but stable state.

Most organic systems are too complex to encourage detailed studies of the mechanism of their radiation decomposition, however, a few generalisations may be made about the types of reactions observed. A great variety of products can usually be found, for example gases such as H_2, CO and CO_2 molecular fragments and polymerisation products. Aromatic materials are however, considerably more resistant to the effects of radiation damage than aliphatic materials. This relative stability has been attributed to the delocalised nature of the molecular orbitals of the valence electrons in aromatic systems, which can distribute the effects of ionisation over the molecular network. In addition, excited electronic states of aromatic molecules have high probabilities for de-excitation by the emission of fluorescent radiation.

Aromatic hydrocarbons have also been shown to exhibit a protective influence over aliphatic hydrocarbons in a mixture of both (Friedlander and Kennedy (1962)). Energy absorbed by one part of a molecule may be transferred to other parts of the molecule or to a neighbouring molecule, by a process known as resonance energy transfer.

The excited molecular species produced by the primary radiation damage processes can then undergo secondary chemical reactions, often involving many neighbouring molecules in a complex series of steps.

One other phenomenon worth mentioning here is the so-called "cage effect" exhibited by substituted aromatic

hydrocarbons, where molecular fragments or atoms, released by radiation damage processes, remain localised because of a lack of accessible diffusion routes. Murata et al (1977), demonstrated this effect by obtaining high resolution, molecular images of chlorinated copper phthalocyanine, showing that the radiation damage took place preferentially at edges and voids of the crystal, where molecular fragments could easily diffuse from the matrix.

The above processes however all lead to the same result; that is loss of structural information due to the degradation of the crystal structure of the material. An electron microscopist, working with beam sensitive specimens then, is concerned with imaging the specimen before it is destroyed or seriously altered by the irradiating electrons. For organic materials, a critical dose of only a few C cm^{-2} must not be exceeded in order to obtain reliable structural information. The consequence of this restriction is that large, statistical fluctuations in the number of electrons that form each picture element, leads to poor statistical definition in the image. In order to visualise a feature in the image, the coherent contrast must exceed the statistical fluctuations by the minimum acceptable signal to noise ratio (S/N);

$$C_d \geqslant \frac{S/N}{\sqrt{n}} \qquad 2.2.6(i)$$

where C is the image contrast, d is the object size and n is the total number of electrons passing into a given

image point (picture element) (Glaeser (1971)).

One way to improve the shot noise limitation is to utilise the redundancy of information which is present in an image of an ordered array of identical objects. Superimposition, provided that a large enough number of objects was used, would then produce an "average" object, with a greatly improved signal to noise ratio, as only the signal would correlate from one object to the next. (Unwin and Henderson (1975)). With the advent of computer image processing techniques, great efforts are being made to facilitate this averaging approach and some of the techniques used are described in chapter 3 of this thesis.

Obviously, the development of techniques which prolong the lifetime of the specimen in the electron microscope is another approach which can be used when dealing with beam sensitive specimens. Encapsulation of organic crystals in a thin, evaporated layer of carbon, gold or aluminium (Salih et al (1974)) and SiO, carbon, and hexabromobenzene (Fryer and Holland (1983),(1984), Holland et al (1983)) have been shown to reduce their radiation sensitivity appreciably. Minimal dose techniques (more fully described in chapter 4) are now well established, in which the area of interest is only irradiated when recording the image. (Williams and Fisher (1970), Unwin and Henderson (1975)).

Ionising radiations produce less damage on cooled material and so a considerable effort has been made in the

development of cryomicroscopy. Improved stabilities have been observed by many workers on organic crystals at low temperatures, for example, Dubochet et al (1981), Knapek (1982) and Taylor and Glaeser (1976), although it would appear that significant gains in radiation stability for many materials are not made in lowering the temperature from 77K to liquid helium temperatures as reported, for example, by (The International Experimental Study Group (1986).

The use of higher accelerating voltages have been shown to reduce the rate of damage (Thomas et al (1970), Kobayashi and Reimer (1975)), in addition to increasing the thickness of the specimen with which it is possible to work.

2.3 SELECTED AREA ELECTRON DIFFRACTION

As already stated, the Fraunhofer diffraction pattern of the object is formed in the back focal plane of the objective lens. In the normal transmission mode, the projecting lens system (the intermediate and projector lenses) are focused on the intermediate image produced by the objective lens and magnify this image onto the observation screen. By altering the lens currents, the projecting lens system can be focused on the back focal plane of the objective lens, projecting the diffraction pattern of the object onto the final screen. For periodic specimens, for example crystalline materials with crystal

planes parallel to the electron beam, the electron diffraction accords with the Bragg Law and so the reciprocal lattice can be viewed.

Selected area diffraction can be achieved by the insertion of an aperture into the column at the first intermediate image plane and hence be used to delineate a small area of the specimen, as shown in figure 2.4.

In the diffraction mode, the electron microscope can be considered to be a simple electron diffraction camera. As shown in figure 2.5, discrete diffraction spots or rings will occur when the incident electrons are diffracted by a crystal plane or planes, lying at an angle to the incident beam, which satisfies the Bragg Law. From the diagram;

$$\tan 2\theta = D/2L \qquad 2.3(i)$$

The Bragg Law for first order diffraction (n=1) is;

$$\lambda = 2d\sin\theta \qquad 2.3(ii)$$

and since θ will be small (usually less than 3°), the approximation,

$$\tan 2\theta = 2\sin\theta = 2\theta \qquad 2.3(iii)$$

may be invoked to obtain;

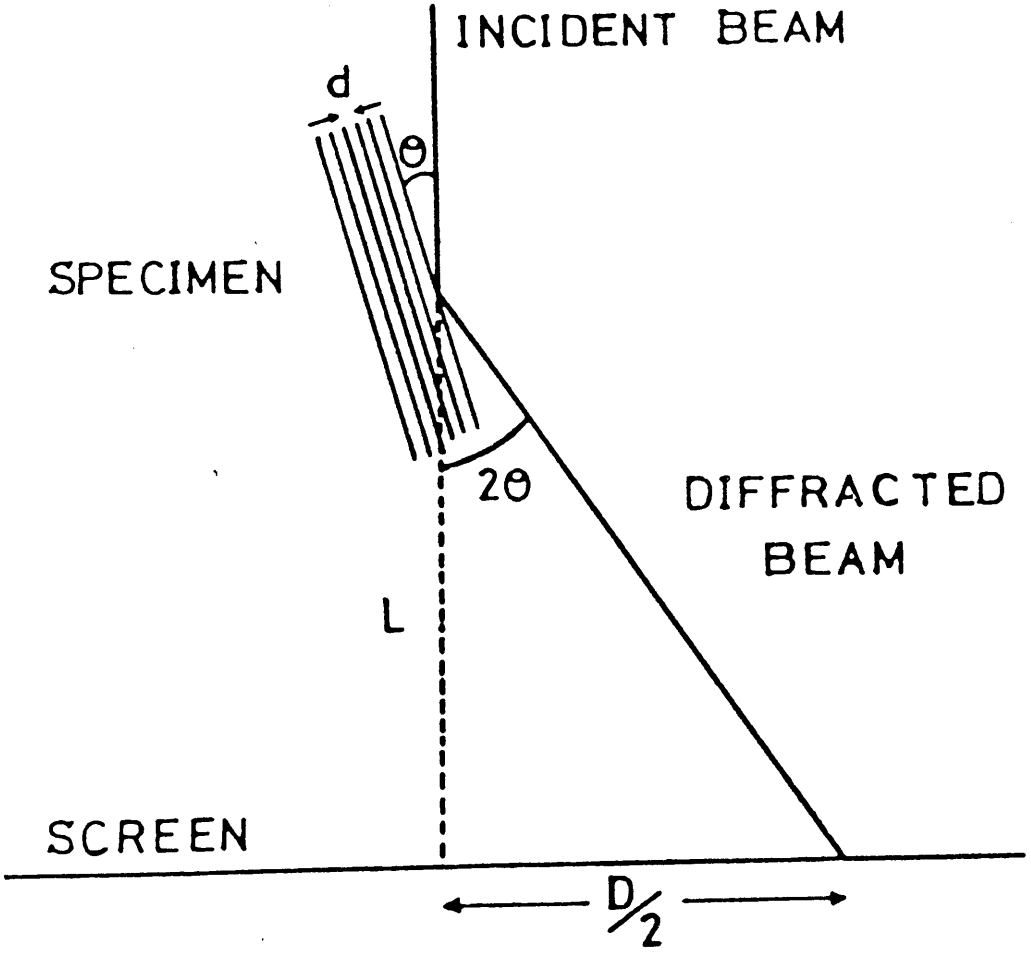

Figure 2.5

$$Dd = 2\lambda L \qquad 2.3(iv)$$

where $2\lambda L$ is the so called camera constant. L is the effective camera length and is given by;

$$L = f_o . M_1 . M_2 . M_3 . M_4 \qquad 2.3(v)$$

where f_o is the focal length of the objective lens and M_1, 2, 3, 4 are the magnification values for the intermediate and projector lenses.

The information obtainable from electron diffraction patterns is extensive. The camera constant is determined by the use of a standard specimen where the interplanar spacings are accurately known (normally the Au or TiCl reflections). Unknown diffraction patterns can then be identified by comparison of the list of interplanar spacings obtained with tabulated x-ray data in the A.S.T.M. powder diffraction index, often giving the exact composition of the specimen. Careful experimental procedure in the setting of post-specimen lens currents and the specimen height, can yield lattice spacings to within an optimum 1 - 2% accuracy.

The symmetry of the diffraction patterns may, in many instances, lead to the determination of the crystal class, and occasionally the space group, to which the specimen belongs. Formulae are available which allow calculation of interplanar spacings, angles between crystal planes, zone axis orientation and inter-zone axis angles for the common

crystal systems. Orientation relationships between precipitates, inclusions or twinned crystals and any surrounding matrix and between two single crystals in a polycrystalline sample may be investigated, along with the crystalline orientation of crystal defects of all kinds (dislocations, stacking faults, voids, boundaries). more comprehensive treatments of these topics are contained in the work of various authors, for example Andrews et al (1967), Beeston et al (1972) and Hirsch et al (1965).

This easy to understand, geometrical approach to electron diffraction can therefore provide much useful information, particularly for the identification of microcrystalline materials embedded in a matrix. The diffraction of electrons by a substance however, yields considerably more information than already suggested. The diffraction intensities may be used to reveal structure factor values for the crystal under investigation and therefore provide a basis for an ab initio, crystal structure analysis.

This possibility can be more readily appreciated by considering, once more, the interaction of the incident electron beam with the specimen. As already mentioned, in section 2.2.3, the elastic scattering of electrons can be modelled in several ways. The kinematical diffraction theory relates the diffracted wave intensities to the structure factor amplitudes in a simple manner, if the kinematical approximation can be said to hold. The constraints for this model however, mean that often the measured diffraction intensities are not proportional to

the square of the structure factor amplitudes, hence a dynamical scattering theory, including factors to allow for crystal deformation and inelastic and incoherent scattering for example, must be used.

Taking equation 2.2.3(i), the transmission or propagation function for an electron wave through a specimen is;

$$\psi_t(x,y) = \psi_o \exp(i\sigma\phi(x,y)\,\Delta z \qquad 2.2.3(i)$$

and where,

$$\phi(x,y) = \int \phi(x,y,z)\,dz \qquad 2.3(v)$$

is the projection of the potential distribution, for a thickness Δz of the specimen, in the beam direction.

The expansion of this expression yields;

$$\psi_t(x,y) = 1 - i\sigma\phi(x,y)\Delta z + \frac{\sigma^2}{2!}\phi(x,y)^2\Delta z^2 + \cdots\cdots \qquad 2.3(vi)$$

The Fourier transform of 2.2.3(i) is then;

$$\psi_d(h,k) = F(\psi_t(x,y)) = \delta - i\sigma\Delta z F(h,k) + \frac{\sigma^2\Delta z^2}{2!}F(h,k)\cdot F(h,k) + \cdots \qquad 2.3(vii)$$

In the kinematical approximation then, the measured intensities of the diffraction spots are simply related to the structure factor amplitudes only if the first term of the expansion is important. In other words, when the weak phase approximation, $\sigma\phi(x,y)\Delta z \ll 1$, holds.

The Structure Factor is defined as;

$$F(h,k,l) = \sum_j f_{e_j}(s)\, e^{2\pi i \underline{s}.\underline{r}} \qquad 2.3(viii)$$

where, f_{e_j} is the electron scattering factor for atom j, $\underline{s}.\underline{r} = hx/a + ky/b + lz/c$, hkl are the miller indices of the diffracted beams, and x /a, y /b, and z /c are the fractional unit cell coordinates of atom j.

The measured Structure Factor amplitudes can therefore be seen to depend upon the accelerating voltage (in the interaction term), the atomic numbers in the unit cell (through $f_{e_j}(s)$) and the crystal thickness ($n\Delta z$). The kinematical approach may often be used when considering organic materials then, as the atomic numbers of atoms in the unit cell are generally small and crystal thicknesses not too large.

Where these constraints are not met, the diffraction intensities measured can only be described by the application of a dynamical model for electron scattering, as all of the additional terms in equation 2.3(vi) become important.

The most widely used model is that formulated by Cowley and Moodie (Cowley and Moodie (1957)) and deals with the successive propagation of the electron beam through "slices" of crystal potential. In this case, the crystal structure is not simply related to the diffraction intensities due to the convolution of the diffracted beams

from successive slices. The image plane transmission function through n successive slices of a crystal is

$$\psi_t = (\psi_{n-1} * \exp(\frac{i k(x^2 + y^2)}{2 \Delta z}) \psi_n(x,y)$$

2.3(ix)

ψ_{n-1} is the transmission function after n-1 slices and ψ_n is that of the last slice. The Ewald sphere curvature is approximated for by the exponential term, where $k = 2\pi/\lambda$.

Dorset ((1978), (1980), (1983)), has shown that elastic bend deformation of the crystals can significantly alter the diffracted intensity. Whilst this should be accounted for by carrying out an n-beam dynamical calculation for the deformed lattice, the complexity of such a process (see Moss and Dorset (1982)) supports the approach of Cowley (1961), where the intensities are modeled using a kinematical, gaussian perturbation to describe the bend deformation.

Cowley and Moodie (1959) and Gjønnes and Moodie (1965), showed that symmetry information could be obtained from dynamical scattering situations in that the observed intensities depend upon the relative phases of the participating reflections. Translational symmetry elements resulting in systematic absences, would also be seen if the incident beam was parallel to the unique axes of these elements. If however, the translational symmetry element axes in successive slices were not exactly superimposed then the 'forbidden' reflections will appear, albeit weakly, in the diffraction pattern. This is best minimized

by using thin crystals.

Another phenomenon which alters the intensities, from those predicted by an n-beam calculation, is inelastic scattering of the incident beam.

The advances represented by the use of n-beam dynamical scattering theory, to describe the observed diffraction intensities, have led to the application of the technique to ab initio crystal structure analysis; for a review see Dorset (1985). Phase determination based on trial and error methods, Patterson functions, direct phasing and potential energy minimisation have all been used in crystal structure analyses of long-chained organic materials. Furthermore, phase retrieval procedures using electron microscope images are continually being developed and may provide another method for determining the phases of reflections in electron diffraction patterns. Hence, quantitative crystallographic analyses, for materials which cannot be crystallized adequately for standard x-ray analysis, are a distinct possibility.

CHAPTER 3: COMPUTER PROCESSING OF ELECTRON MICROSCOPE IMAGES.

3.1 INTRODUCTION

The use of either optical analysis, (as explained further in section 4.5.1), or computer analysis of microscope images, allows assessment of electron optical parameters to be made. For images of well-ordered specimens, image analysis based on Fourier methods, gives an indication of image resolution and specimen preservation as well as providing a means of image enhancement whereby structural details, obscured by noise, may be visualised. Digital computer processing, whilst initially costly both in time and resources, is reliable and in most cases easy to use. Many complex tasks can be performed and iterative procedures applied to many micrographs, with a flexibility which cannot be matched by optical methods.

Computer analysis of low dose images of the calcium 4B toner crystals was confined to "transform masking", or spatial averaging, in this work to improve the signal to noise ratio problem, mentioned already in section 2.6 dealing with radiation damage. The impressive use of computer techniques demonstrated by many workers, particularly in the three-dimensional reconstructions of biological macromolecules as shown, for example, by Unwin

and Henderson (1975) and Grano (1979), were beyond the scope of this project and whilst providing possible directions for future applications of computer processing to the problem of imaging small organic molecules, will not be discussed in this thesis.

The aim of this chapter is to provide an introduction to those topics in computer image processing which were encountered in the course of this project. Consequently, conversion of the image to digital form, some aspects of discrete Fourier transformation, "averaging" of motifs in the image and an overview of the SEMPER image processing program (Saxton et al (1978))will be discussed.

3.2: DENSITOMETRY

In order to study images by computer, it is first necessary to translate the information that the micrographs contain into a form suitable for numerical processing. That is to say, the continuously varying optical density on the photographic plate, which is linearly dependent upon the electron exposure to around D=1 (Valentine (1966)), must be converted to a digital representation. This is achieved by measuring the optical density on a two-dimensional, square lattice of points, the distance between the points being called the "sampling interval", each measurement being averaged over a small area called the "sampling aperture". Several forms of scanning densitometer are available, ranging from fast, rotating drum instruments and those

based on ccd arrays, to slower, adapted one-dimensional instruments depending upon requirements and cost. Details of the densitometers used in this work are given in chapter 4 along with a description of a system based upon a T.V. camera.

The sampling aperture blurs the micrograph before the sample values are taken. This corresponds to an attenuation of the high frequency detail from the image transform, as will be seen shortly. Generally square apertures are used, with the aperture size and sampling interval equal so as to limit noise levels. A sampling interval of half the image resolution is in theory sufficient, but a smaller interval is necessary in practice as a 50 μm scan might fail to detect a 100 μm periodicity completely.

The size of the sampling interval then is a major factor in determining the resolution attainable in the computer represented image. To understand how accurately the digitised image represents the original electron image and how the choice of sampling interval and aperture can affect that representation it is necessary to look at the mathematical relationship between the sampled and continuous functions. This subject and the subsequent section on discrete Fourier transforms has been fully treated in several works; for example, Saxton (1978), Misell (1978), Goodman (1968), Hawkes (1980), Rosenfeld and Kak (1976) and Grano (1979).

A continuous function g(x), may be sampled on a rectangular grid as shown in figure 3.1(a-e). Mathematically, this is expressed by multiplying g(x) by a comb function s(x).

$$s(x) = \sum_n \delta(x - n\delta x) \qquad 3.2(i)$$

The Fourier transform of the sampled function is then the convolution of the Fourier transform of g(x) (ie G(s)) and the Fourier transform of the comb function s(x) (ie S(s)).

$$G_{samp}(s) = G(s) * S(s) \qquad 3.2(ii)$$

The Fourier transform of a comb function of period Δx is also a comb function, but of period $1/\Delta x$. The convolution therefore may be visualised as the nett effect of distributing G(s) in accordance with the spacing shown in S(s), (figure 3.1(f)), or mathematically;

$$G_{samp}(s) = G(s - n/\Delta x) \qquad 3.2(iii)$$

G(s), and consequently g(x), can therefore be approximated by considering that part of $G_{samp}(s)$ centered at n=0.

In this case, G(s), is a band-limited function, (non-zero over a limited area), and so a single copy of G(s) can be obtained without overlap contributions from neighbouring copies centered at n=+/- 1, +/- 2, +/- 3 ..... By inspection, if S_{max} is the highest non-zero Fourier component of G(s) then a sampling interval of $\Delta x \leqslant 1/2S_{max}$ will ensure no overlap.

FIGURE 3.1

Comparison of the continuous and discrete Fourier transforms

(a) Continuous object function, g(x)

(b) Its continuous Fourier transform G(s) band-limited at s_{max}

(c) and (d) A comb function for sampling and its Fourier transform

(e) The "discrete" object results from multiplying (a) and (c)

(f) The continuous transform results from convolving (b) with (d). x was chosen so that the band-limited transforms do not overlap.

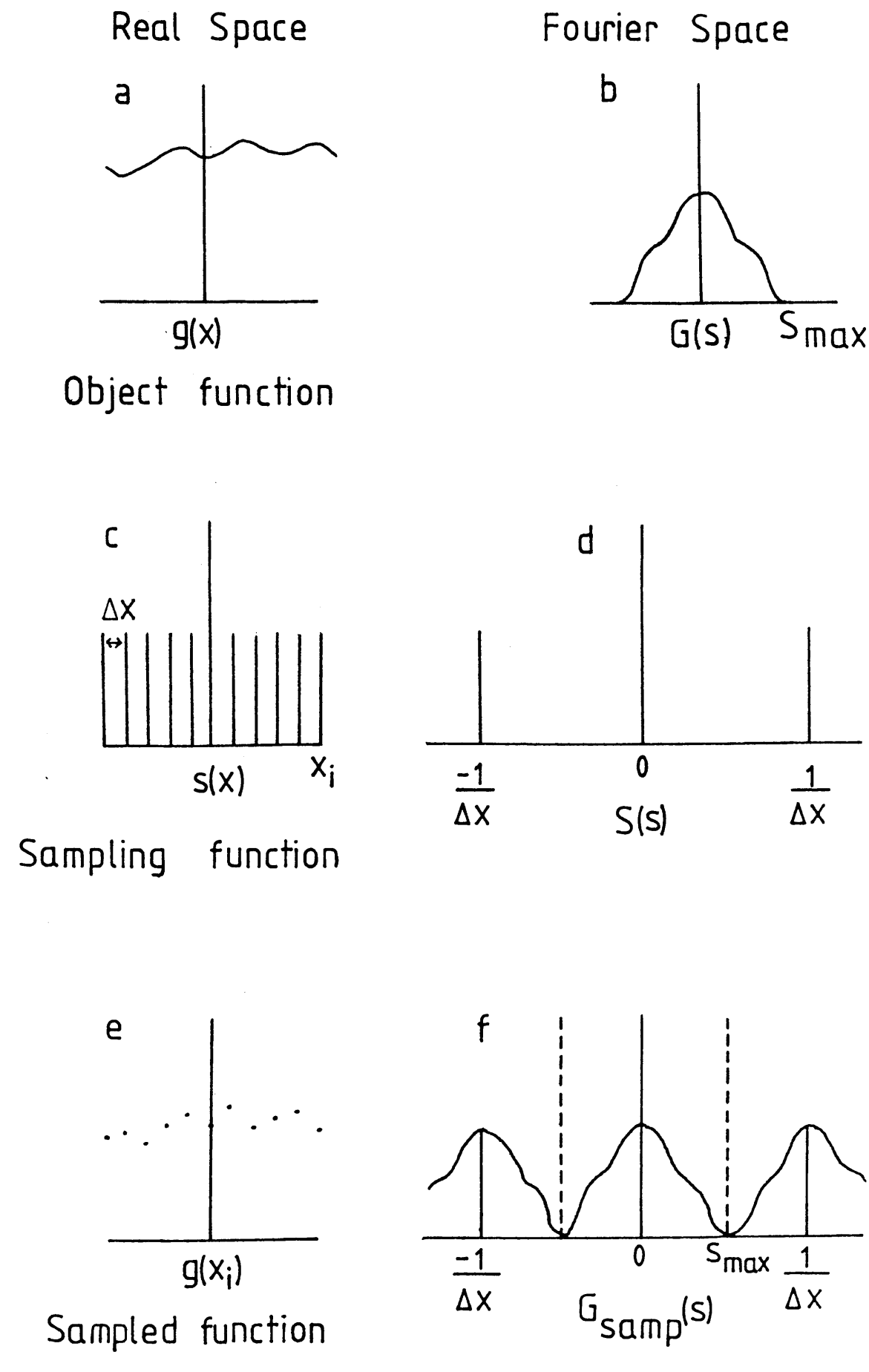
Real Space
Fourier Space
a
b
g(x)
G(s)
S_{max}
Object function
c
d
ΔX
s(x)
x_i
-1/ΔX
0
1/ΔX
S(s)
Sampling function
e
f
$g(x_i)$
-1/ΔX
0
S_{max}
1/ΔX
$G_{samp}(s)$
Sampled function

Figure 3.1

It follows then that no comb function separation is sufficient to prevent the overlap of neighbouring continuous transforms where a function is not band-limited as such a function has a non-zero transform for all s. This is known as aliasing and implies that the true continuous transform G(s) of a non-band-limited function can not be found from the sampled function.

Equation 3.2(iii) therefore becomes;

$$G_{samp}(s) = G(s) + G(s \pm 1/\Delta x) + G(s \pm 2/\Delta x) + \ldots. \qquad 3.2(iv)$$

where G(s) is the "true" value and the other terms are "aliasing" terms. The effect of the aliasing terms are important only if they are non-zero and of a similar magnitude to G(s). The smaller Δx becomes, the further the aliasing terms' frequency moves from the frequency of the correct term and so the smaller the effect of aliasing.

Microscope images are spatially limited functions and as such cannot be band-limited. Whilst the above therefore, suggests that "exact" representation by a sampled function is not mathematically possible, the magnitude of transforms of microscope images, at large s values, decreases rapidly and so the aliasing terms will be quite small. the sampling interval then should be chosen such that $\Delta x \leqslant r/2$ where r is the smallest resolved periodicity in the image. In practice, the sampling aperture used is around r/3.

The sampling aperture size reflects the area over which the optical density of the micrograph is averaged. As stated earlier, this averaging leads to an attenuation of the high frequency detail in the image, due to a convolution of the aperture profile with the image. The aperture size used is usually the largest possible such that no overlap between adjacent sampling intervals occurs and that the maximum area contributes to the sample, the effect of the attenuation being compensated for by the reduction in statistical noise.

3.3: THE DISCRETE FOURIER TRANSFORM

3.3.1 DEFINITION AND PROPERTIES

The discrete Fourier transform (DFT) is the heart of image processing. Indeed, it was the development of a fast way of calculating transforms which made digital image processing feasible at all. The DFT can be defined as;

$$G(n/NT) = \sum_{k=0}^{N-1} g(kT)\, e^{-2\pi i n k/N} \quad , n=0,1,2\ldots,N-1. \qquad 3.3.1(i)$$

where g(kT), k= 0,1....N-1 are samples of a continuous function g(x).

Conversely, the inverse transform is defined as;

$$g(kT) = 1 / N \sum_{n=0}^{N-1} G(n / NT)\, e^{i2\pi nk/N}, k=0,1,2....,N-1$$

3.3.1(ii)

The important feature of this transform pair is that they share the same properties as the corresponding continuous transform pair, the most important of these being listed below.

LINEARITY

$$DFT (f(kT) + g(kT)) = DFT (f(kT)) + DFT (g(kT))$$

3.3.1(iii)

COORDINATE ORIGIN SHIFTING THEOREM

If $DFT (g(kT)) = G (n / NT)$ then;

$$DFT (g(kT-x)) = G (n / NT) . e^{-\frac{i2\pi nx}{N}}$$

3.3.1(iv)

This shows that translation of a function preserves the amplitude of the DFT of the untranslated function but not the phase.

CONVOLUTION

$$DFT (\sum_{i=0}^{N-1} f(iT)g(kT-iT)) = F(n / NT). G(n / NT)$$

3.3.1(v)

ie the familiar result that convolution in real space is

equivalent to multiplication in reciprocal space.

CORRELLATION

$$\mathrm{DFT}\left(\sum_{i=0}^{N-1} f(iT)g(kT+iT)\right) = F^{*}(n / NT) \cdot G(n / NT) \qquad 3.3.1(vi)$$

The discrete correllation of two functions f and g. F^{*} is the complex conjugate of F.

The discrete autocorrellation follows by putting f=g. thus F^{*} .G becomes F^{*} .F and so the auto correllation function is given by the inverse transform of the power spectrum of the DFT.

3.3.2 THE CONSEQUENCES OF USING THE DFT

A discrete function may be considered to consist of a continuous function f(x), sampled at intervals defined by a comb function of spacing T, s(x), with an aperture function a(x), limiting the number of samples. (see figure 3.2) ie, the continuous function is;

$$f(x) \cdot s(x) \cdot a(x) \qquad 3.3.2(i)$$

By application of the convolution function to this modified function, the continuous transform would be;

$$(F(s) * S(s)) * A(s) \qquad 3.3.2(ii)$$

FIGURE 3.2

The discrete Fourier transform pair

(a) The continuous function f(x)

(b) The sampling function s(x) which is similar to the Fourier space sampling function $S_2(x)$

(c) The real space aperture function a(x) which delimits the object being subjected to the DFT.

(d) The continuous Fourier transform of f(x).s(x).a(x) the central portion of width 1/T sampled at 1/NT is the discrete Fourier transform.

(e) The continuous inverse Fourier transform of the (SAMPLED) discrete Fourier transform. The Fourier sampling has resulted in the periodic continuation of f(x).s(x).a(x). The central portion of width NT, sampled at T is the discrete inverse Fourier transform

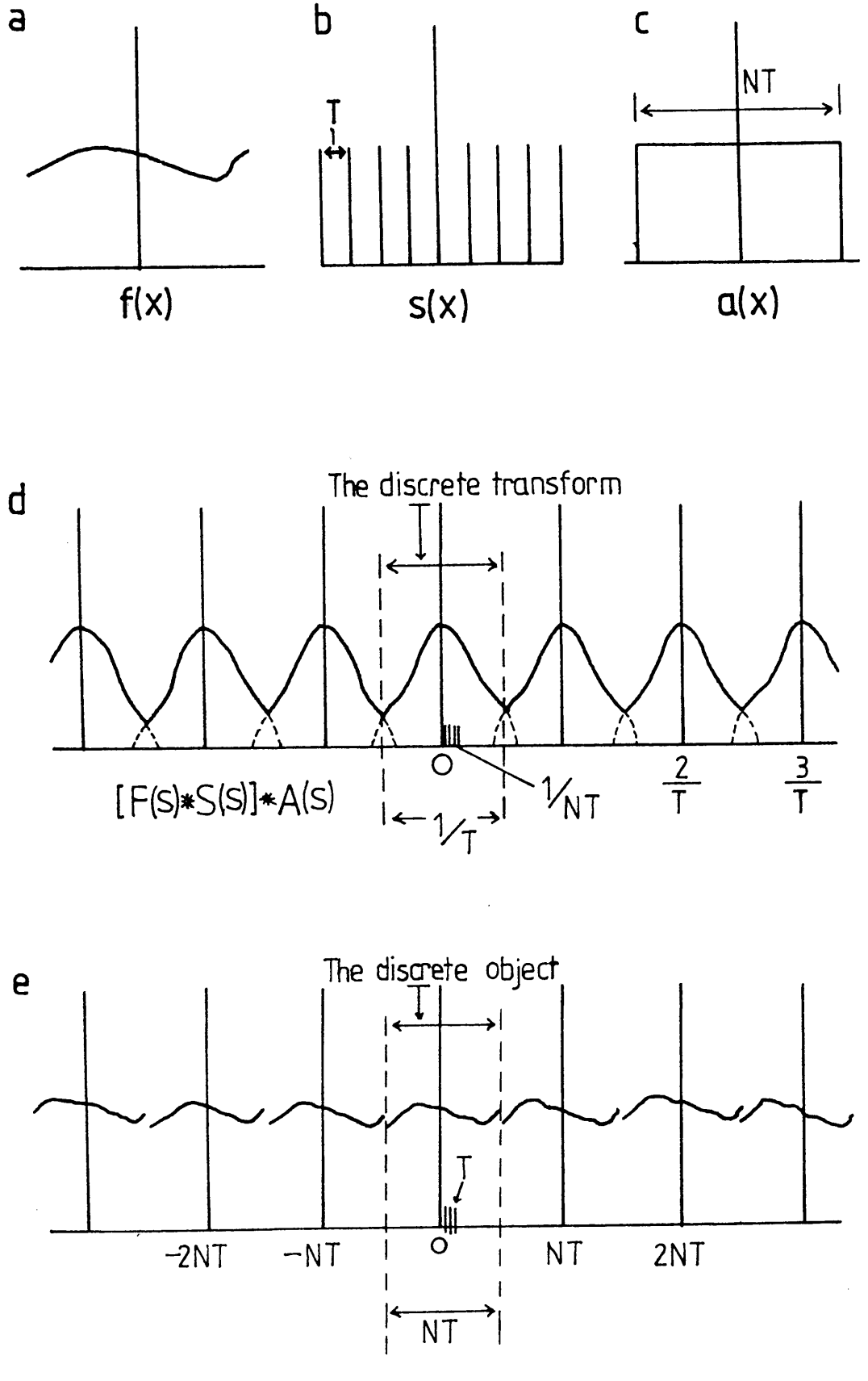
a
b
c
T
NT
f(x)
s(x)
a(x)
d
The discrete transform
T
O
1/NT
2/T
3/T
[F(S)*S(S)]*A(S)
1/T
e
The discrete object
T
-2NT
-NT
O
NT
2NT
NT

Figure 3.2

The discrete transform samples values of this transform on a comb function, say $S_2(s)$, of spacing 1 / NT, where N is the number of samples allowed by a(x).

Thus the dicrete function $f_2(x)$, is actually a periodic array of the original apertured and sampled functions.

$$f_2(x) = (f(x) \cdot s(x) \cdot a(x)) * s_2(x) \qquad 3.3.2(iii)$$

where $s_2(x)$ is the Fourier transform of $S_2(s)$ and consequently, is a comb function of spacing NT.

The periodic nature of the data in discrete transform processes means that image displacements in convolution or correllation for example are 'circular': that is to say that, what is shifted off one side of a picture reappears at the opposite side. This means that picture edges are often contaminated by the opposite edge after processing and should be discounted. Often the region of interest is masked-off within the picture.

The sampling of real space data is carried out over a length NT, where N is the number of samples at interval T. The Fourier space sampling must then be 1 / NT. Decreasing the sampling interval in real space results in coarser sampling in reciprocal space, for the same number of samples. This is why, in addition to computing cost considerations, there is no need to decrease the sampling interval below that which is necessary to resolve the smallest periodicity in the image without significant

aliasing problems, as decreasing the sampling interval for a given length of specimen leaves the Fourier space sampling constant.

3.3.3 THE DFT OF A PERIODIC SPECIMEN

There are two important cases to consider in the discrete transformation of a periodic image namely, sampling an integral number and a non-integral number of periods.

Both can be illustrated by considering the function $f(x) = \cos(2\pi g.x)$. The wavelength of this function is $1/g$ and consequently the continuous Fourier transform would contain peaks at $\pm g$. Sampling an integral number of periods m of this function, at a spacing T for a total of N samples, means that the Fourier coefficients are sampled at $1 / NT = g/m$. Thus the coefficients at $\pm g$ are sampled exactly, as shown in figure 3.3. The width of the discrete function ($NT = T_o$) results in the DFT being a convolution of the delta functions at $\pm g$ with a sinc function, $\sin(\pi T_o f)/\pi T_o f$. The zeros of this function will then occur at frequencies $g - i/T_o$, i = ...,-2,-1,1,2..... Therefore, apart from the sampling at m/T_o (the maximum convolution peak), all other discrete transform coefficients will be zero, as the zeros of the sinc function coincide with sampling points. Providing an appropriate sampling rate in real space was chosen, there will be little or no aliasing problems in Fourier space and so the advantage of sampling an integral number of periods

may be easily seen due to the lack of convolution problems (see figure 3.3).

The same situation does not apply to a non-integral period sampling. Here, $NT=T_o$ contains m+f periods of spacing 1/g, where $0 < f < 1$. Again the continuous transform would have peaks at $\pm g$, convolved with the sinc function as before. The problem however, is that $g = m+f/T_o$. Reciprocal space is sampled at intervals of $1/T_o$, therefore $\pm g$ will not be sampled. Furthermore, the zeros of the sinc function, still at $g-i/T_o$, i=...,-2,-1,1,2....., will also not coincide with sampling points. The convolution will therefore be sampled at f/T_o and $1-f/T_o$ in the main lobe of the function and at $1/T_o$ in the other lobes. The 'true' value of the convolution therefore, will not be obtained (see figure 3.4).

The problem can be alleviated to some extent however, by increasing the number of periods sampled, (ie. using a greater T_o). The attenuation of intensity caused by the missampling of the convolved peaks at $\pm g$ depends upon the shape of the sinc function. Whilst a greater number of repeats does not alter the intensity degradation, the greater T_o results in a better separation of the diffraction orders, due to a narrowing of the convolved sinc function. The larger T_o , the more peaked the sinc function becomes and hence the more local the effects of the convolution.

The 'true' amplitudes of the function may be obtained by

FIGURE 3.3

The discrete Fourier transform of a cosine wave

(a) A cosine wave of m periods in N samples.

(b) The continuous transform of this apertured wave, showing the aliasing effect and the convolved sinc function.

(c) A close-up of the transform centered at m/T_o. Note that neighbouring samples fall at the zeroes of the sinc function.

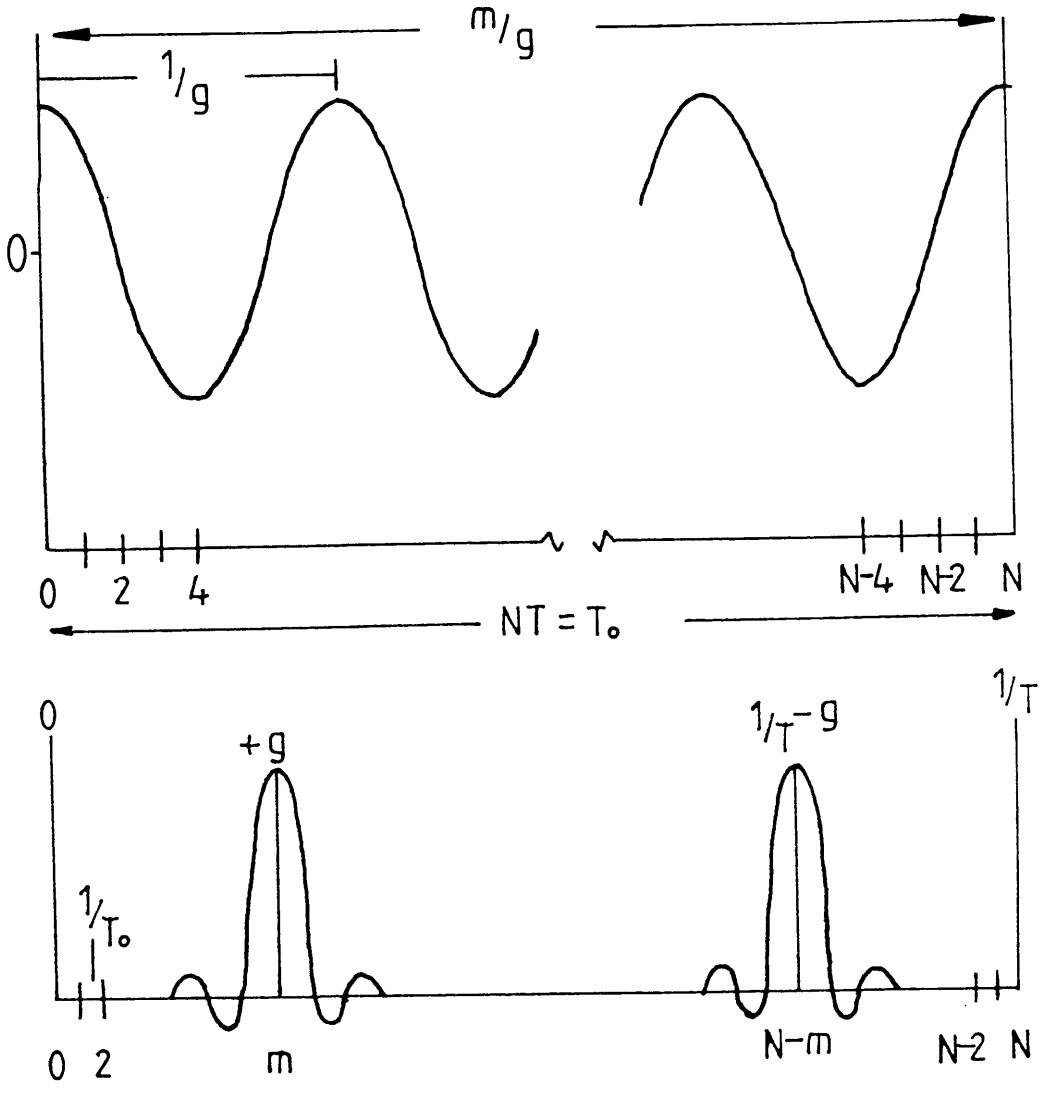
m/g
1/g
0
0 2 4
N-4 N-2 N
NT = T₀
0
+g
1/T₀
1/T
1/T - g
0 2
m
N-m
N-2 N

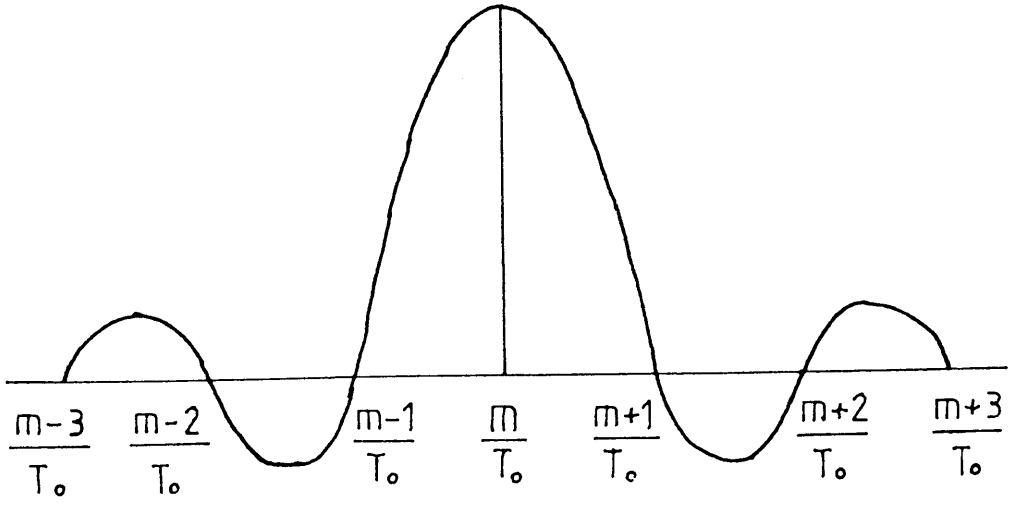
m-3/T₀
m-2/T₀
m-1/T₀
m/T₀
m+1/T₀
m+2/T₀
m+3/T₀

Figure 3.3

FIGURE 3.4

Part of the discrete Fourier transform of a non-integral number of periods of a cosine wave. The inclusion of (m+f) periods shifts the central peak of the convolved sinc function of the sampling lattice.

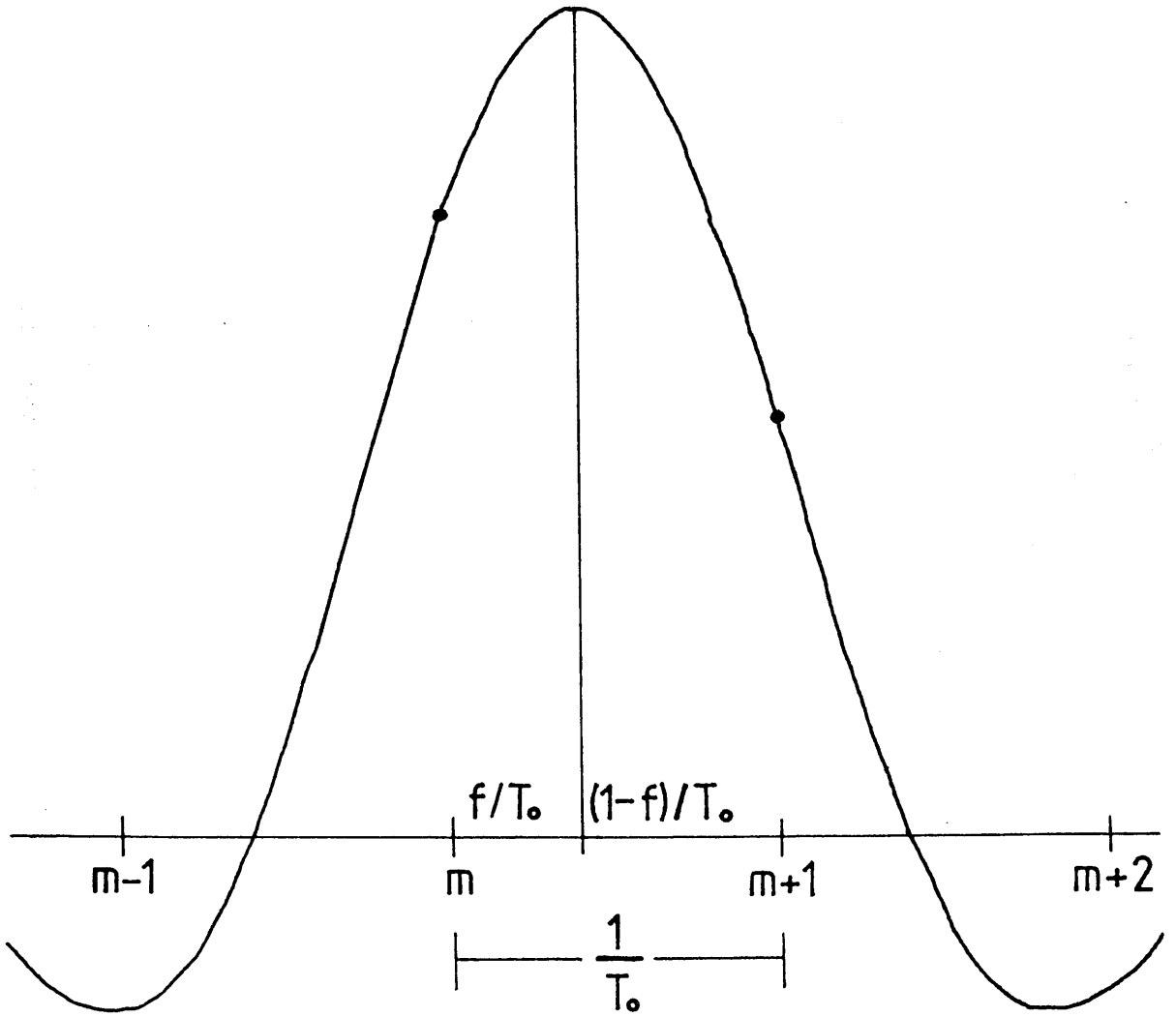

Figure 3.4

interpolating the original data onto a new sampling grid which will contain an integral number of repeats. One way of achieving this is by bi-linear interpolation (Aebi et al (1973)). Briefly, as shown in figure 3.5, to obtain a value at G from four values A,B,C,D, straight lines AB and CD are drawn, yielding values at E and F. A further line EF gives the value at G. The angular orientation of the unit cell axes with the picture axes is first carried out, followed by 'resampling' the original function to yield an integral number of repeats in the image. If necessary, as is often the case, the resampling may be given parameters such that there is an integral number of repeat units in the picture along both the picture axes.

3.4 FOURIER TRANSFORM FILTERING

The improvement in image signal/noise ratio has been given as the reason for employing computer processing techniques in this project. Averaging N repeats of a given signal will reduce the noise levels by a factor of $\sqrt{N}$. The simplest approach to this is a process known as photographic superposition (Horne and Markham (1972)), where identical motifs are superimposed by projecting the image onto photographic paper n times, making an exposure of 1/n th of the exposure required to make a normal print of the motif, and moving the image to project another motif between each exposure.

A useful way of averaging motifs in a noisy image,

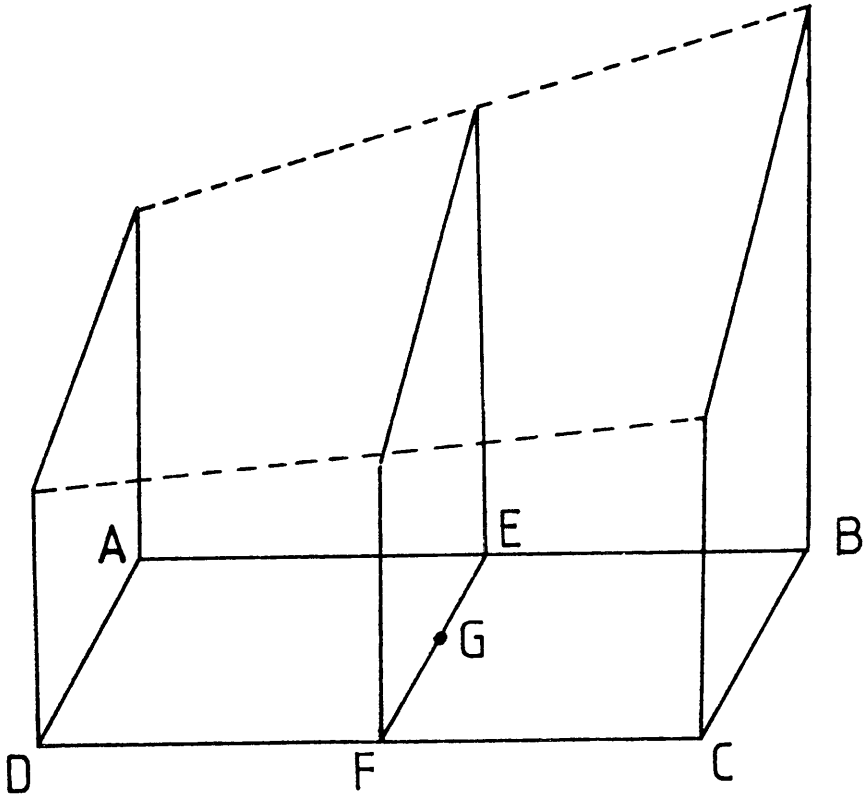

Figure 3.5

particularly if the signal to noise ratio is so low as to make visual recognition of the motif impossible, is to carry out a 'quasi-optical' filtration of the calculated image transform. The signal transform is localised around the reciprocal lattice positions, whilst the noise transform will be widely spread out. Imposing a filter mask consisting of an array of 'windows' around each spot will preserve only the information at the reciprocal lattice spots, thus removing most of the noise. As already shown, the signal transform spots will have a finite size of about the reciprocal of the size of the periodic region in the original image. Also, if the original image contains a non-integral number of repeats, then the centre of the spot will be spread over several points of the transform. For these reasons, an indefinitely small window (ie. one transform value- δ-function filtration) is not used to achieve an indefinitely good noise reduction as some of the signal would be excluded in the filtration. This would have the effect of averaging non-equivalent parts of the motif over a perfect periodic array and the result, whilst having apparent 'structure', would bear little resemblance to the actual motif. Using larger windows, reducing the improvement of the signal to noise ratio, has the advantage of including all of the signal and affecting 'averaging' over a more localised array of the motifs. The filtering process may be further constrained by constructing the transform mask such that a 'realistic' number of diffraction orders are included, based on consideration of such parameters as the degree of specimen preservation and the expected resolution of the image. The

procedure is shown diagramatically in figure 3.6.

Care must be taken to align the mask with the reciprocal lattice. Misalignment, either rotationally or with respect to scale will again result in non-equivalent parts of the unit cell of the periodicity being 'averaged'. Again, larger window sizes will limit the averaging to smaller areas and so slight misalignment over a few unit cells will result in almost equivalent parts being added together.

The filtered image obtained using a greater than delta function mask, being a local average, will often show lattice disorders and areas of radiation damage in the specimen. In addition, a low resolution filtration can often help to provide the necessary rotational and rescaling parameters for a subsequent interpolation step.

3.5 THE SEMPER IMAGE PROCESSING SYSTEM

All of the computer processing described in this thesis was carried out using the SEMPER image processing program (Saxton, Horner and Pitt (1979)). This is a composite program suite, comprising sets of precompiled routines which are called by an interpreter routine, as directed by the users' commands. The program structure is such that SEMPER assumes responsibility for the command language, picture management and handling, the diplay facilities and a range of many of the major operations required in image

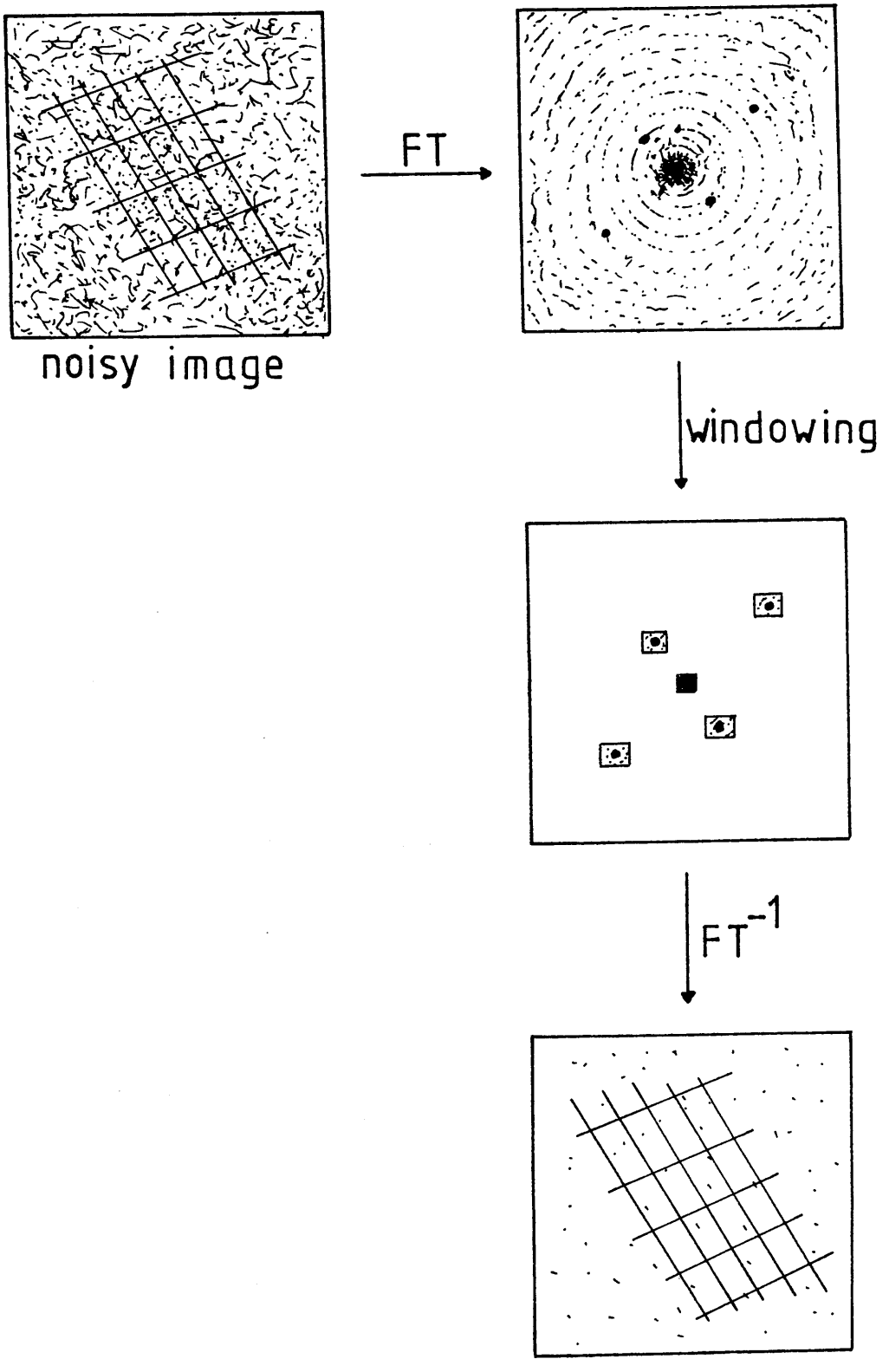

Figure 3.6

enhancement and analysis.

Operation of the system is carried out on two levels - interactive and non-interactive. Interactive use is the more natural procedure as we most commonly require to use our visual perception to assess a processed result. For example, on displaying an image, it may be found to be degraded by an intensity gradient and this can be remedied and the result displayed before further processing. In the interactive mode SEMPER, once started, asks for a line of input by issuing a prompt. The user types in SEMPER commands which are then executed before the cycle begins again. This process is repeated until a command is typed that ends the session or switches to non-interactive operation.

As in most other programming languages, SEMPER handles variables and expressions, conditionals, jumps and lables and simple for-loops, allowing a high degree of control over operational sequences.

The processing operations are supplied in the form of what are known as extension commands or "SEMPER VERBS". These follow a common, syntactic form involving verb NAMES, KEYS and OPTIONS. The verb NAME, identifies the operation to be performed. The KEYS set variables to the command which are usually defaulted unless set explicitly. The OPTIONS can be used to modify the action of the verb and require no value. An example of a typical SEMPER command is shown below;

FOURIER FROM = 1 TO = 2 REAL

FOURIER is the verb name and calculates the discrete Fourier transform of the image stored as picture 1 (Key FROM = 1), putting the result into picture 2 (key TO = 2) the option REAL forcing the verb to use only the real part of the source picture, (a valuable, time-saving option). The above command may also be typed FOU 1 2 REA, the variables FROM and TO being implied.

A note on the pictures used by SEMPER would not be out of place here. The pictures are stored as complex arrays of numbers using FORTRAN's floating-point data-type, representing picture brightness values sampled on a square lattice for example. They are limited in size to 512 by 512 pixels but may be freely dimensioned up to this maximum. The location of a pixel is identified by a pair of coordinates: '0,0' is the centre point, 'X,Y' the pixel X columns to the right, Y rows above the centre. The value of any given pixel is also represented by an expression pair, defining the real and imaginary parts of the complex value (a+ib). For images input from a densitometer, for example, the imaginary part will be zero and so the time in calculating the Fourier transform of such a picture will be considerably reduced by considering only the real part of the picture, (the reason for the option REAL, given in the example above).

Two versions of SEMPER have been installed at Glasgow. The first, on an ICL 2988 mainframe computer, stored pictures

in a 10 Mbyte, Fortran, direct access file and the second, a version of SEMPER called micro-SEMPER, running on an Olivetti M24 microcomputer, uses an 8 Mbyte file. In either case, a stored picture is identified by a number in the range 1 to 99 and are divided into several classes, for example;

Image class	picture	---------	class 1
Fourier class	picture	---------	class 3
Spectrum class	picture	--------	class 4

Changes in class on application of a particular routine is noted automatically and in many cases the class of a source picture directs the mode of action of the verb.

Indirect or 'off-line' operation is catered for in two ways; through the use of command 'procedures' and 'programs'.

Command procedures form the simplest way in which SEMPER commands can be stored for subsequent execution. The command ' TO n ' causes any commands on the current input line to be stored as a 'procedure' class picture n and can then be applied using the command ' DO n '. For example,

To 90; Survey N type log; Display N preset

defines a procedure for calculating a variety of picture statistics such as the mean value, reporting these values on the terminal screen, recording them in a file for

subsequent printing and displaying the picture. The command line;

for N 1,5; Do 90

would then apply the procedure to pictures 1 to 5 in turn. Procedure calls may be 'nested' (eg calling one procedure from another), but care must be taken to avoid confusion, a more sensible approach being to call each procedure as required, or if a more complex task is being carried out, to use a SEMPER program.

The use of SEMPER 'programs' allows a much greater degree of complexity than is allowed by procedures, however they must be defined prior to the session. The 'programs' are sequences of SEMPER commands sharing a common syntax, several of which may be combined in a single text file. Two program files, called RUN and LIBRARY, are attatched to a SEMPER session. Each program starts with a labelled comment and ends with a return statement. A command 'RUN NAME' will execute the program NAME, if present in the RUN file, (similarly for the LIBRARY file - 'LIBRARY NAME'). An example of a simple SEMPER program used at Glasgow is shown below.

```
1)      PICINPUT: C Inputs pictures from crystal system
2)      Overlay off
3)      Create display size 512 external noerase
4)      Ask ' Which picture number? ',p
5)      Copy display to p
```

6) Overlay on

7) Type ' Copy complete '

8) Return.

Line 1 gives the program name (PICINPUT) and a brief description of its' purpose. In this case, the program will input a picture 'grabbed' from an image intensifier camera and stored in a framestore to the micro-SEMPER picture disc. Line 2 switches off the display overlay (used in annotating the display pictures), enabling read-back from the display. Line 3 defines a picture of 512 pixels square without erasing the display area, classifying the picture as a SEMPER external class picture (the picture values being stored in byte format). Line 4 asks the user for the picture number that the image will be stored under and line 5 copies the 'grabbed' image to the SEMPER disc. Line 6 merely switches on the annotation facility again and line 7 reports completion of the task. Line 8 returns control of the system to the terminal for the next command line.

The above program is stored as a library program on the Olivetti M24 and can be invoked by typing LIBRARY PICINPUT (or LIB PIC as the interpreter considers only the first three characters of a word.).

Most of the operations performed during a SEMPER session are recorded in a text file which therefore provides a record of the session and which may be edited to become a program file of the type shown above. The record document,

or LOG, may also be written to freely by the user, which is of further help in, maintaining a record of the session.

Extensive on-line help facilities are also available, detailing most of the information about the system in several catagories, including the complete specifications for each SEMPER VERB.

Overall, SEMPER may be viewed as shown schematically in figure 3.7. The system is flexible enough to provide for most of the processing operations which are required for images (not only electron microscope images°) and the use of programs can allow very complex tasks to be performed by combining existing routines. If however, a particular operation is required which is not already catered for, or may be carried out more efficiently by a single routine, then the list of SEMPER verbs can be extended by writing a new FORTRAN routine for the operation, in a manner similar to the existing verbs. This new routine may then be incorporated into the system following a prescribed set of rules.

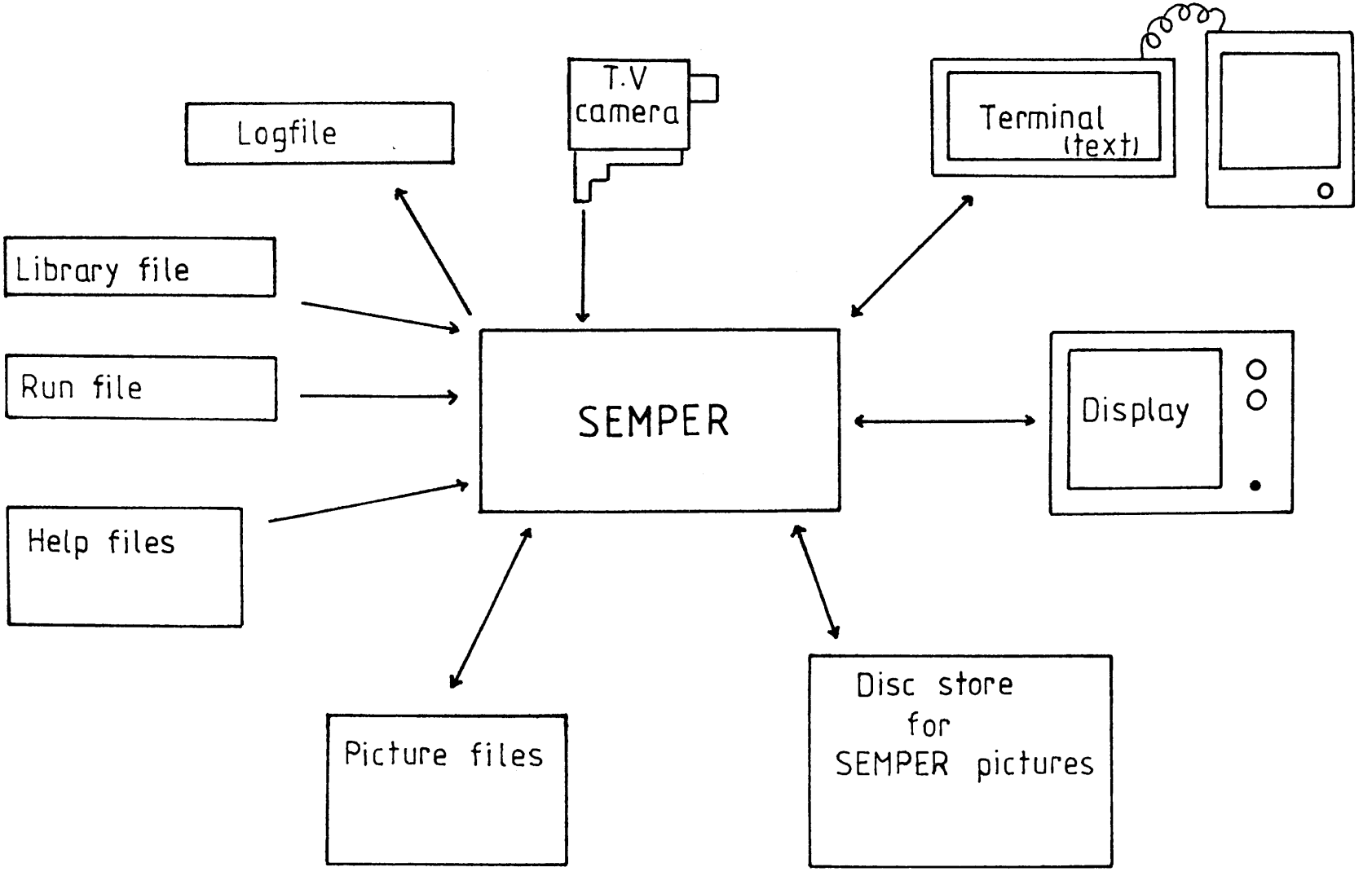
Logfile
T.V camera
Terminal (text)
Library file
Run file
SEMPER
Display
Help files
Picture files
Disc store for SEMPER pictures

Figure 3.7

and a fine end-point worked on the white solid diazo over 15 minutes.

9.4g of $CaCl_2 . 2H_2O$ in 50ml of water was then added and the resulting mixture stirred for 5 minutes.

(b) Coupling component.

9.4g of 3-hydroxy-2-naphthoic acid (β- oxynaphthoic acid - βONA) and 6g of NaOH were dissolved in 150ml of water at 35°C. The volume was then increased to 300ml at 25°C.

(c) Coupling reaction.

The coupling vessel was charged with 300ml of water and enough coupling component added to increase the pH of the solution to 10.9. The diazo and coupling components were then added simultaneously over 40 minutes to give a blue-shade red pigment slurry at pH 10.6. The simultaneous coupling procedure was used in order to allow the control of the pH to within very close limits and to keep the amount of the unstable diazo component exposed to the critical conditions of the coupling pH to a minimum. During coupling the pH was maintained between 10.5 and 11.0 using dilute HCl or a dilute NaOH solution as required. The pigment slurry was then stirred for 1 hour.

Addition of HCl reduced the pH to 7.3 and the slurry was then heated to 80°C over 15 minutes, during which time it became bluer and more fluid. At 80°C it was filtered and

washed chloride free with water. The resulting press-cake was weighed (yield 18g) and then separated into 3 parts.

(i) Major part - dried overnight at 90°C, yielding monohydrate blue shade pigment.

(ii) 2nd part - dried overnight at ambient temperatures yielding a dihydrate yellow-shade red pigment.

(iii) 3rd part - small sample taken from press-cake.

The preparation is shown diagramatically in figure 4.1.

4.2 Sample Preparation for Electron Microscopy

Initially, in order to avoid artefact, the pigments were dry dusted onto carbon-coated copper grids. Crystallite dispersion however was poor, with examination being limited to particles which had separated from the main crystal aggregates. Such particles may have been untypical and so further preparations were studied in order to improve the dispersion of the crystals.

Suspension of the crystals in water, alcohol or a water-alcohol mixture followed by immersion in an ultra-sonic bath was carried out and the suspensions applied to the carbon-coated copper grids by two methods. Firstly the suspensions were dropped onto the grids and then allowed to dry-down in air. Whilst improving on the "dry-dusting" preparation, crystal aggregation still occurred and so the method was altered such that the

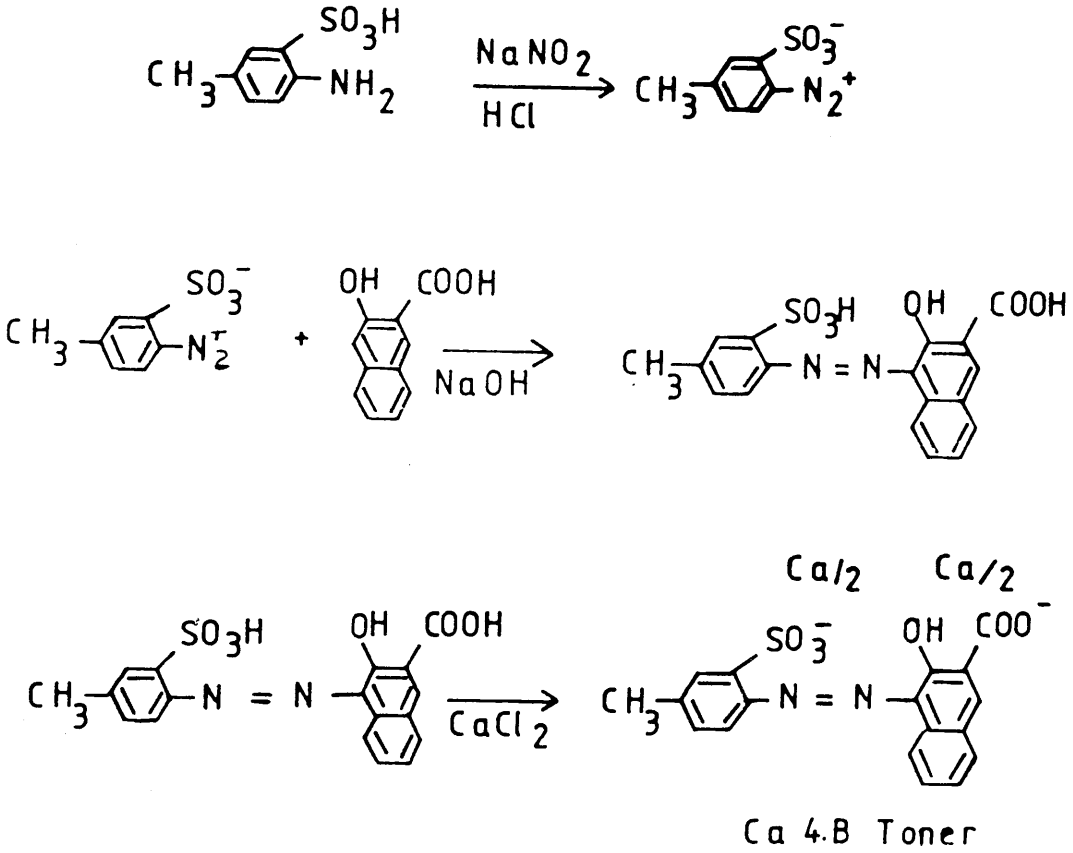

Ca 4.B Toner

Figure 4.1

crystal suspensions were sprayed onto the grids by microspray. The suspension of the crystals in water, immersion of the suspension in an ultrasonic bath and then micro-spraying onto the grids was found to produce the optimum dispersion.

Unfortunately, attempts at depositing thin films of calcium 4B toner by vapour epitaxy were unsuccessful, as degradation of the pigment occurred on heating.

4.3 Minimum Dose Electron Microscopy.

The high resolution studies were carried out at Glasgow using a JEOL 1200EX electron microscope which can be used for minimal exposure techniques. The sequence of operations used during the investigations are listed below.

The microscope was initially placed in the diffraction mode and, with the incident electron beam spread as far as possible, the specimen searched until a crystal, or group of crystals was found. The position of the specimen area was then recorded and, after switching the microscope to the imaging mode, moved out of the irradiated area. The illumination of the adjacent area was increased and focusing and astigmatism correction carried out with the aid of an image intensifier. (A Badger 25 television camera equipped with a YAG single crystal phosphor lens, connected to a green screen TV monitor.) The electron specimen area repositioned. The image was recorded on Ilford EM film or Kodak - Industrex C x-ray film by

realigning the beam. On the JEOL 1200 EX microscope, the operation is controlled by microprocessor, the operator setting the exposure intensity and time and correcting the astigmatism and focus.

The exposure times varied according to the later use of the images. Most of the calcium 4B toner images, used in the computer processing, were low-dose images; that is to say images recorded using an electron dose of only a few electrons per squared Å. Higher dose images of the same area were then obtained in order to observe the electron optical conditions, for example the presence of astigmatism and the focus setting.

The major experimental difficulty encountered using minimal dose techniques was that of obtaining images of the crystals at the focus position set. Due to crystal agglomeration, the areas selected without direct observation, were often at markedly different heights than the adjacent areas on which the microscope conditions were set. Many of the images obtained therefore were of limited value in the subsequent analysis.

4.4 X-Ray Powder Diffractometry.

X-ray powder diffraction patterns were obtained on a Siemens Crystalloflex diffractometer at Ciba-Geigy Pigments Ltd., Paisley and on a Philips x-ray diffractometer in the Geology department of the University of Glasgow.

4.5 Arrangements for Computer Processing at Glasgow.

4.5.1 Optical Diffractometry.

Preliminary scanning of the electron micrographs was carried out using an optical diffractometer similar to that shown schematically in figure 4.2 As well as providing a quick and inexpensive assessment of the quality of a given micrograph, areas suitable for digitisation could be found, providing a considerable saving in processing time and cost. For higher dose micrographs, the diffraction pattern produced in the optical diffractometer shows an eliptically shaped transform for the amorphous carbon support film, where the astigmatism correction was poor and loss of Fourier components in the direction of mechanical specimen drift, if present in the micrographs. The preserved periodicity of crystalline specimens may be evaluated and in the case of "low-dose" images, often provide the easiest means of finding areas for subsequent digitisation.

4.5.2 Densitometry.

Initially, the images were digitized using a Joyce-Lobel mark III CS flat bed microdensitometer with the kind permission of the Department of Natural Philosophy, University of Glasgow. In this system two beams of light are produced by a single source. One beam is transmitted by the area of the micrograph under examination and the

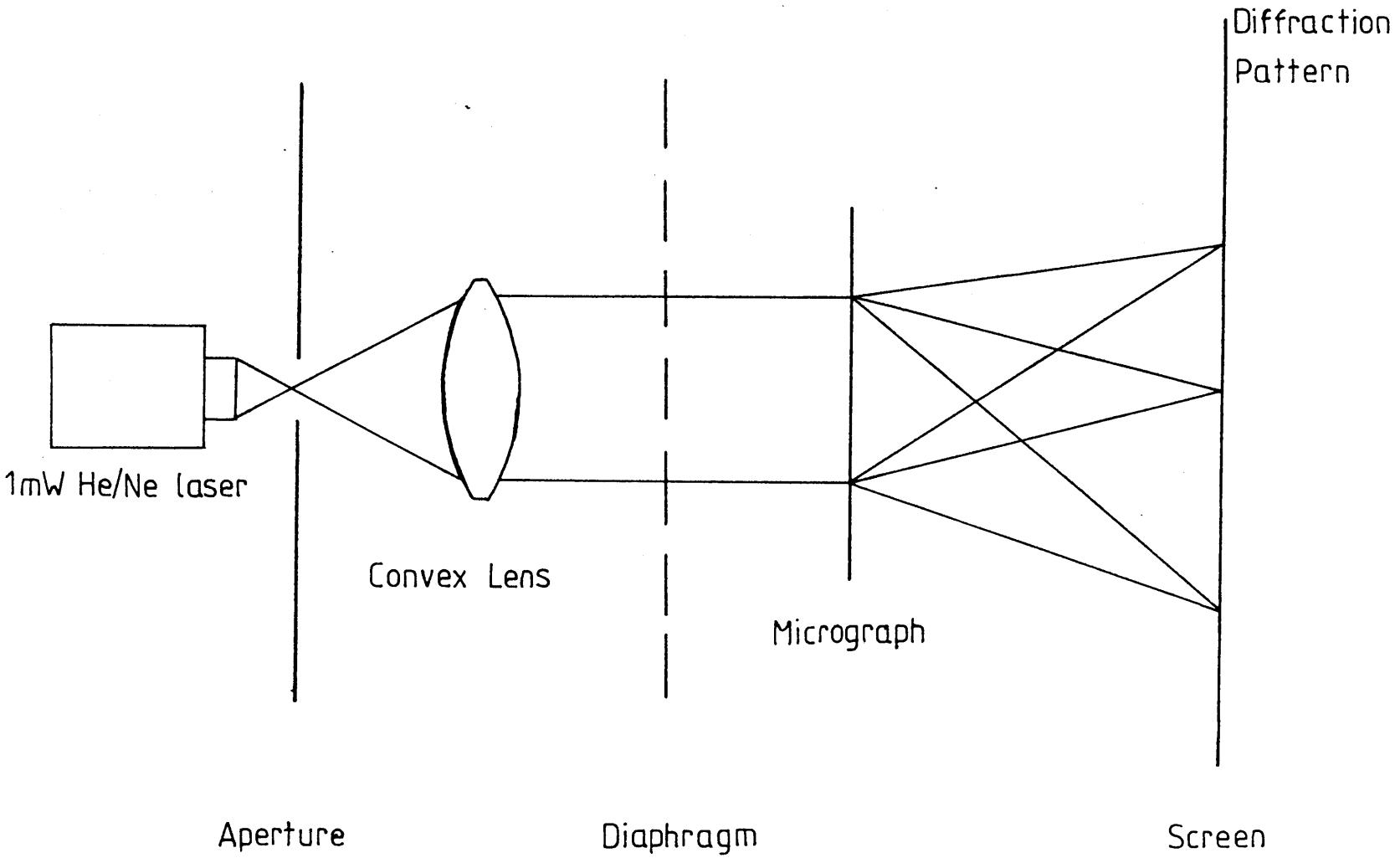
Diffraction
Pattern
1mW He/Ne laser
Convex Lens
Micrograph
Aperture
Diaphragm
Screen

Figure 4.2

other by a calibrated wedge in which the optical density varies linearly along its length. The two transmitted beams are then alternately measured by a photomultiplier detector, any difference between the two readings being used to generate an error signal. This controls a servo-mechanism which moves the calibrated wedge until the transmitted intensity in both beams is identical. The position of the wedge then determines the optical density of the area of the micrograph under observation. The size of the area being examined is governed by a pair of slits, which may be set to give sampling areas ranging from 5μm x 5μm to 100μm x 100μm.

The densitometer output the optical density readings by means of paper tape. This proved to be both cumbersome and very slow, (for example a 256 x 256 square image scan produced more than 100 meters of paper tape and required 4 hours to complete.) In addition, transferring such large amounts of data into the computer memory was not without hazard; the tape was sometimes misread and occasionally torn while reading.

Later, the images were sent to the SERC microdensitometry service at Daresbury. There, the images were scanned using a Scandig rotating-drum microdensitometer (for sampling aperture sizes of 25μm or greater) or a Joyce-Loebel mark 6 flat-bed microdensitometer (for sampling aperture sizes of 10μm), the digitized images being returned on magnetic tape. The Data Transfer Service in the Computing

Services Department of Glasgow University then read the tape into the computer memory.

A very recent development at Glasgow has been the direct acquisition of images from the image intensifier camera, mounted on the microscope, into MICRO-SEMPER, run on an Olivetti M24 microcomputer. A novel method of data collection using this system is described in section 4.5.4.

4.5.3 SEMPER INSTALLATION AT GLASGOW.

Initially, SEMPER was installed on the ICL 2988 mainframe computer running VME 2900. The display device used was a Sigma colour graphics terminal, connected initially via a 2400 and later via a 9600 baud serial line. The display device was used as both a text and a graphics monitor, switching between modes being freely operated by the user. The computer supports a large number of interactive users. The "SEMPER disc" was a permanent "direct access" file of 10 Mbytes and no magnetic tape use was supported.

The SEMPER primitives were written by Mr Jim Beck of the Glasgow University Computing Service. The display was in 16 grey levels and the maximum picture size set for 512 x 512 pixels. Compilation and relinking of the program modules were made easier by a series of control programs and all logical units were assigned on starting SEMPER by means of a command file.

The units attached to each SEMPER session were assigned as follows:-

Unit 1 .... SEMPERDATA (the SEMPER "Picture Disc")

Unit 2 .... Picture data

Unit 3 .... Command sequence

Unit 7 .... SEMPER library programs

Unit 8 .... SEMPER logfile.

Additional units, if required were assigned before starting a SEMPER session.

Several problems existed with the installation. Firstly, and most importantly the input of picture data was not established. The format of the microdensitometer output was edited by hand and then changed to FORTRAN 20I3 format by a simple FORTRAN routine. The picture data was input to the SEMPER disc by an edited version of the SEMPER routine PGT. Whilst this was by no means, an efficient method of data input, as it was slow and required very large amounts of disc space, nevertheless, without access to magnetic tape it was the only method possible. The same routine (PGT) also allowed output of SEMPER pictures provided that an output unit had previously been assigned.

Hard copy output was obtained by photographing the display.

An on-line colour plotter was available but, with false colours for each of the grey levels, produced confused, difficult to interpret images.

One or two routine software errors existed in the supplied source code. The REM routine for removing illumination ramps from SEMPER pictures tried to output on the unit used for input. On the ICL2988 this is not possible and the routine was edited accordingly. The SEMPER disc access primitive, MCDISC, was not writing to the correct memory areas with the result that data storage within the SEMPER disc between sessions was not possible. With the small picture sizes being used, the systems' virtual memory was sufficient for each session. The fault was later corrected, with the help and advice of Dr W O Saxton of the University of Cambridge and SEMPER ran as expected.

The latest installation is that of a form of SEMPER called MICRO-SEMPER, run on an Olivetti M24 microcomputer. The precompiled program modules were supplied on floppy disc by Synoptics Ltd of Cambridge and installation consisted of the fairly simple procedure of booting the system after copying the routines onto a 20Mbyte winchester and running the system regeneration program SEMACR.

4.5.4 A New Method for Collection of Images and Diffraction Patterns.

The installation of MICRO-SEMPER on an Olivetti M24 microcomputer equipped with an 8086 cpu, an 8087 maths

coprocessor board, a 20Mbyte Winchester, two monochrome display monitors (one green, long-persistance screen for image displays) and a "frame-grabbing" TV input board, has allowed the development of a novel method for the collection of electron microscope images and electron diffraction patterns. The input source for the "Frame-grabbing" board is the image intensifier camera mentioned earlier.

An electronic timing device, operating at millisecond levels, was constructed and connected to the electron gun deflector coils. When switched on, this device excites the coils so as to deflect the electron beam from the specimen area being examined. A series of switches then allows the deflection of the electron beam to be relaxed for a length of time determined by two potentiometers, which are set to the exposure time required, by the operator.

As an interface between the Olivetti M24 "frame-grabbing" board and the image intensifier camera, an image processing system called Crystal, supplied by Microconsultants Ltd., is used to hold the image until it can be passed to the M24 along standard video cables. The use of the Crystal system allows some degree of noise reduction to be carried out before passing the image to MICRO-SEMPER, by utilizing a supplied integration function, where an "integrated" image is obtained by summing the image over several frames of the TV scan.

This combination of computer-based hardware and software

has allowed the development of what has been termed a "fast exposure" technique of image collection (Fryer (1986)). Briefly, the microscope is operated as for minimum dose microscopy with the exceptions that, the incident illumination settings for recording the image are such that the beam is quite intense, and that when a desired area has been found, the fast timing device is switched on, after focusing on the adjacent area, to deflect the electron beam. The microscope screen is then raised and the minimum dose mode switched off. Collection of the image data proceeds by exposing the specimen to the beam for a time in the order of 50-100 msecs and collecting the image over a number of frames.

Electron diffraction patterns may be recorded by allowing the diffraction pattern to be imaged on the single crystal phosphor lens of the TV camera. Collection of the intensity data is achieved by integrating the "image" over a large number of frames of the TV scan (for example 2048 frames.) This image, stored in the Crystal system, may then be passed, via the frame-grabbing board, to MICRO-SEMPER, where the intensities of the discrete diffraction spots may be measured.

A preliminary analysis of this method of data collection is contained in the results and discussion section. (Section 5.).

CHAPTER 5: RESULTS AND DISCUSSION

5.1 Computer Processing

5.1.1 Results of Computer Processing of Images on the ICL 2988 Mainframe Computer

Images of chlorinated and brominated copper phthalocyanines were used at each stage in the computer processing in order to evaluate the procedures being used. These materials have well defined crystal structures, as explained in section 1.2, and so the results of the digital processing methods could be assessed against expected results. Plate 5.1(a) shows the original noisy image. The area for digitisation was chosen by scanning the micrograph on an optical bench. The digitised image was first floated to a mean picture density and 'masked-off' by a smooth-edged, circular mask to avoid shape transform problems. The Fourier transform and power spectrum of this prepared image were then calculated and the power spectrum displayed.

The wide range of values present in the power spectrum means that a thresholding procedure must be applied when displaying the result on a grey-level screen, otherwise the spectrum will be dominated by the high central values, making the reciprocal lattice difficult to visualise. Once the reciprocal lattice has been defined, parallellogram shaped 'windows' of a size related to the unit cell axes

Plate 5.1

(a) Original Image

(b) 'Windowed' Transform

(c) 'Filtered' Image

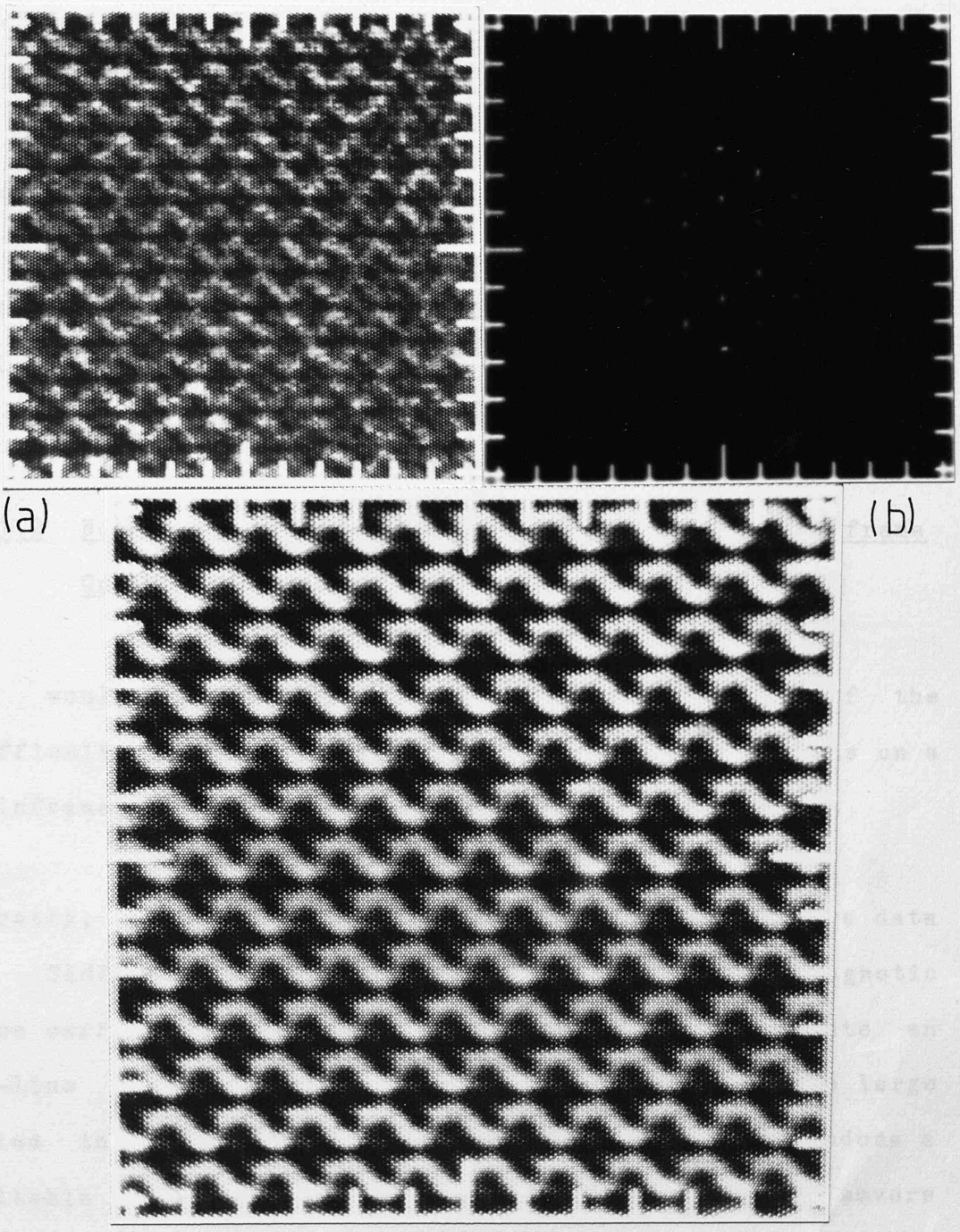
(a)
(b)
(c)

(usually 1/4 of the unit cell axes lengths) and with sides parallel to the axes directions, are placed around each reciprocal lattice position in the image transform to a realistic resolution (usually around 3Å) and the rest of the transform set to zero (see plate 5.1(b)). The inverse transform of this 'windowed' transform yielded the filtered result shown in plate 5.1(c).

The improvement in the visibility of the molecular columns is apparent and so the same procedures were applied to digitised, low-dose images of the calcium 4B toner crystals, as will be discussed in section 5.6.

5.1.2 Notes on Aspects of Image Processing on a Mainframe Computer

It would be appropriate here to discuss some of the difficulties encountered on processing the images on a mainframe computer.

Firstly, as mentioned in section 4.5, input of picture data to SEMPER was cumbersome. The paper or magnetic tape carrying the digitised image was first read into an on-line storage area of around 800Kbytes. These large files then had to be edited (manually!) to produce a suitable format for input to SEMPER, incurring quite severe restrictions on the amount of disc space available at any one time (and occasionally the wrath of the computer operators). The lack of on-line tape access resulted in

difficulties in archiving any of the processed pictures from within SEMPER. The only way this could be achieved was to write the data to another on-line file and then archive that by a batch job, usually requiring overnight running due to CPU restrictions.

The mainframe used was the central University computer and as such was heavily used by up to 100 users at any given moment. This inevitably led to processing times becoming alarmingly extended, even though CPU usage was not too high, due to demands on the time-sharing system. Simply displaying a 256 x 256 pixel image, for example, could take upwards of 20 minutes to complete. Admittedly, the calculation of Fourier transforms of images could be submitted as overnight batch jobs, however, the power of image processing lies in an interactive input by the human operator and this aspect can be severely hampered on a time-sharing system.

Finally, no hard copy devices were available to record the processed images. As detailed in section 4.5.3 therefore, Polaroid or 35mm photographs were taken of the graphics screen.

5.1.3 Results of Computer Processing of Images on the Olivetti M24 microcomputer

The acquisition of a microprocessor based, image processing system served to eliminate many of the practical

difficulties in archiving any of the processed pictures from within SEMPER. The only way this could be achieved was to write the data to another on-line file and then archive that by a batch job, usually requiring overnight running due to CPU restrictions.

The mainframe used was the central University computer and as such was heavily used by up to 100 users at any given moment. This inevitably led to processing times becoming alarmingly extended, even though CPU usage was not too high, due to demands on the time-sharing system. Simply displaying a 256 x 256 pixel image, for example, could take upwards of 20 minutes to complete. Admittedly, the calculation of Fourier transforms of images could be submitted as overnight batch jobs, however, the power of image processing lies in an interactive input by the human operator and this aspect can be severely hampered on a time-sharing system.

Finally, no hard copy devices were available to record the processed images. As detailed in section 4.5.3 therefore, Polaroid or 35mm photographs were taken of the graphics screen.

5.1.3 Results of Computer Processing of Images on the Olivetti M24 microcomputer

The acquisition of a microprocessor based, image processing system served to eliminate many of the practical

difficulties encountered on using the Mainframe computer. Whilst the processing power of a 16 bit microcomputer is several orders of magnitude lower than that of a 32 bit, virtual memory based mainframe, the advantages of having a dedicated system more than compensates for this with respect to the time required to process each image.

As in the case of the mainframe processing, copper phthalocyanines were used to test the system and to show the effects of various processing artefacts.

On transforming images of the sort shown in plate 5.1(a), it was found that a form of raster effect was exhibited by the image collection system, (plate 5.2). The vertical band of intensity through the transform could only be described as a form of transfer function for the TV camera - data transfer hardware. Exactly how this may affect the information transferred however, is difficult to gauge and was not investigated further in this work.

The need to float images to a mean picture density of zero before transformation, as already explained in chapter 3, can be graphically illustrated by the formation of shape transforms from the picture edges, as shown in plate 5.3(a). The same image after suitable pre-treatment, yields a much more representative transform (plate 5.3(b)).

The effect of different reciprocal lattice window sizes can be seen in plate 5.4. The smaller the windows around each

Plate 5.2

The vertical band of intensity in the transform arising from the image collection system.

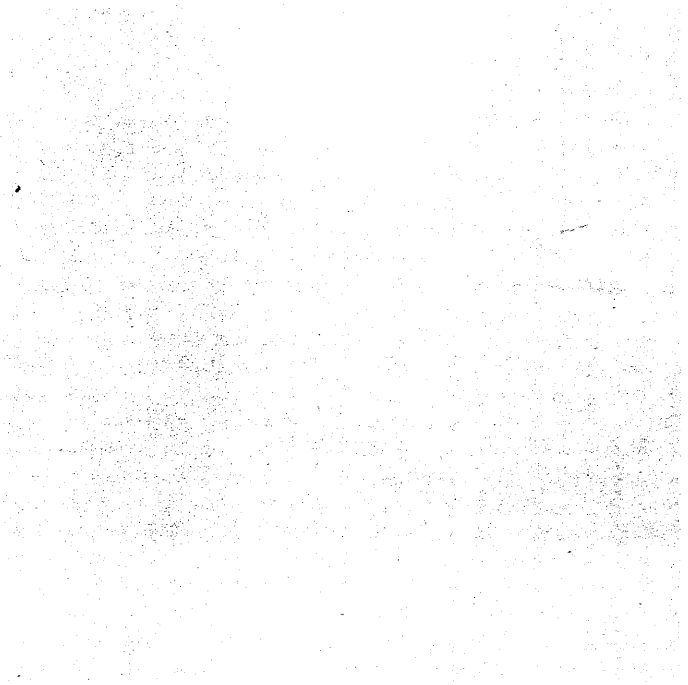

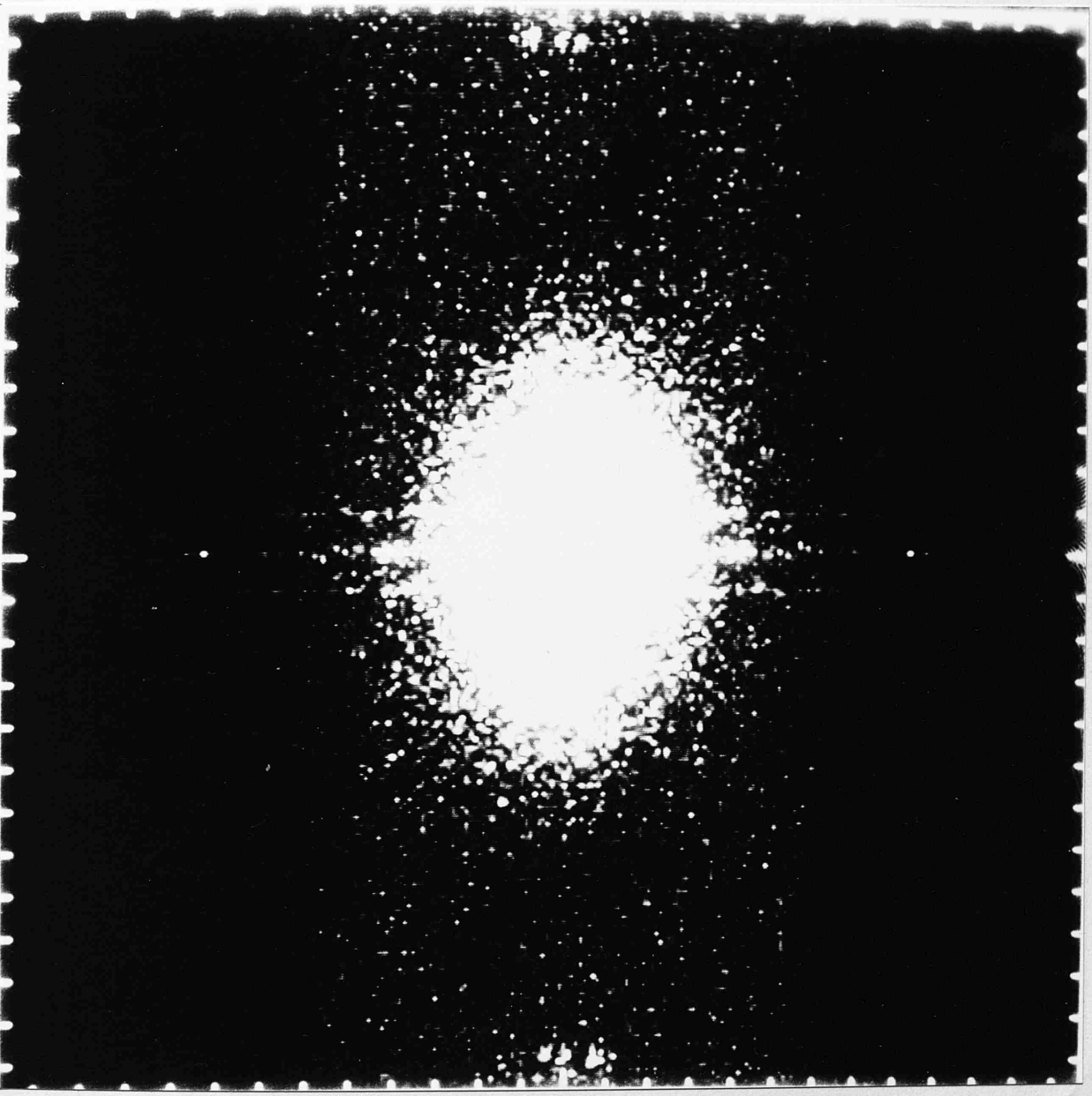

Plate 5.3

(a) Shape Transform

(b) Transform from 'pre-floated' image

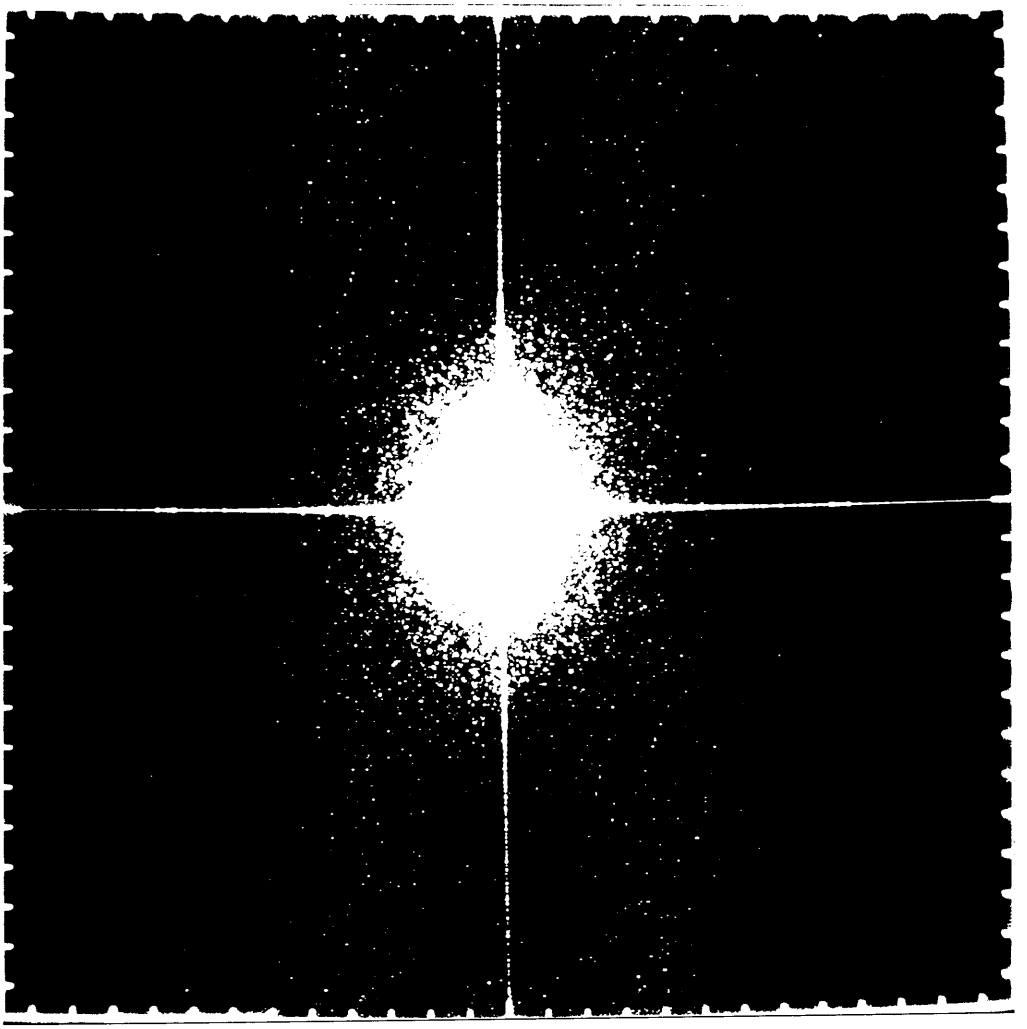

(a)

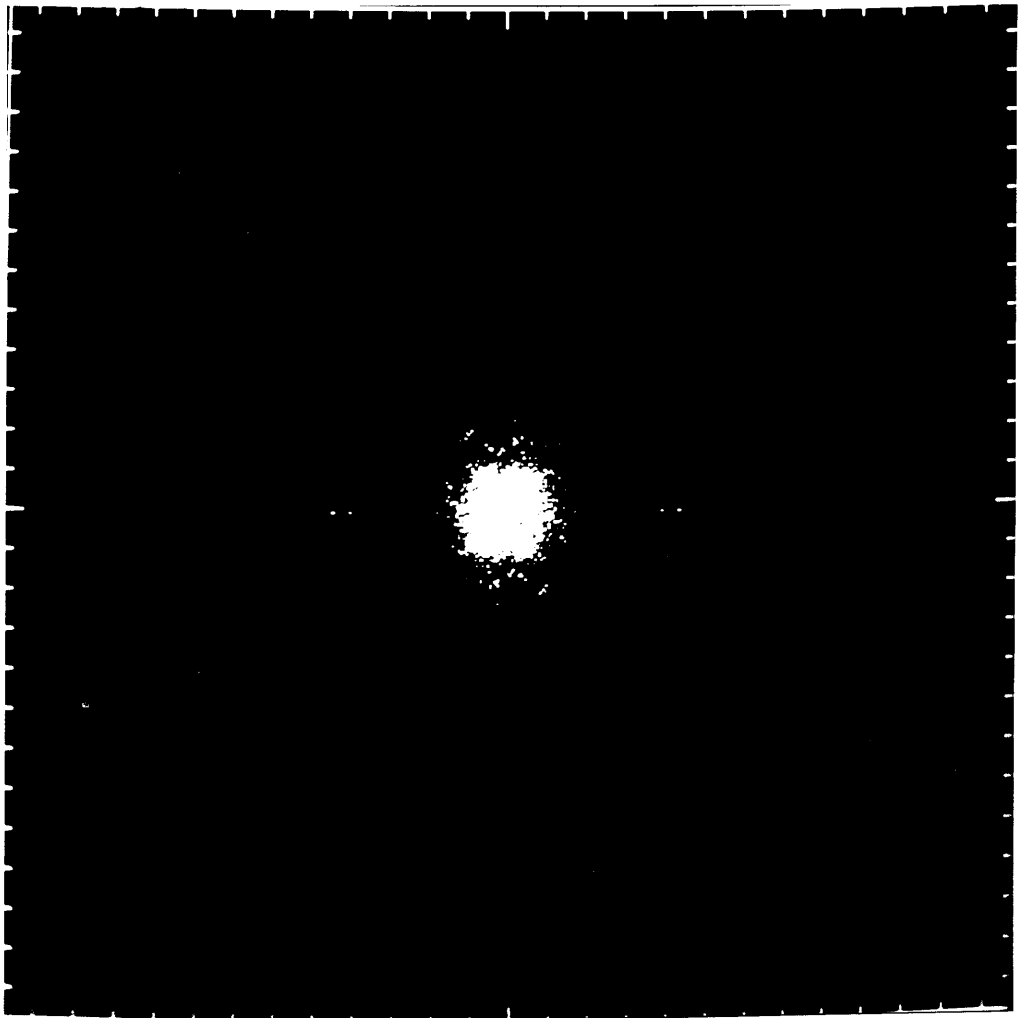

(b)

Plate 5.4

The effect of different reciprocal lattice 'window' sizes on the filtered result.

(a) 0.3 times the reciprocal lattice vector lengths.

(b) 0.2 times the reciprocal lattice vector lengths.

(c) 0.1 times the reciprocal lattice vector lengths.

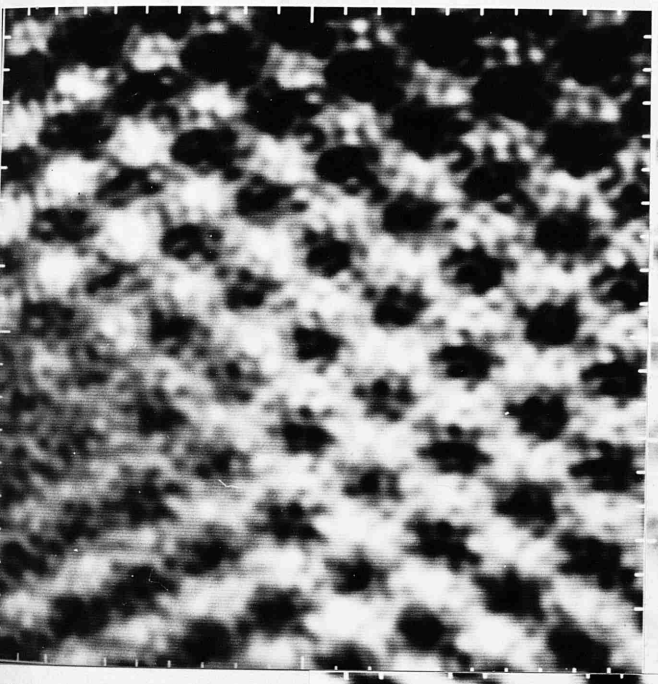

a

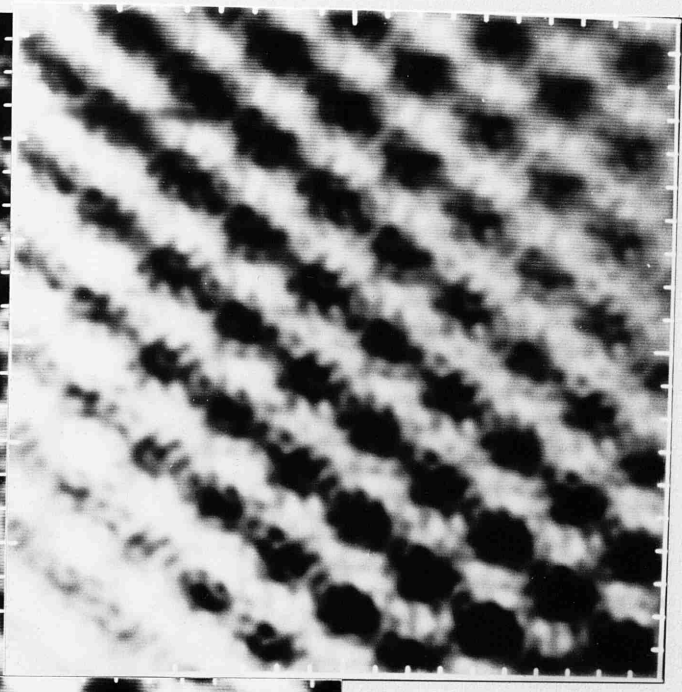

b

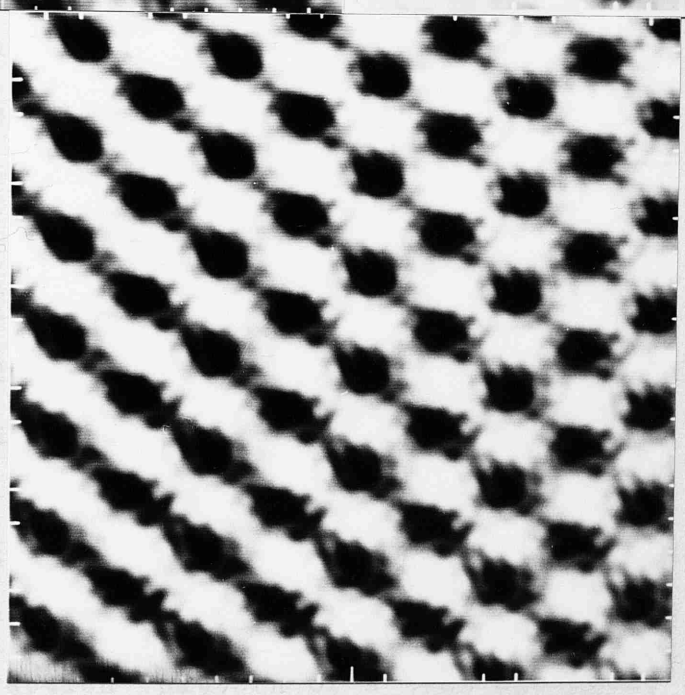

c

Plate 5.5

A rotationally symmetrised average image of a brominated phthalocyanine, produced using a 'correlation averaging' approach.

recorded by 'integrating' the signal received by the image intensifier camera over a number of frames, for example 1024, and 'stretching' the contrast as described in section 4.5.4. An example of such a pattern is shown in plate 5.6.

From the intensities of the diffraction maxima, the following comparison of the observed and calculated structure factors can be obtained.

hk	F(obs)	F(calc)
20	91.53	82.1
40	17.07	22.85
11	99.75	88.02
21	10.32	17.05
31	25.91	29.62
02	50.34	44.74
22	15.10	25.63

F(calc) - multislice calculation with isotropic B = 6.0Å^2 for all atoms.

The R- factor, a measure of how well the observed and calculated structure factors compare, for this data is R = 0.17, which is quite reasonable.

One point should be noted however. The Crystal system is equipped with a monochrome TV monitor so that a captured image may be assessed visually before input to MICRO-SEMPER Weak reflections in the paraffin diffraction pattern were

Plate 5.6

The (100) diffraction pattern of the paraffin $nC_{44}H_{90}$ recorded by the low light level TV camera.

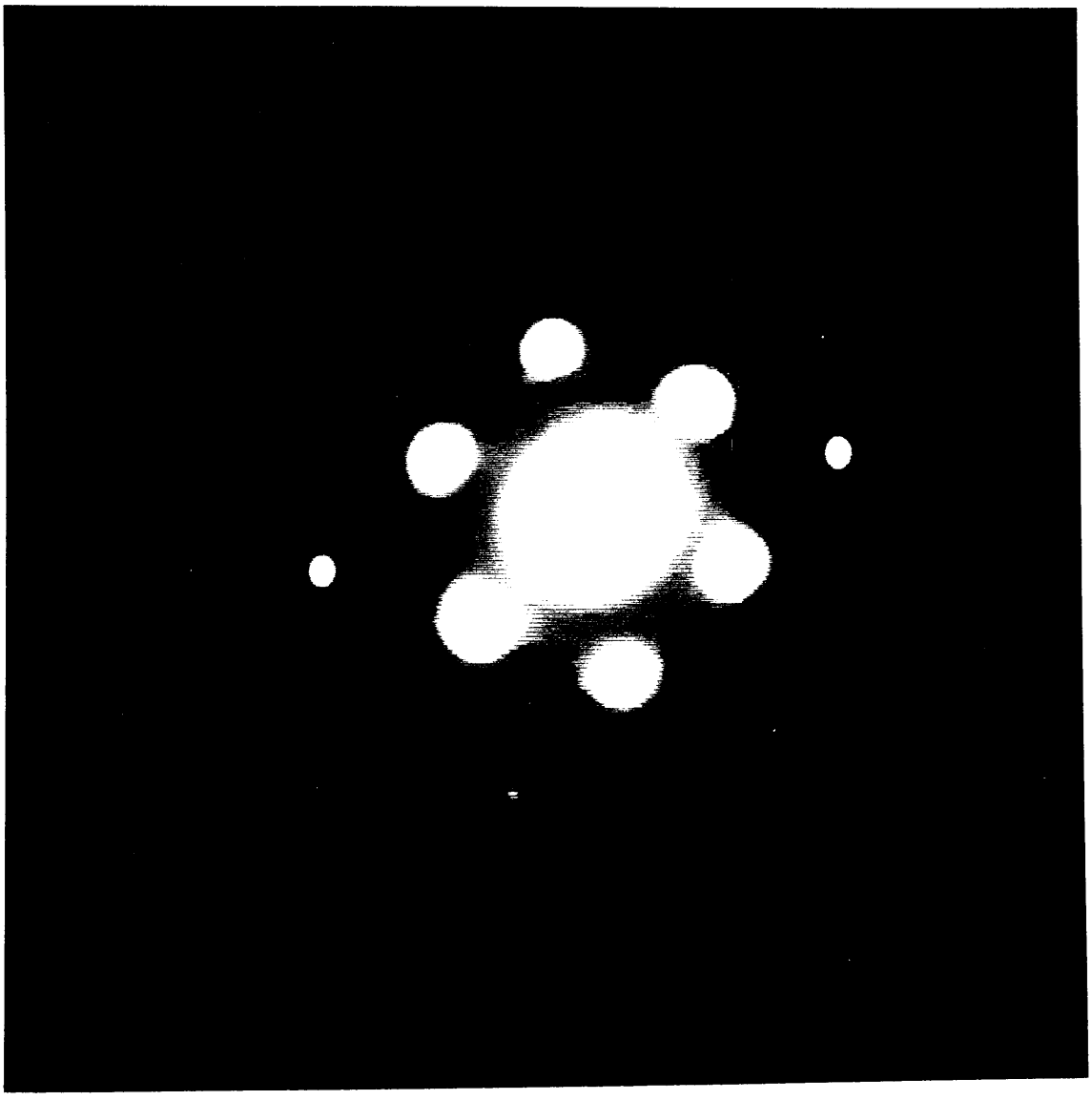

observed on this monitor which were not picked up by MICRO-SEMPER. This suggests that there must be a threshold level built into the system which may only be overcome by increasing the number of TV frames summed in recording the image. 'Stretching' the contrast of the image alleviated the problem to some extent without affecting the R- factor unduly. Further assessment, perhaps using a linear signal amplifier to boost the weak signals, is required. If, however, this data collection procedure proves valid then a considerable amount of photographic film could be saved and the time taken in measuring the intensities of diffraction spots shortened considerably.

5.2 Crystal Morphology of Calcium 4B Toner

Firstly, it should be pointed out that, whilst efforts were made to optimise crystallite dispersion in preparing the 4B specimens, crystal agglomeration was common and so most of the crystals examined were those that were separate from the main crystal masses. This may have resulted in the examination of atypical crystals however, this implied selectivity was minimised, as far as possible, by the use of the microscope in the diffraction mode when selecting areas for imaging. The small number of diffraction pattern types seen from the specimens (see section 5.5) allowed identification of suitable crystalline areas.

As can be seen in plate 5.7, lathe- or plate- like crystals were observed, often agglomerated to a large extent into

Plate 5.7

A typical example of crystal agglomeration in Ca4B toner samples.

Magnification:- X40,000.

masses. The wide variety of crystal lengths suggested that several components may be present, a situation not unusual in pigmentary materials as evidenced by the polymorphism of the phthalocyanines and azo pigments referred to in chapter 1.

Two components were of markedly different appearance, namely thin, flaky crystals and electron dense, dendritic masses. Closer examination of the electron dense masses showed a periodic lattice structure of 18Å (see plate 5.8). The apparent presence of these two components can be explained by the flat crystals being viewed 'side-on', so that strongly electron scattering layer planes are in the correct orientation to scatter electrons from the incident beam.

A further point evident from the 'side-on' views of the crystals is that there is exfoliation of the lattice planes at the ends of the crystals. This indicates a reduced lattice energy in these regions with the corresponding increase in capacity for crystal fusion, gas adsorption and such like.

Plates 5.9 and 5.10 show further examples of the crystal agglomerates with well-defined 18Å spacings present. The crystal marked in plate 5.10 shows an interesting lattice defect indicating a stacking fault.

An important point to note is the range of crystallite size. The crystal dimensions are, for the most part, less

Plate 5.8

Image of Ca4B toner showing an 18Å lattice spacing and exfoliation of the lattice planes at the end of the crystal.

Magnification:- X550,000.

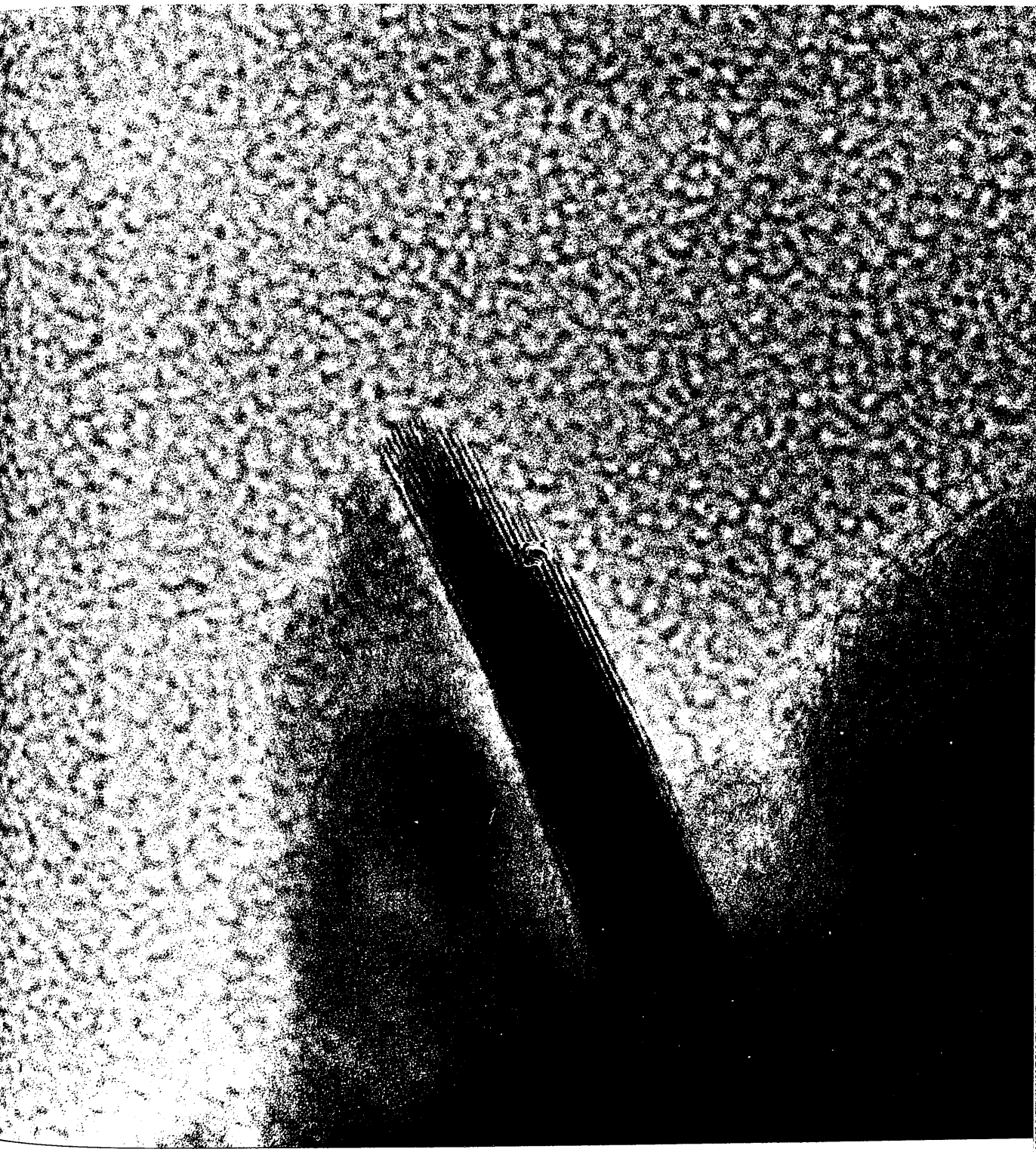

Plate 5.9

Image of an agglomerated crystal mass with 18Å periodicities clearly evident.

Magnification:- X470,000.

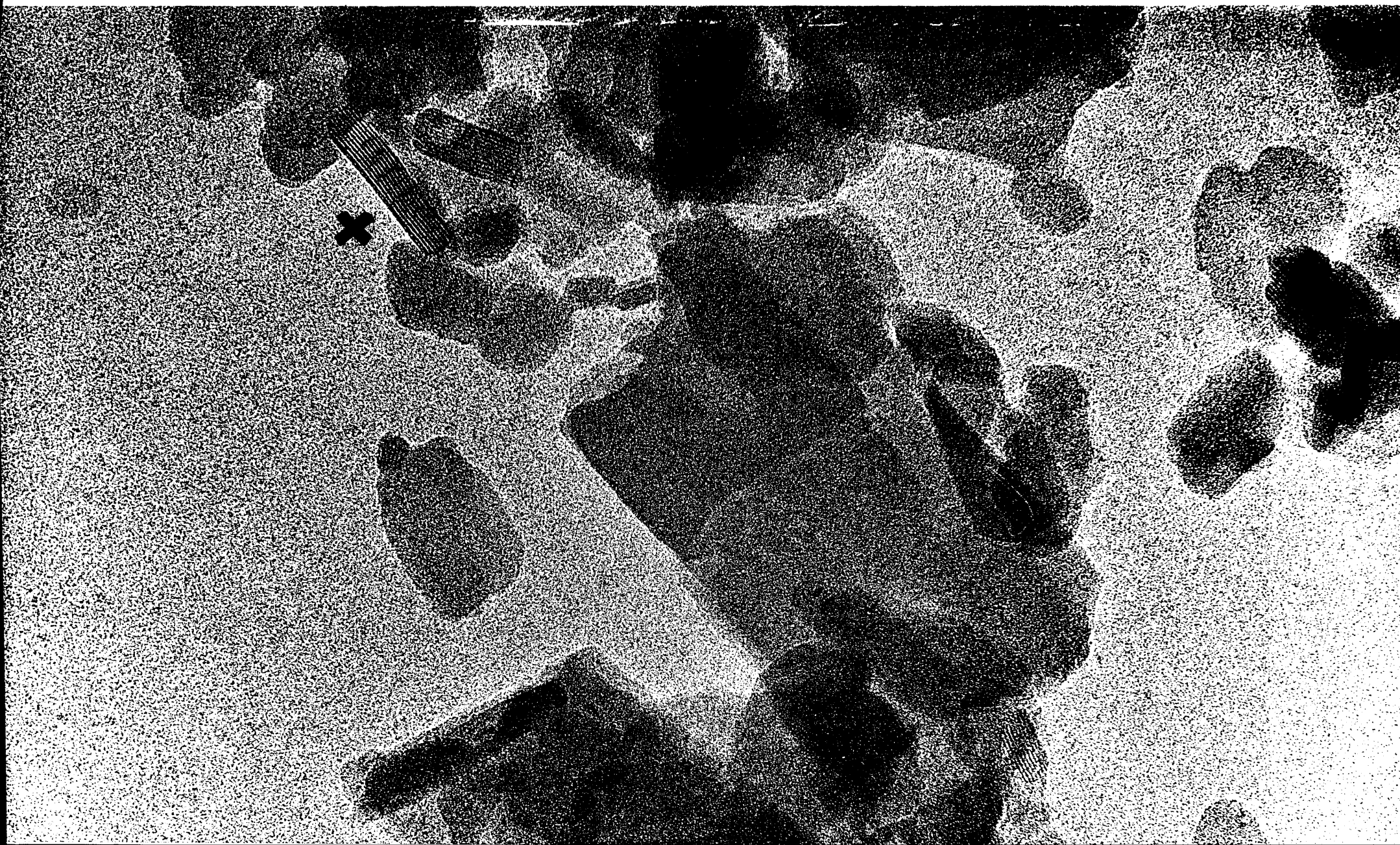

than 50nm in size, with larger crystals being encountered only occasionally. This, along with the radiation sensitivity of the crystals, has important consequences for high resolution electron microscope studies, as will be discussed shortly.

The anisotropic morphology of the crystals suggested, in common with other layer structures, that the organic anions are situated in the plane of the layers with the cations and water molecules situated between the layers, accounting for the ease of hydration.

Perhaps the most important feature to emerge from the preliminary survey of the crystals however, was their radiation sensitivity. The electron doses used in conventional electron microscopy caused rapid loss of high resolution detail, particularly from the in-layer structure, as evidenced by the fading of the diffraction pattern shown in plate 5.11. This problem necessitated the use of minimal and low dose imaging techniques in order to obtain high resolution information.

5.3 Minimal Dose Microscopy

The higher resolution, in-layer information could only be obtained using minimal dose microscopy; that is irradiating the crystals only when recording the image (see section 4.3). Plate 5.12 shows an image of a group of crystals with extensive areas of lattice fringes. An enlarged image of the boxed area is shown in plate 5.13 along with the

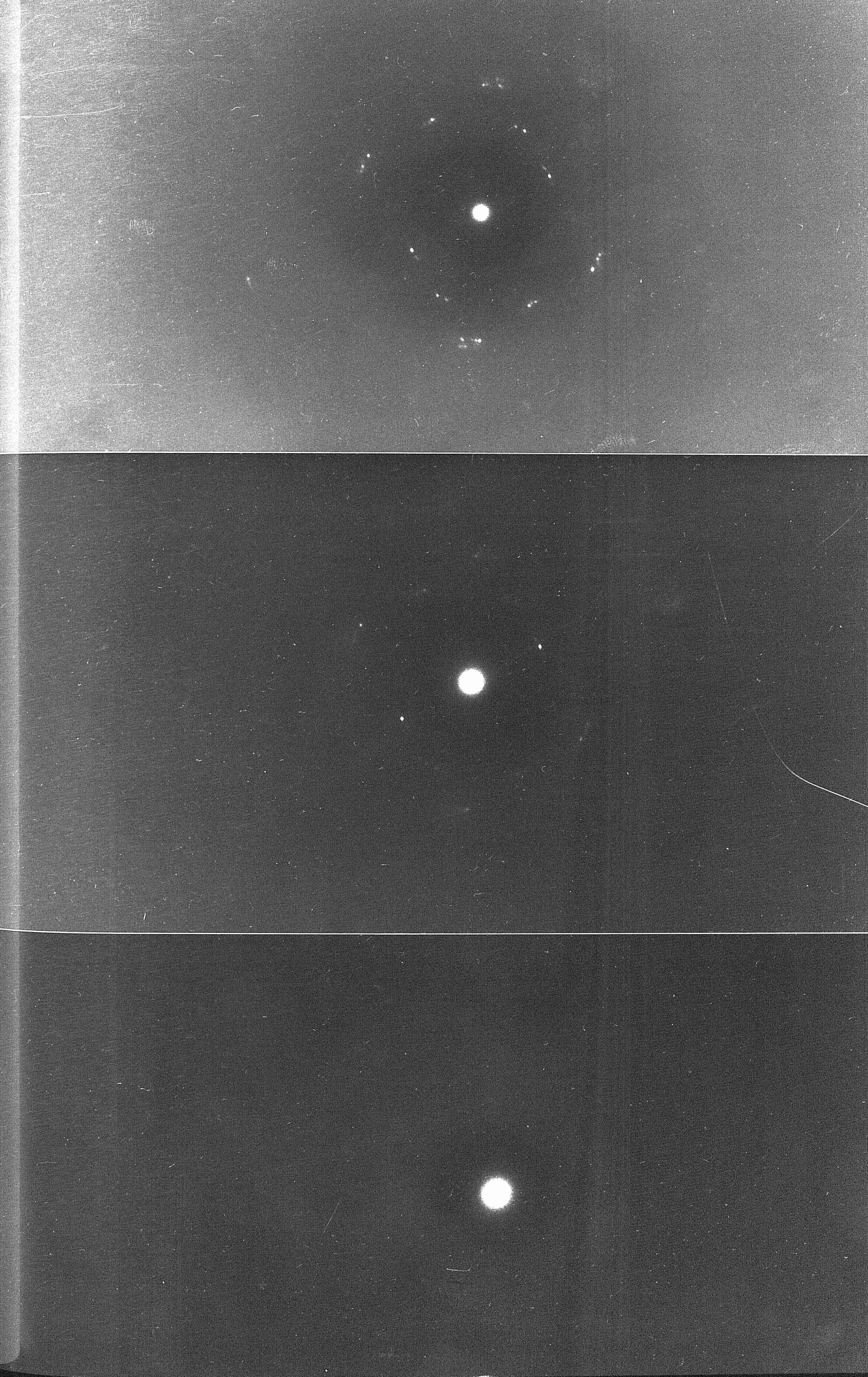

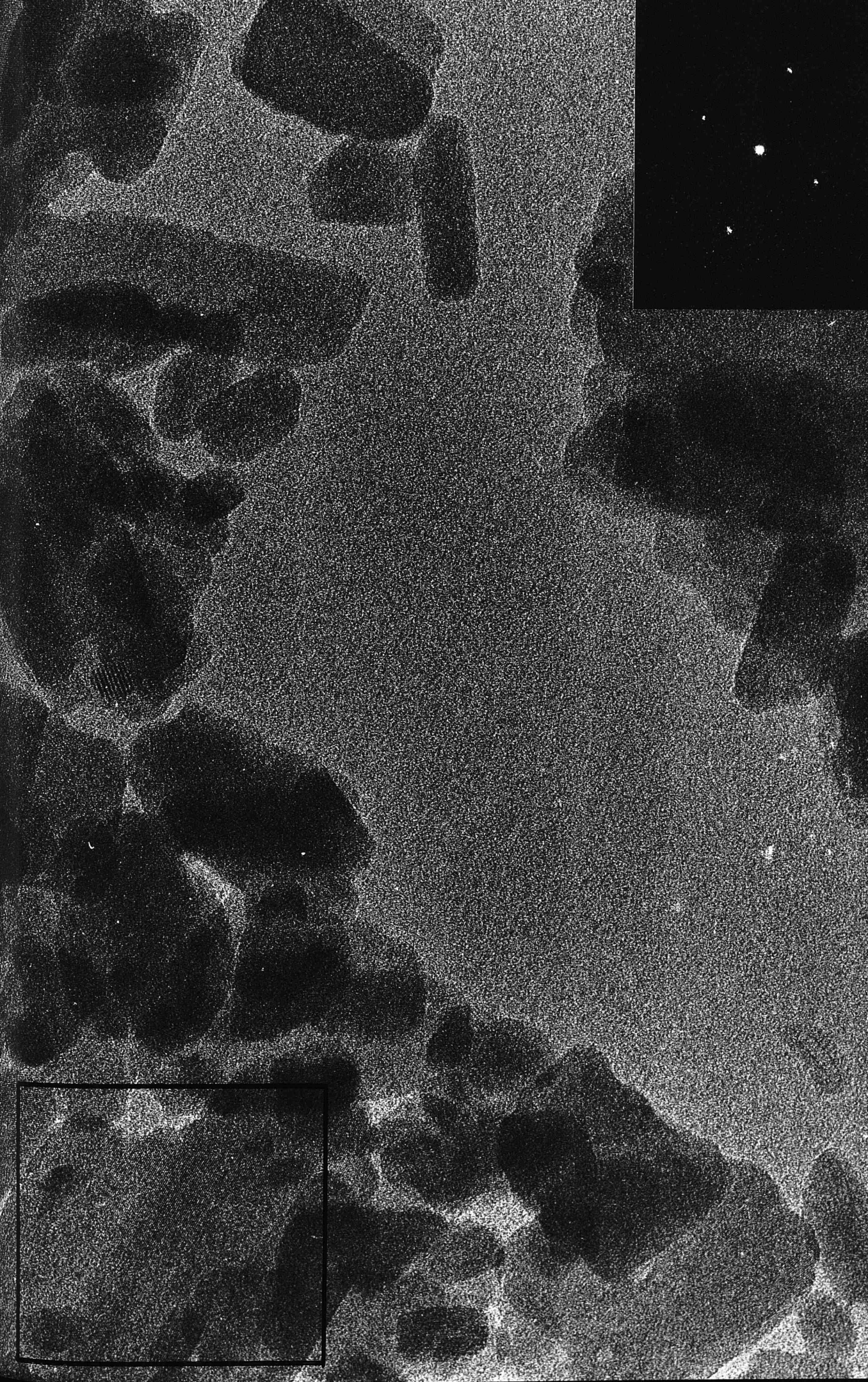

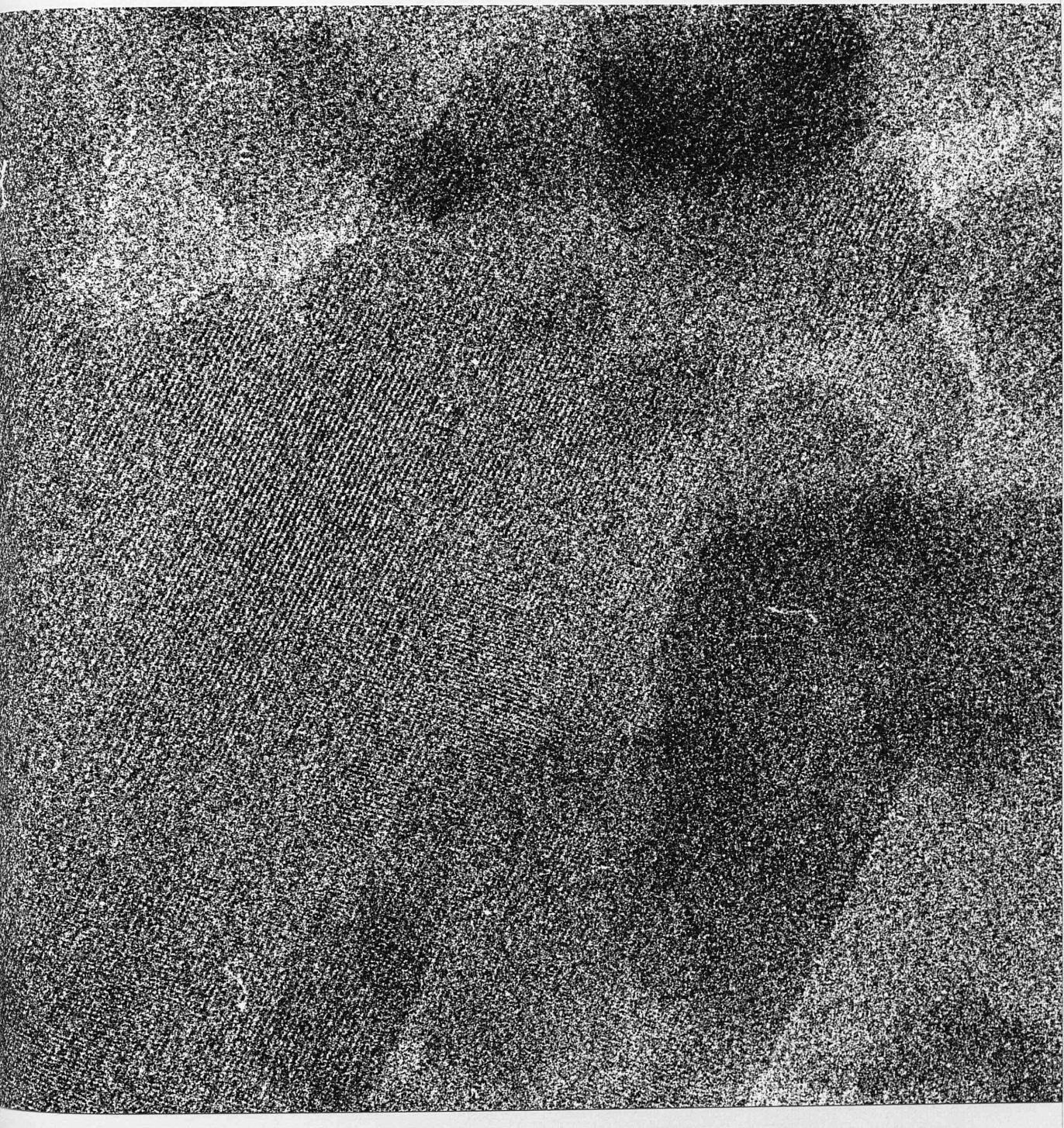

corresponding optical diffraction pattern of the area. Plates 5.14 and 5.15 show similar collections of crystals. It is interesting to note that the agglomeration of the crystals leads to a variety of crystal orientations with respect to the incident electron beam. As such, adjacent crystals can show quite different periodicities, as seen in plate 5.16. Without the possibility of preparing particular, crystalline orientations, for example the failure to produce vapour-deposited, epitaxial specimens due to thermal decomposition of the material, obtaining several images of a given orientation is somewhat uncertain, many images being required. Whilst some orientations may well be preferred, due to crystal/support interactions for example, the specimen preparation method used (spraying the crystal suspension onto the grids) could limit this effect, while drying droplets of the suspension on the grid is more likely to produce agglomeration.

Plate 5.17 shows an image of a crystal whose optical diffraction pattern shows structural preservation to 3.4Å.

Crystal agglomeration can cause considerable difficulties when using a minimal dose procedure. Often the crystal imaged is at a markedly different focus level than that set by focussing on an adjacent area. This limits the value of such images in any subsequent analysis and is another reason for the collection of many images, in order to obtain a few where the imaging conditions were as set.

Plates 5.14 and 5.15

Further examples of lattice fringes in Ca4B crystals. (5.4Å).

Magnification:- X530,000.

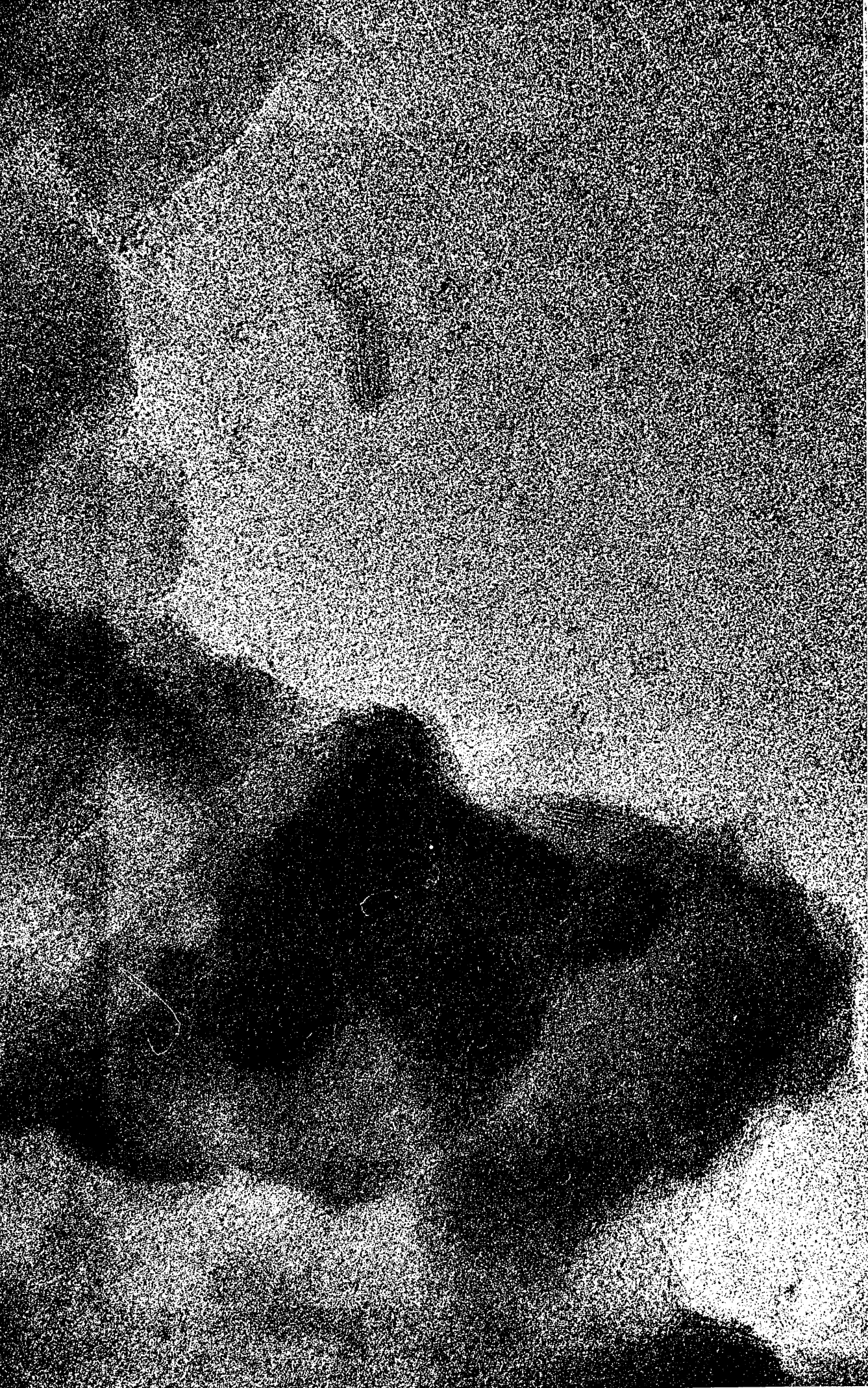

Plate 5.16

A group of Ca4B crystals, each showing differently spaced lattice fringes of 18Å, 7.2Å and 5.4Å.

Magnification:- X1,350,000.

Plate 5.17

Image of a Ca4B crystal showing structural preservation to 3.4Å. (Insert: optical diffraction pattern).

Magnification:- X630,000.

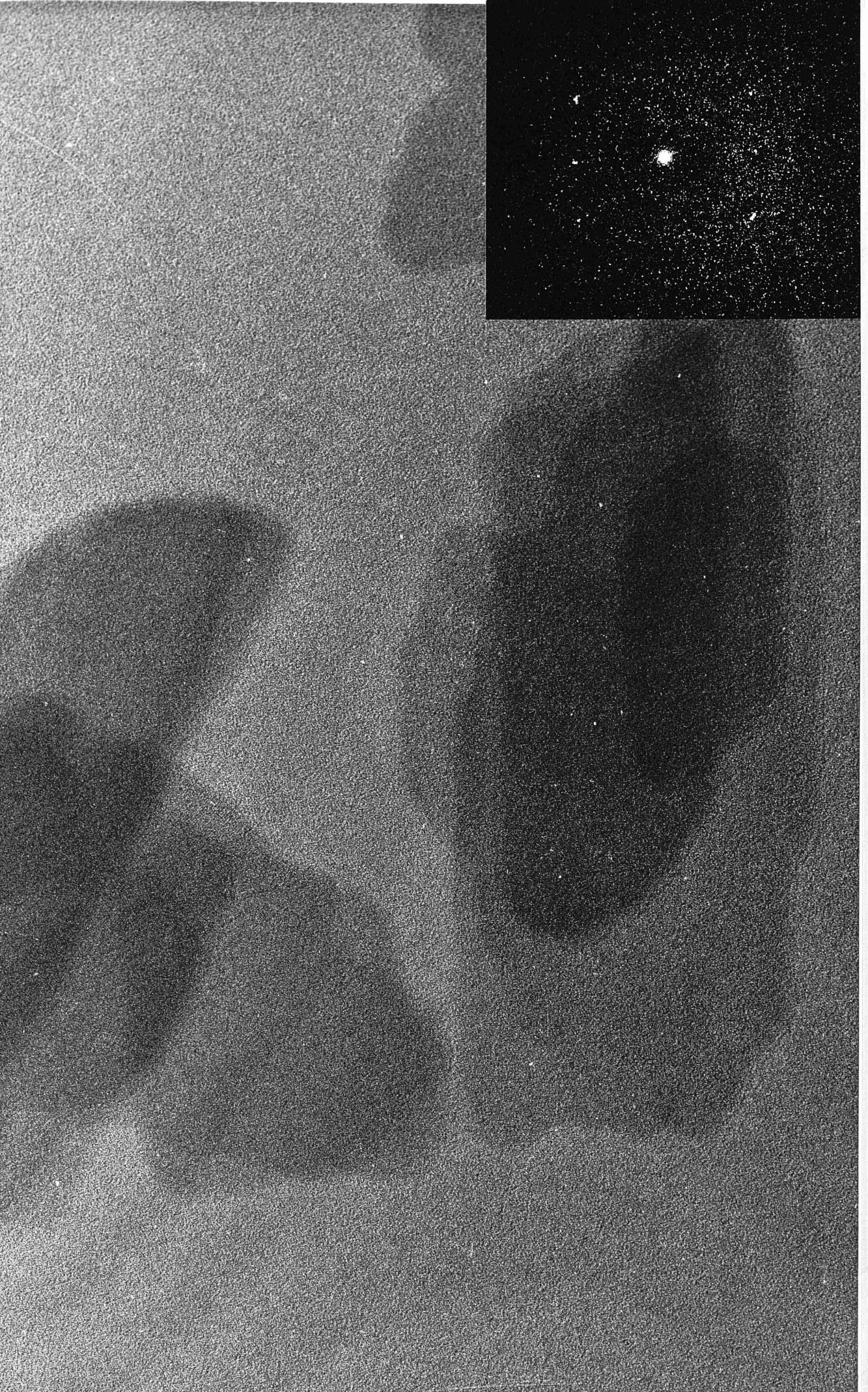

The radiation sensitivity of the crystals made obtaining focal series of statistically well-defined images of a given crystal impossible, as most of the high resolution detail was lost on obtaining the first image of the series. Consequently, low dose imaging had to be used with the resulting lack of statistical definition in the images. The results of applying computer image enhancement techniques on these images will be discussed more fully in section 5.6.

Despite the fact that the JEOL 1200EX electron microscope is equipped with a eucentric, tilting, specimen stage, the small size of the crystals presented difficulties in obtaining electron diffraction patterns or images at a range of tilt angles, as even a slight lateral movement of the crystal, moved it from the field of view defined by the selected area aperture. Furthermore, with no constancy of orientation between adjacent crystals, no correlation could be accurately defined without prior knowledge of the specimen structure. A specimen holder, as shown in figure 5.1, allowing a greater range of tilt angles than the $\pm 25°$ allowed by the existing specimen holder, proved of limited value due to difficulties in machining the holder to the correct specimen height and eucentricity.

5.4 X-Ray Powder Diffraction Results from Ca4B Toner.

X-ray powder diffraction patterns are used routinely as a qualitative analytical tool in the pigment industry. Listed in figure 5.2 are the interplanar spacings for the

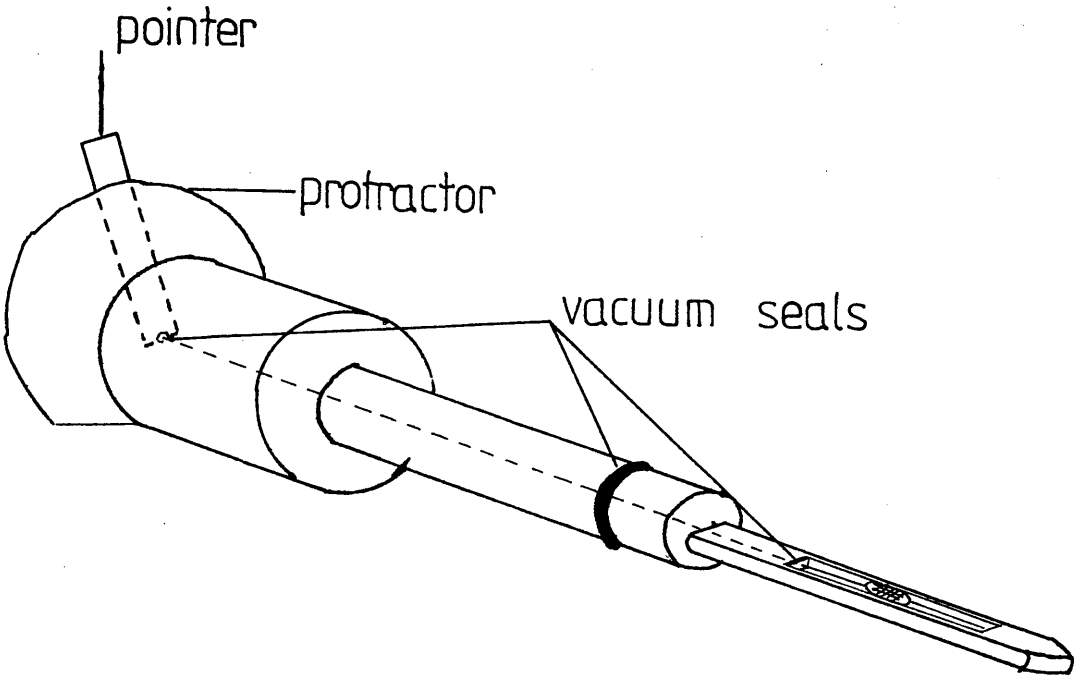

Figure 5.1

X-ray Powder Diffraction Spacings. (Å)

Monohydrate	Dihydrate
18.6	-
-	18.0
12.0	-
9.0	9.4
8.0	7.9
7.2	-
-	6.4
5.8	5.7
5.6	-
4.9	4.9
4.8	4.8
4.7	4.65
4.5	4.5
4.25	4.2
3.95	3.9
-	3.8
-	3.7
3.6	3.6
3.4	3.4
-	3.3
3.25	3.2
3.15	3.1
-	2.3

Figure 5.2

dihydrate and monohydrate pigment samples. As can be seen, the structures provide quite different patterns indicating a crystallographic change on the loss of the first mole of water (see section 1.3.4). The shade change seen on partial dehydration can therefore be ascribed to a definite structural alteration.

Indexing the monohydrate pattern, following the methods of Henry et. al.(1951) and Ito (1949), proved indecisive as using any probable combinations of reflections as the unit cell parameters failed to provide for all of the reflections in the pattern. Admittedly, neither method is completely reliable in producing indices for any given powder pattern, but the failure to index all the reflections can be interpreted as evidence of a degree of polymorphism in the sample.

5.5 Electron Diffraction of Ca4B Toner

As mentioned in chapter 1, Young (1971) pointed out that two discrete hydration states of the calcium 4B toner exist. Thermal gravimetry has shown that the dehydration of the compound progresses through both stages gradually, without a definite dissociation temperature being evident, thus suggesting that neither of the water molecules can be described as water of crystallisation. The first mole of water is removed between temperatures of 20 to 100°C, with the second between the much higher range of 150 to 250°C.

The x-ray powder diffraction results show that the monohydrate and dihydrate samples produce quite different diffraction patterns. The problem with examining these two structures in the electron microscope is that with the column vacuum at less than 10^{-6} torr, the dihydrate rapidly loses one mole of water at room temperature, and so identical diffraction patterns are obtained from both samples.

Electron diffraction patterns, both polycrystalline and single crystal, have been obtained of the monohydrate material. A polycrystalline pattern is shown in plate 5.18 and the interplanar spacings are tabulated in figure 5.3 along with the x-ray powder diffraction results for comparison. As can be seen, many of the spacings compare well from both techniques, although some are seen in the x-ray pattern which are not evident in the electron diffraction pattern. This is not surprising as, for example, the chance of a 'lathe-like' crystals on a microscope grid being oriented 'end-on' with respect to the incident beam is minimal, even in the polycrystalline pattern, resulting in some reflections not being seen in the electron diffraction case. The reasons for the differences in the results of the two diffraction methods are further compounded by the possibility of the polymorphism mentioned in the last section.

Single crystal patterns from the calcium 4B toner show only 3 types of pattern. These are shown in plates 5.19(a) to (c), with the interplanar spacings shown in these patterns

Diffraction Pattern Spacings (Å)

d(x-ray)	d(electron)
18.0	17.9
12.0	-
9.0	8.6
8.0	8.0
7.2	7.2
6.4	-
5.8	5.85
5.6	5.58
4.9	-
4.8	4.83
4.7	4.7
4.5	-
4.25	4.2
-	4.1
3.95	-
3.6	-
3.48	3.43
3.25	3.25
3.15	-

Smaller spacings obtained by electron diffraction include;

2.8, 2.7, 2.6, 2.4, 2.0, 1.95, 1.87, 1.8, 1.7, 1.6, 1.45, 1.36, 1.16.

Figure 5.3

Plate 5.18

Polycrystalline electron diffraction pattern of Ca4B toner.

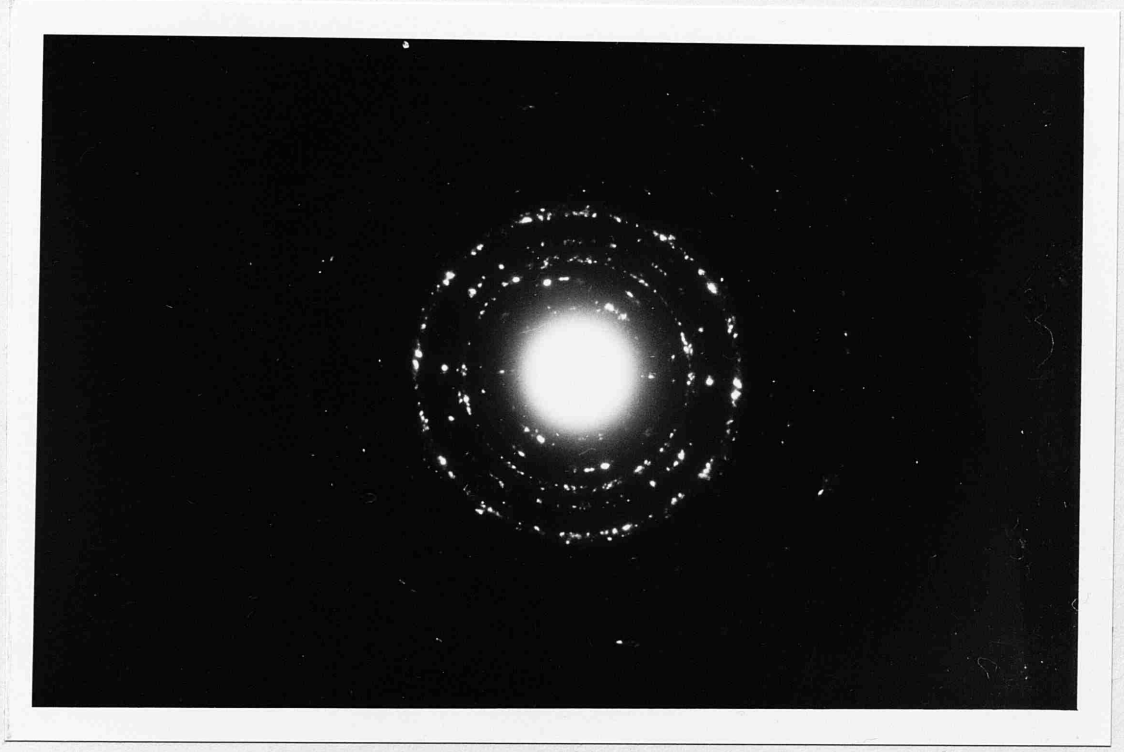

Plate 5.19

Characteristic, single crystal, electron diffraction patterns of Ca4B toner.

a

b

c

listed in figure 5.4(a) to (c). The limited number of diffraction patterns serve as further evidence of the layer structure of the crystals, since such materials commonly have only a few zone axes which orient a suitable number of crystal planes to give discrete arrays of diffraction spots.

Patterns of the sort shown in plate 5.19(b) were indexed, tentatively, as shown in figure 5.5. From this and the orientation showing the 18A periodicity, unit cell parameters have been assigned as follows;

Monoclinic $a = 8.4\text{Å}$ $b = 5.8\text{Å}$ $c = 18\text{Å}$ $\beta = 92°$

Using these unit cell parameters, indexing of the x-ray powder diffraction patterns again proved to be unsuccessful

Density measurements of the crystals of $1.66 g/cm^3$ compared favourably with the expected value for two formula units of the monohydrate material per unit cell.

5.6 Results of Computer Processing of Images of Ca4B Toner Crystals.

As shown in section 5.1.1, the improvement in the visibility of the molecular columns in images of copper phthalocyanines, by computer image processing techniques, led to such an approach being applied to low dose images of the Ca4B crystals.

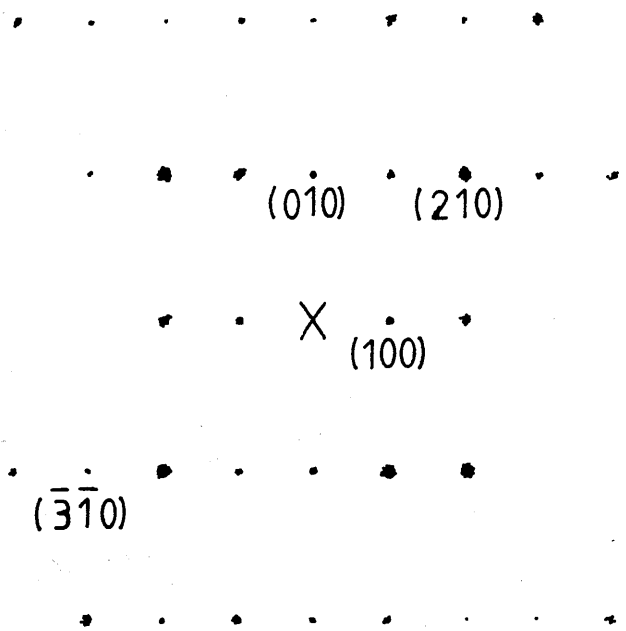

Figure 5.5

The optical transform from an area of such an image is shown in plate 5.20, along with the original digitised image, an enlarged area of the resulting filtered image and the calculated power spectrum.

When examined more closely, the 'Y' - shaped motifs in the filtered image suggested that these were molecular images, the proposed molecular arrangement being that shown in plate 5.21. Similar examples of such filtered images can be seen in plates 5.22 and 5.23.

Some justification for such an interpretation can be found in O'Keefe, Fryer and Smith (1983), who demonstrated, by using calculated images, that resolution of aromatic rings in images of organic materials, to give recognisable molecular shapes, was possible even up to a microscope resolution of around 7Å. The optical diffraction patterns of the 4B images used in the computer processing methods here showed the image resolution to be between 3 to 4Å.

The implications of this interpretation in the light of the electron diffraction results and the evidence, already detailed in section 1.3.3, on the structures of similar materials, form the subject of the next section.

5.7 A Possible Structure of Calcium 4B Toner

Considering further the packing variations shown by azo compounds discussed in section 1.3.3, some possible packing arrangements of the calcium 4B molecules may be proposed,

Plate 5.20

Optical transform (top left) from original low-dose image of a Ca4B crystal. The filtered transform is shown (top right) along with an enlarged area of the filtered image.

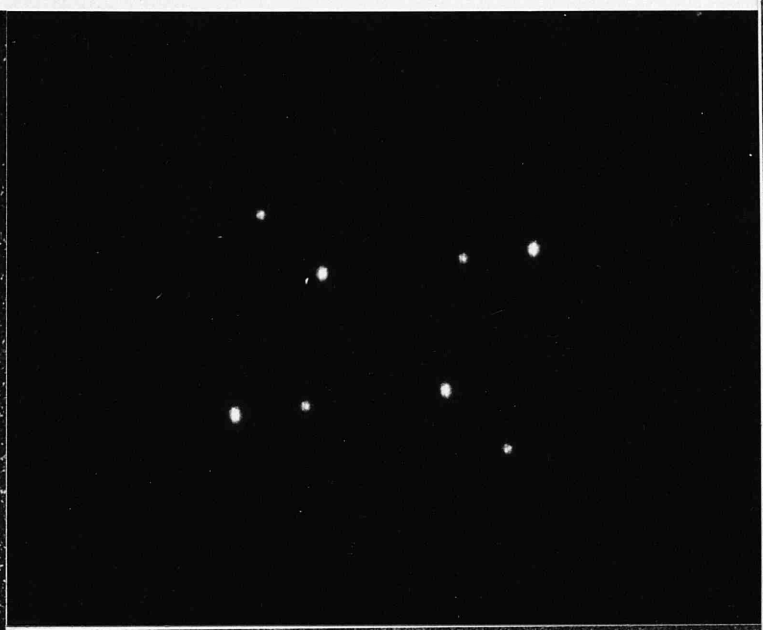

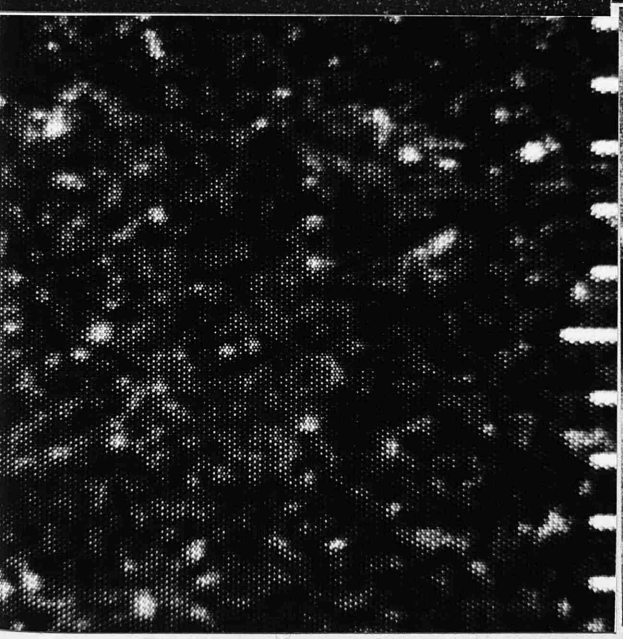

Plate 5.21

Proposed molecular arrangement in crystals of Ca4B toner.

Me
N
N
H
O
$^{-}O_3S$
Ca^{2+}
CO_2^-
$^{-}O_2C$
Ca^{2+}
SO_3^-
O
H
N
N
Me

Plates 5.22 and 5.23

Other examples of 'molecular' images of Ca4B toner molecules.

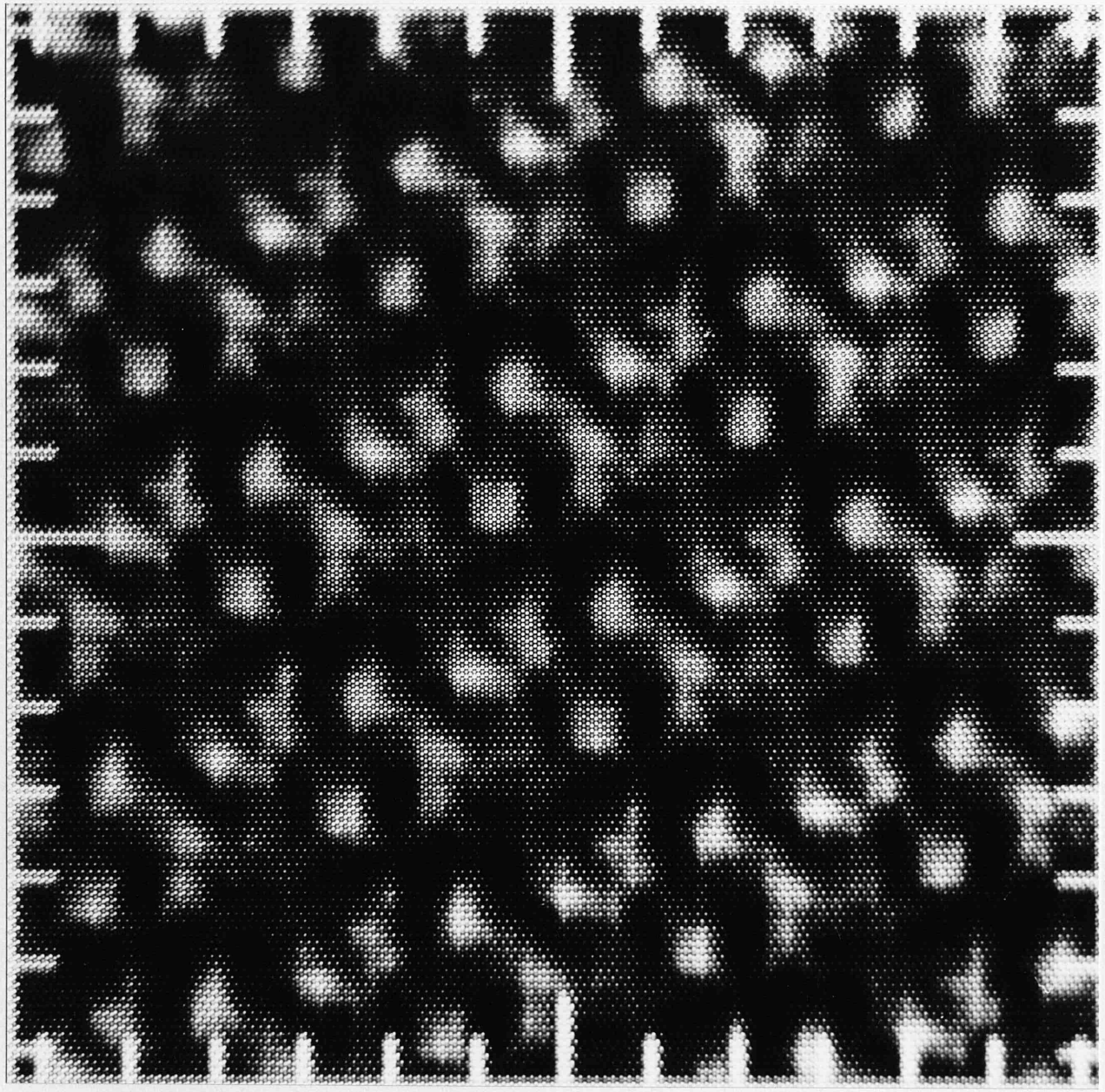

bearing in mind the fact that the structures so far determined are of purely organic pigments and not of a metal salt.

Firstly, considering the 4B molecule itself, a large body of evidence, from the lack of hydroxylic properties to C n.m.r. studies (Harris et. al. (1984)), suggests that the molecules exist as the keto-hydrazone tautomer (see figure 1.7(II)). This is not an uncommon phenomenon for many azo compounds as shown, for naphthol and naphthylamine derivatives for example, by Kelemen (1981) and Kelemen et al (1982 a,b) using Raman, n.m.r., electronic and mass spectroscopy and supported by molecular orbital theory Kelemen et al (1982c). The 4B molecule may then be assumed to exist in the form shown in figure 5.6. As such the possibility of cis and trans conformations and intramolecular hydrogen bonding become important factors. As discussed in section 1.3.3 all of the azo pigments for which crystal structure determinations have been carried out, show the trans conformation (see figure 1.8). The 4B molecule contains a sulphonate group, ortho to the hydrazo link and therefore a bifurcated hydrogen bond is likely involving the naphthol oxygen, the hydrazo hydrogen and one of the sulphonate oxygens. Following the reasoning given earlier therefore, the molecule is likely to be planar; the bifurcated hydrogen bond constraining both ring systems to the same plane. The organic anions then should show similar packing arrangements to those exhibited by the metal free pigments already mentioned.

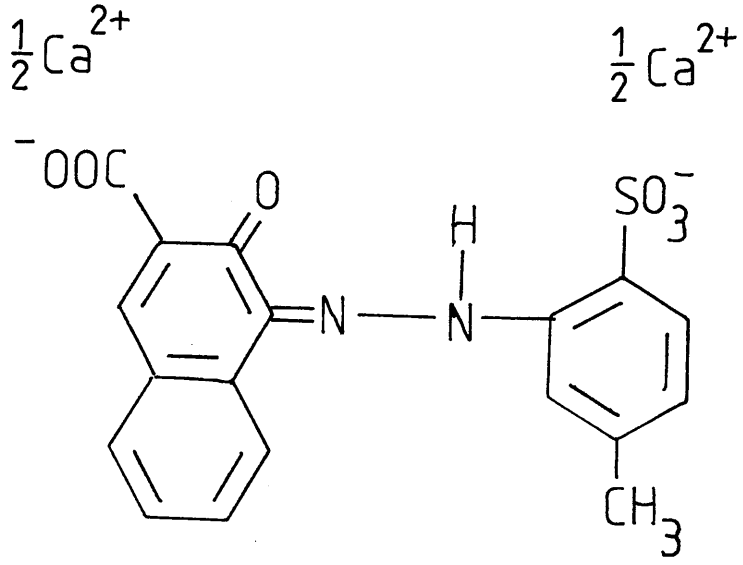

Figure 5·6

Whitaker (1978b) has described the crystal morphology of the azo pigments as flat, needle-shaped crystals. The planar azo molecules stack in columns within the crystal, with the columnar axis parallel to the needle axis. Within the columns, the molecular planes are not perpendicular to the column axis, in all cases. It would seem reasonable then to assume that a similar situation exists in the case of the Ca4B anions. Johnson (1984), using solid state n.m.r. spectroscopy of the cadmium analogue of the Ca4B toner, has shown that only one metal ion environment exists in the material, suggesting a 'head-to-tail' arrangement of the pigment molecules. Figure 5.7 shows two possible intermolecular arrangements consistent with this finding.

The significance of the interpretation of the processed images shown in the last section should now be apparent. The dimeric units visible in images such as those shown in plates 5.20 to 5.23 closely conforms to the arrangement drawn in figure 5.7(b).

An immediate consequence of this interpretation is that the molecular planes are tilted well away from being normal to the columnar axis in the crystal.

Clearly the most important contribution to the intermolecular bonding in the dimer will arise from the electrostatic bonding between the organic anions and the calcium cations. Calcium ions are generally found in 4- or 6- coordinate environments. It is possible to envisage situations where both coordination possibilities can be

(a)

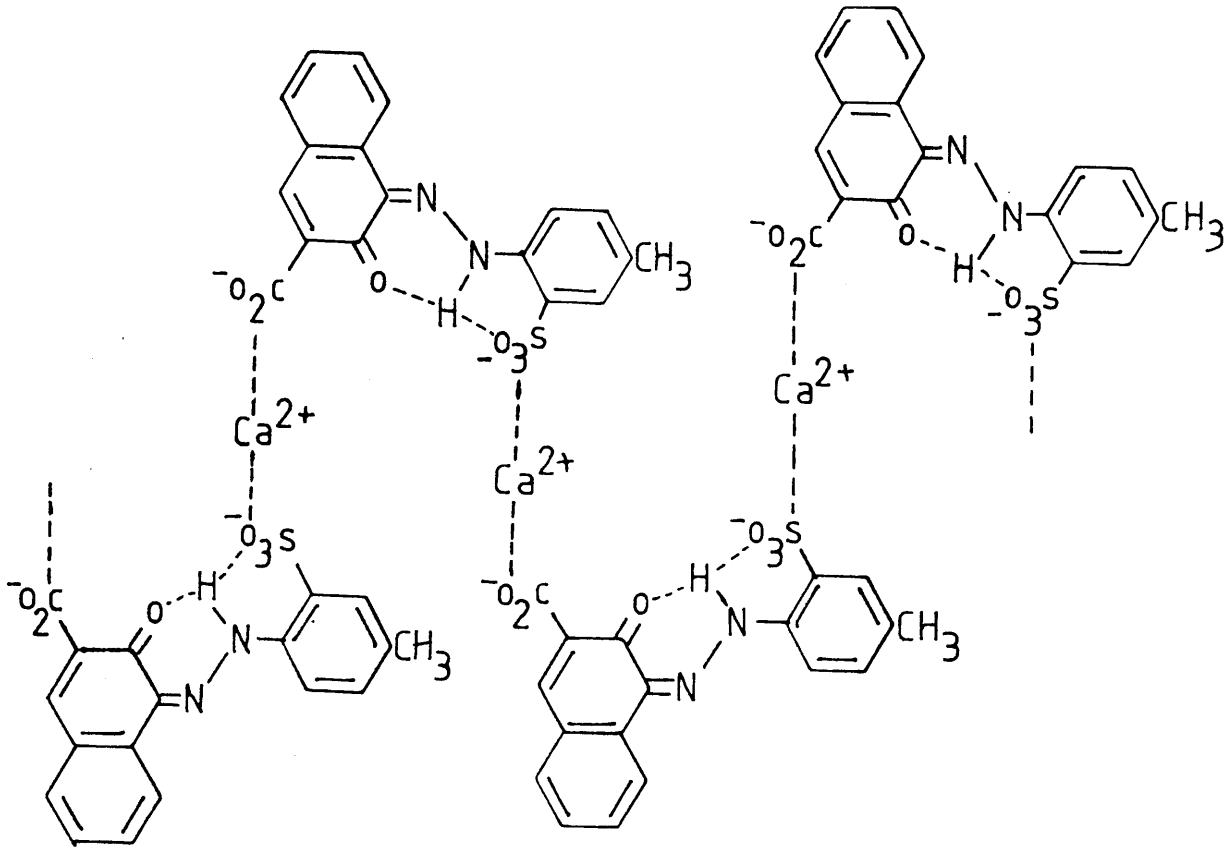

(b)

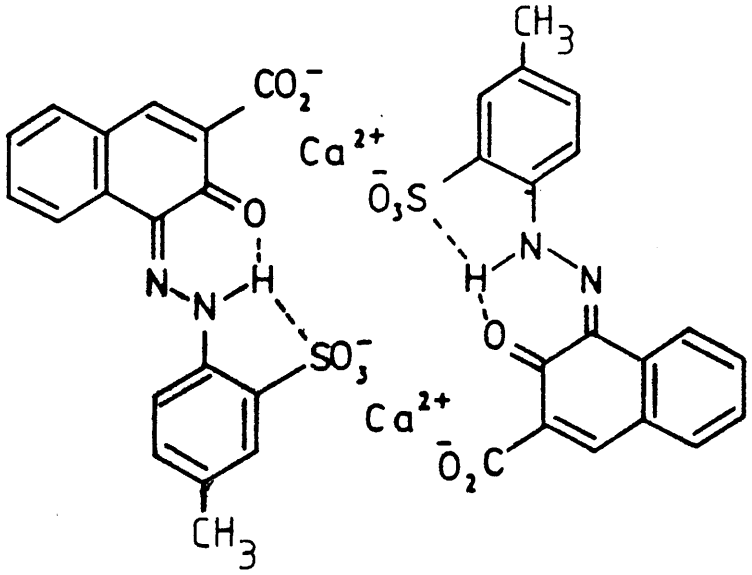

Figure 5.7

accomodated in the 4B crystals as shown in figure 5.8. Without a full crystal structure determination however, it is difficult to distinguish between these possibilities. It can be suggested, admittedly without any solid evidence however, that the shade change on the loss of one molecule of water may be linked to the different coordination possibilities for the calcium ions.

The in-layer packing of the organic anions has been investigated by building models of the possible combinations. The two arrangements shown in figure 5.7 give rise to packing arrangements of the sort shown in figure 5.9 (a) and (b). In the light of the molecular images presented in the last section then, it is proposed that the packing arrangement resembles that shown in figure 5.9(b).

One implication of this assignment is that, if the prediction of an organic layer structure, with the interlayer spacing equal to the c axis distance (18Å), is correct then there is a very large space between the layers of molecules, perhaps explaining the ease of hydration.

The small crystallite size may also be viewed as a direct consequence of the large interlayer spacing. The layers cannot be considered to be 'close-packed' and as such the crystals' internal energy is not minimized as demanded by the theory of close packing of organic molecules. A situation may be envisaged where the crystal becomes meta-stable on reaching a certain size, with the result that

(a)

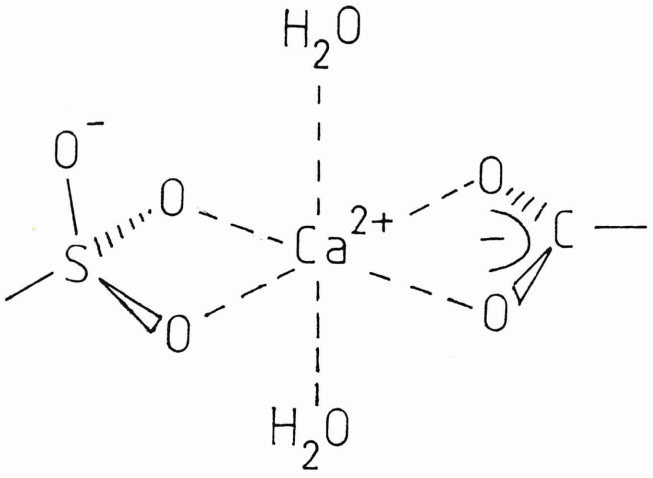

(b)

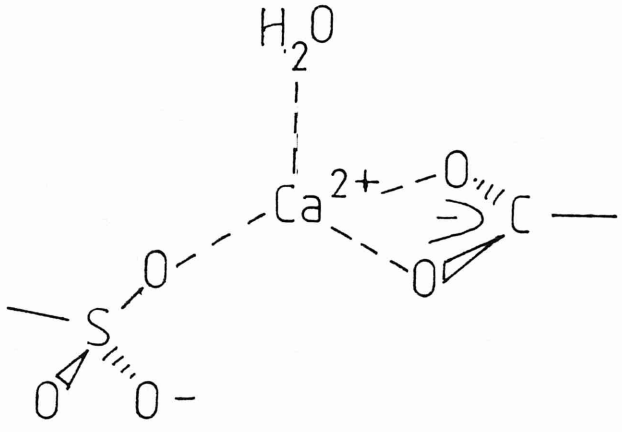

Figure 5.8

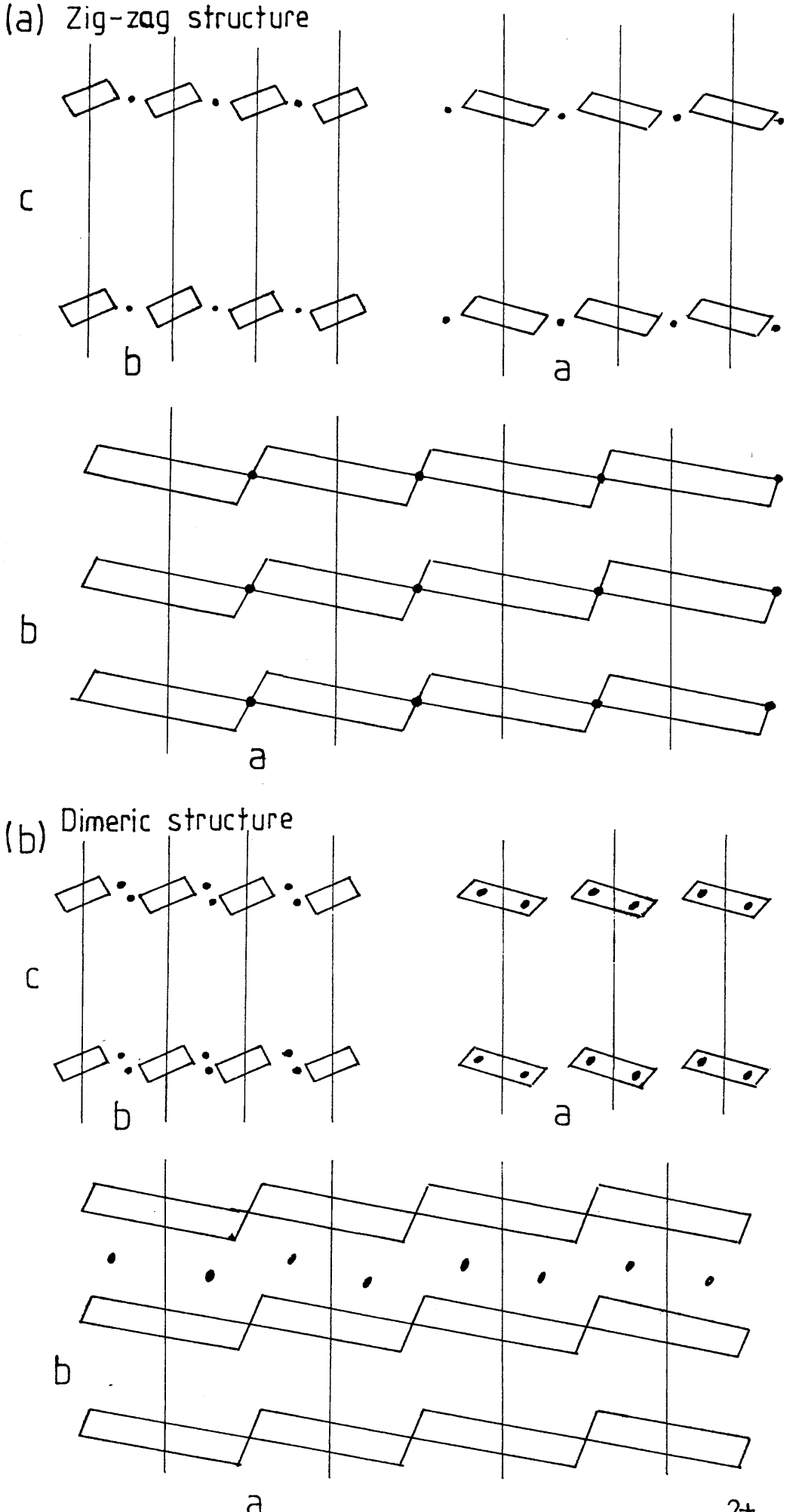
(a) Zig-zag structure
c
b
a
b
a
(b) Dimeric structure
c
b
a
b
a
Ca^{2+}
4B acid

Figure 5.9

further crystal growth is not possible. The failure to achieve a close-packed arrangement of the layers can only be ascribed to the presence of the calcium ions in the crystal, making the crystal more ionic in nature and so in some way hindering the packing of the organic anions.

5.8 CONCLUSIONS

The results of the approach used in this work for the structural investigation of an organic material, which cannot be studied by conventional x-ray techniques, give reason for some optimism about the future of such studies. Whilst there can be no doubt that, at present, the procedure is ad hoc in nature, the commercial significance of developing a method for determining the structure of organic pigments and indeed any organic material which forms only small crystals, is obvious and certainly provides an impetus for the continuation of the work. Reviewing the results presented in this thesis, the following points are apparent.

Calcium 4B Toner

1/ The 4B toner exists as a dimeric structure with the dimers arranged in layers.

2/ The large interlayer separation would appear to account for the ease of hydration of the material. Indeed, some

very recent work has suggested that other ions (for example silicate ions) can diffuse easily into this gap.

3/ The commercial pigment, in common with many others, probably exists as a mixture of polymorphs, the details of which are not yet known.

4/ The shade change evident in the production of the pigment is associated with a definite structural alteration and may be due to different coordination environments of the calcium ions in the two forms of the pigment.

Image Processing

1/ With the limitations imposed on resolution by the radiation sensitivity of organic crystals, image processing techniques provide an avenue by which the internal structure of such materials may be investigated.

2/ The establishment of an on-line, or at least dedicated, processing system provides many advantages to the use of a more powerful, but time-sharing, off-line system (unless, of course, the CPU time is being shared between very few processes).

5.9 Suggestions for Further Work

1/ Recently, it has been pointed out that incident beam tilt can have a profound effect on the images obtained in an electron microscope, particularly at high resolution (Henderson et al (1986)). In the light of this observation, closer examination of the beam alignment procedures used must be carried out. In this respect, a fast, on-line computer system, to allow real time computation of image covariance (to visualise the effect of slight beam misalignment), would be extremely useful. (Saxton - private communication).

2/ A more intensive electron diffraction study, at a greater range of tilt angles and using samples prepared in a manner specifically designed to limit the possiblity of polymorphism, should be carried out on the Ca4B toner.

3/ Cryo-microscopy may be used to prolong the lifetimes of the specimens allowing higher resolution images to be obtained. The low temperatures may, in addition, allow the study of the dihydrate form of the pigment, in the microscope.

4/ Development of the 'short-exposure' technique could yield significant improvement on the acquisition of structural information from radiation sensitive specimens. The initial study mentioned here and further work by Fryer (1987) indicates that the technique shows great promise.

REFERENCES

Aebi, U., Smith, P.R., Dubochet, J., Henry, C. and Kellenberger, E. (1973), Jou. Supramol. Struct., 1, 498 - 522.

Allen (1971) In 'Colour Chemistry', Nelson, P.23.

Andrews K.W. Dyson D. J. Keown S. R. (1967). In 'Electron Diffraction Pattterns' Adam Hilger London.

Ashida (1966a) Bull Chem. Soc. Japan. 39, 2625.

Ashida (1966b) Bull Chem. Soc. Japan. 39, 2632.

Bamberger (1894) Ber 27, 1948.

Beeston B.E.P. Horne R.W. and Markham R. (1972). In 'Practical Methods in Electron Microscopy' ED G.M. Glauert, North Holland Amsterdam.

Boerchia A. and Bonhomme P. (1974). Optik, 39, 437.

Brown C. J. (1968) Jou. Chem. Soc. (A) 2488 - 2493, 2494 - 2498.

Busch H. (1926) Ann Physik, 81, 974.

Busch H. (1927) Arch Elektrotech. 18, 583.

Cosslett V. E. (1980) Proc. R. Soc. London. A 370, 1.

Cowley J. M. and Moodie A. F. (1957). Acta Cryst 10, 609.

Cowley J. M. and Moodie A. F. (1959). Acta Cryst 12.

Cowley J. M. (1961). Acta Cryst 14, 920.

Cowley J. M. (1975). In 'Diffraction Physics.', North Holland, Amsterdam. Oxford. New York.

Davisson and Germer (1927). Phys. Rev., 30, 705 - 740.

De Broglie (1924). Phil Mag 47, 446 - 458.

Dorset D. L. (1978). Z. Naturforsch, 33a, 964.

Dorset D. L. (1980). Acta. Cryst. A36, 592.

Dorset D. L. (1983). Ultramic 12, 19.

Dorset D. L. (1985). Jou. Electron Microsc. Tech. 2, 89 - 128.

Dubochet J. Knapek E. and Dietrich I. (1981) Ultramic 6, 77 - 80.

Eisenhandler C. B. and Siegal B. M. (1966) Jou Appl. Phys. 37, 1963.

Erickson and Klug (1971), Phil. Trans. Roy. Soc. London B261, 105 - 118.

Fejes P. L. (1977). Acta Cryst A33, 109.

Frank J. (1973). Optik 38, 519.

Frank J. (1974). Optik 43, 25.

Friedlander G and Kennedy J. W. (1962). In 'Nuclear and Radiochemistry', Wiley, New York, 214.

Fryer J. R. (1977) Inst Phys Con Ser 36, Emag Glasgow 423.

Fryer J. R. (1978) 9th Int. Cong E. M. Toronto 1, 256.

Fryer J. R. (1979) E.M.S.A., San Antonio, pp 552.

Fryer J. R. and Holland F. (1983). Ultramic 11, 67 - 70.

Fryer J. R. and Holland F. (1984). Proc. Roy. Soc. London. A393, 353 - 369.

Fryer J. R. and Smith D. J. (1984). Jou of Micros 141,3-9.

Fryer J. R. (1986). Private Communication.

Gjonnes J. and Moodie A. F. (1965). Acta Cryst 19, 65.

Glaeser (1971) Jou Ultrastruct. Res. 36, 466 - 482.

Glaeser R. (1982) Methods Exp Physics 20, 391 - 444.

Glaser W. (1952) Grundlagen Der Elektronoptik (Springer Vienna).

Glaser W. (1956) In Handbuch Der Physik Vol XXX111, Springer Berlin 123 - 395.

Goodman J. W. (1968) 'Introduction to Fourier Optics'. McGraw-Hill New York.

Grainger and McConnell (1969) Acta Cryst B25, 1962.

Grainger and McConnell (1969) Acta Cryst B25, 1962.

Grano D. A. (1979) Ph.D. - Thesis. Lawrence Berkeley Laboratory. University of California.

Hanzen K. J. (1971) Adv. Opt Electron Micros. 4, 1.

Hanzen K. J. and Trepte L. (1971) Optik, 32, 519.

Harris R. K. Jonson P. and Packer K. J. (1984) Organic Mag. Res. 22-4, 269 - 271.

Hawkes P. W. (1972). In 'Electron Optics and Electron Microscopy,' Taylor and Francis, London.

Hawkes P. W. (1973) In 'Image Processing and Computer Aided Design in Electron Optics'. P.2. Academic Press, London, and New York.

Hawkes (1980). In 'Topics in Current Physics':- Computer Processing of E. M. Images. Springer - Verlag.

Henderson R., Baldwin J.M., Downing K.H., Lepault J. and Zemlin F. (1986). Ultramic., 19, 147 - 178.

Henry, N.E.M., Lipson H. and Wooster, W.A. (1951) The Interpretation of X-ray Diffraction Photographs. MacMillan, Oxford.

Hillier J. and Ramberg E. G. (1947). J. Applied Phys. 18, 48.

Hillier and Vance (1941) Proc Inst Radio Engrs 29, 167-176

Hirsch P. B., Howie A., Nicholson R. B., Pashley D. W. and Whelan M. J. (1965). 'Electron Microscopy of Thin Crystals' Butterworths, London.

Holland F., Fryer J. R. and Baird T. (1983) Inst. Phys. Conf. Ser. 68, 19-22.

Hopkins H. H. (1957) J. Opt. Soc. A. M. 47, 508.

Horne R. W. and R. Markham (1972) Applications of Optical Diffraction and Image Reconstruction techniques to Electron Micrographs Practical Methods in E. M. Vol. 1 Part 2. A. M. Glauert Ed. North Holland, Amsterdam. 327 - 434.

Int. Expm. Study Group (1986) Jou of Micros 141, 385-391.

Ito T. (1949) Nature 164, 755 - 756.

Kelemen J. (1981) Dyes and Pigments 2, 73 - 91.

Kelemen J., Moss S., Sauter H. and Winkler T. (1982a) Dyes and Pigments 3, 27.

Kelemen J., Kormany G. and Rihs G. (1982b) Dyes and Pigments 3, 249.

Kelemen J., Moss S. and Glitsch S. (1982c) Dyes and Pigments 5, 83 - 108.

Kinner J. F., Dow W., Scheidt W. R. (1976) Inorg. Chem 15, 1685 - 1690.

Knapek E. (1982) Ultramic 12, 71 - 86.

Knoll M. and Ruska E. (1932) Ann D. Physik 12, 607.

Kobelt, Paulus and Kunstmann (1972) Acta Cryst 28.

Kobelt. Paulus and Kunstman (1974) Z. Kristallogr. 139, 1315 - 1319.

Kobayashi T. and Reimer L. (1975) Bull Inst. Chem. Res. Kyoto University. 53, No.2.

Mason R., Williams G. A. and Fielding P. E. (1979) Jou Chem. Soc., Dalton Trans. (676 - 683).

Misell D. L. (1973) Advances Electron, Electron Phys 32, 63.

Misell D. L. (1978) Practical Methods in Electron Microscopy. Vol 7. Image Analysis, Enhancement and Interpretation.

Moser and Thomas (1983) The Phthalocyanines (Volumes 1&2) CRS Press.

Moss B. and Dorset D. L. (1982) Juo Polym. Sci. - Polym. Phys. Ed. 20, 1789.

Murata Y., Fryer J. R. and Baird T. (1976) Nature 263, No. 5576 401 - 402.

Murata Y., Fryer J. R., Baird T. and Murata H. (1977) (i) Acta Cryst A33 198 - 200.

Murata Y., Fryer J. R. and Baird T. (1977) (ii). Inst. Phys. Ser. Conf. No.36, 127 - 130.

Kobelt. Paulus and Kunstman (1974) Z. Kristallogr. 139, 1315 - 1319.

Kobayashi T. and Reimer L. (1975) Bull Inst. Chem. Res. Kyoto University. 53, No.2.

Mason R., Williams G. A. and Fielding P. E. (1979) Jou Chem. Soc., Dalton Trans. (676 - 683).

Misell D. L. (1973) Advances Electron, Electron Phys 32, 63.

Misell D. L. (1978) Practical Methods in Electron Microscopy. Vol 7. Image Analysis, Enhancement and Interpretation.

Moser and Thomas (1983) The Phthalocyanines (Volumes 1&2) CRS Press.

Moss B. and Dorset D. L. (1982) Juo Polym. Sci. - Polym. Phys. Ed. 20, 1789.

Murata Y., Fryer J. R. and Baird T. (1976) Nature 263, No. 5576 401 - 402.

Murata Y., Fryer J. R., Baird T. and Murata H. (1977) (i) Acta Cryst A33 198 - 200.

Murata Y., Fryer J. R. and Baird T. (1977) (ii). Inst. Phys. Ser. Conf. No.36, 127 - 130.

Nixon W. C., Ahmed H., Catto C. J. D. (1977)
Cleaver J. R. A., Smith K. C. A., Timbs A. E.
Turner P. W. and Ross. Inst. of Physics Conf. Ser. 13.

Reimer and Gilde (1973). In 'Image Processing and Computer - Aided Design in Electron Optics', ED. P. W. Hawkes P.138 Academic Press, London and New York.

Robertson J. M., (1935) J. Chem. Soc. 615.

Rosenfeld and Kak (1976) Digital Picture Processing. Academic Press.

Ruska (1934) Z Physik 87, 580 - 602.

Salih S. M. and Cosslet V. E. (1974) Phil Mag 30, 225.

Saxton W. O. (1978). In Computer Techniques for Image Processing in Electron Miscroscopy. Advances in Electronics and Electron Physics. Supplement Vol.10, Academic Press, New York, San Fransisco and London.

Saxton W. O., Horner M., Pitt T. (1979) Ultramic 4, 343

Scherzer O. (1949) Jou of Appl. Phys. 20, 20.

Schrodinger (1926). Ann. Physik. 81, 109 - 139.

Taylor K. A. and Glaeser R. M. (1976) Jou Ultrastr. Res. 55, 448 - 456.

Thomas L. E., Humphreys C. J., Duff W. R. and Grubb D. T. (1970) Radiation Effects, 3, 89 - 91.

Unwin, P. N. T. and Henderson R. (1975) J. Mol. Biol. 94, 425.

Uyeda N., Ishizuka K., Saito Y., Murata Y., Kobayashi K. and O'Hara M. (1974) 8th Int. Cong. on Electron Microscopy Canberra 1, 266 - 267.

Valentine R. C. (1966) Adv. Opt. Electron Micros 1, 180.

Whitaker A (1977) A. Kristallogr 145, 271.

Whitaker A (1977) Z. Kristallogr. 146, 173 - 184.

Whitaker A (1978)(A) Z. Kristallogr 147, 99 - 112.

Whitaker A (1978)(B) Jou. Syn. Dyers and Col. 94, 431-435

Whitaker A (1979) J. Appl. Cryst. 12, 626.

Whitaker A (1980) Z Kristallogr 152, 227.

Whitaker A (1982) J. S. D. C. 98, 436 - 439.

Williams R. C. and Fisher H. W. (1970) J. Mol. Biol. 52, 121 - 123.

Young T. I. (1971) Private Communication.

Zollinger H. (1961) In 'Azo and Diazo Chemistry; Aliphatic and Aromatic Compounds', Interscience.

Frank., J. (1980). In 'Topics in Current Physics:- Computer Processing of E. M. Images.', Springer - Verlag.

O' Keefe, M., Fryer J. and Smith D., (1983) Acta Cryst. A39 838.